Novel Mass Spectroscopy Techniques Implementing UV Action Spectroscopy for the Characterization of DNA Cation Radicals and Transition Metal Complexes

Andy Dang

A dissertation submitted in partial fulfillment of the requirements for the degree of:

Doctor of Philosophy

University of Washington

2019

Reading Committee:

František Tureček, Chair

Matthew Bush

Bo Zhang

Program Authorized to Offer Degree:

Department of Chemistry

University of Washington

Abstract

Novel Mass Spectrometry Techniques Implementing UV Action Spectroscopy for the Characterization of DNA Cation Radicals and Transition Metal Complexes

Andy Dang

Chair of the Supervisory Committee:
Professor František Tureček
Department of Chemistry

Mass spectrometry has become a powerful analytical tool for the detection and characterization of chemical compounds for biological and environmental studies. Advancements in mass spectrometry including new ionization sources, ion traps, and ion activation and separation methods have allowed for enhanced structure elucidation of gas-phase ions. With electrospray ionization, multiply-charged ions in solution can now be readily transferred into the gas phase. 3D quadrupole and linear ion traps can now facilitate multi-staged tandem (MS^n) mass spectrometry experiments. That is, ions (based on their mass-to-charge ratios) can be isolated and fragmented, desired fragment ions can be subsequently isolated and fragmented, and so on. Ion activation methods including collision-induced dissociation (CID), electron transfer dissociation (ETD), and UV-Vis photodissociation (UVPD) can now offer

different fragmentations of precursor ions and can be combined for more robust structural analyses. Here, novel tandem mass spectrometry techniques implementing UVPD action spectroscopy for the characterization of DNA cation radicals and transition metal complexes is presented.

To begin, the employment of new automated action spectroscopy methods on two different commercial mass spectrometers is discussed. UVPD action spectroscopy involves exposing isolated ions to high-energy photons and measuring the resulting photo-fragmentation as a function of photon wavelength (i.e. 200-700 nm). The generated action spectrum is representative of the gas-phase ion population's electronic excitations, and can be complemented with theoretical calculations to probe the predominant gas-phase structures. The modifications imposed on a 3D quadrupole and a linear ion trap mass spectrometer, including the optical setups needed to direct an external laser beam into the ion traps, are described in detail. Utilization of the instruments' auxiliary interface features, as well as the specific software (LabView) codes created to orchestrate automated MS^n-UVPD at specified photon wavelengths, is also reported. To compare the performance of the automated action spectroscopy methods between the two mass spectrometers, the experimental action spectrum of a well-studied compound was generated using both systems.

Next, the focus is shifted towards the characterization of DNA molecules using tandem mass spectrometry with UVPD action spectroscopy. Radiative damage of DNA can lead to the formation of nucleobase cation radicals along DNA chains, resulting in nucleobase loss and strand breaks. Here, DNA-based cation radicals of guanine, 9-methylguanine, and guanosine were generated in the gas phase, and their isolated structures and intrinsic properties were probed using UVPD action spectroscopy and excited state computations. The DNA cation radicals generated in the gas phase via MS^2-CID of their doubly-charged Cu(II)-complexes were isolated and subjected to MS^3-UVPD at incremental wavelengths from 210-700 nm. Experimental action spectra were acquired for the isolated cation radicals and were found to closely match the theoretical spectra generated by time-dependent density functional theory (TD-DFT) calculations, which considered various functionals and basis sets. The results also suggested that the guanine, 9-methylguanine, and guanosine canonical structures were the predominant cation radical conformations in the gas-phase, and were in agreement with past infrared multiphoton photodissociation (IRMPD) action spectroscopy studies.

The DNA nucleobase cation radical of thymine was also closely investigated using UVPD action spectroscopy in conjunction with other complementary methods. In this case, thymine cation radicals were generated via MS^2-CID of their doubly-charged Cu(II)-complexes and were characterized via UVPD action spectroscopy, hydrogen-deuterium exchange experiments, ion-molecule reactions, and theoretical calculations. The experimental results suggested a mixture consisting chiefly of non-canonical thymine cation radical tautomers (77%), with the canonical isomer as a minor component (23%). Theoretical calculations predicting the low-energy isomers also supported the experimental results.

Lastly, the peculiar discovery of gas-phase water splitting involving simple transition metal complexes is addressed. For decades, immense efforts have been directed at achieving catalytic water splitting using sophisticated water oxidation complexes and sunlight to generate carbon-neutral fuels. Here, a novel method utilizing transition metal complexes and near-UV light to split water into hydroxyl radical is explained. (2,2'-bipyridine)Metal-O^+ ions (Metal = Cu, Ni, Co) were first produced by near-UV photodissociation of $[(2,2'\text{-bipyridine})\text{Metal}^{II}NO_3]^+$ ions in the gas phase. Upon storage in an ion trap, the (2,2'-bipyridine)Metal-O^+ ions

spontaneously added water, and the newly-formed [(2,2’-bipyridine)Metal-O + H_2O]$^+$ complexes eliminated OH after subsequent near-UVPD (i.e. 260-340 nm) to achieve stoichiometric homolytic cleavage of gaseous water. Ion-molecule reactions, isotope-labeling experiments, and DFT calculations were further conducted to better characterize the reactions.

Table of Contents

Chapter 1: Introduction…...………………………………………………………..............1

1.1 Mass Spectrometry……………………………………………………………………1
1.2 Ionization Sources…………………………………………………………………….3
1.3 Mass Analyzers and Ion Traps...……………………………….……………………...6
1.4 Ion Activation………………………………………………………………………..11
1.5 UV Action Spectroscopy……………………………………………………………15
1.6 Detection Methods…………………………………………………………………...18
1.7 References……………………………………………………………………………20

Chapter 2: UV-Vis Photodissociation Action Spectroscopy on Thermo LTQ-XL ETD and Bruker amaZon Ion Trap Mass Spectrometers……………………….……………........……..24

2.1 Introduction………………………….……………………………………………...24
2.2 Design……………………………………………………….………………………25
2.3 Experimental Results and Discussion…………………..……………………………32
2.4 Conclusions…………………………………………………………………………36
2.5 Acknowledgments……………..……………………………………………………..36
2.6 References……………………………………………………………………………36

Chapter 3: UV-Vis Action Spectroscopy of Guanine, 9-Methylguanine, and Guanosine Cation Radicals in the Gas Phase……………....……………………………………………..41

3.1 Introduction…………………………………………………………………………..42
3.2 Experimental Section……...…………………………………………………………44
3.3 Results and Discussion………………………………………………………………46
3.4 Conclusions…………………………………………………………………………..70
3.5 Acknowledgments……………………………………………………………………71
3.6 References……………………………………………………………………………71

Chapter 4: Experimental Evidence for Non-canonical Thymine Cation Radicals in the Gas Phase……………….........................…………………………………………………...81

4.1 Introduction……………………………………………………………………..82

4.2 Experimental Section……………………………………………………………...84

4.3 Results and Discussion…………………………………………………………88

4.4 Conclusions……………………………………………………………………109

4.5 Acknowledgments……………………………………………………………..109

4.6 References……………………………………………………………………..110

Chapter 5: Near-UV Water Splitting by Cu, Ni, and Co Complexes in the Gas Phase…..121

5.1 Introduction……………………………………………………………………121

5.2 Experimental Section………………………………………………………….123

5.3 Results and Discussion……………………………………………………..126

5.4 Conclusions……………………………………………………………………148

5.5 Acknowledgements……………………………………………………………149

5.6 References……………………………………………………………………..149

Acknowledgments

I would like to start by thanking Professor Karen Singmaster. You converted me to chemistry back when I was an undergraduate at San Jose State University. Thank you for your support throughout the years, and for inspiring me to pursue a Ph.D.

I would like to thank Professor Joseph Pesek and Dr. Maria Matyska, my undergraduate research advisors from SJSU. You two have been amazing mentors since the beginning of my journey as a scientist. Thank you for all of your advice and support.

I would like to thank my fellow colleagues from the University of Washington. Chris, thank you for being the best post-doc, and for showing me the ropes. Rob, thank you for being a great friend and scientist to bounce ideas and questions off of. Ivy, thank you for the laughs and distractions. Jarred, thanks for the much-needed excursions after work. Yang, thank you for all of the out-of-office breaks, and for being a great friend. Emilie, thanks for being the best conference buddy and for all of the great and random moments. I truly enjoyed getting to know all of you.

I would like to thank my committee members for their time and support, as well as the National Science Foundation for funding the various research projects I’ve been involved in. I would also like to thank the Department of Chemistry at the University of Washington, Seattle for making my Ph.D. experience so memorable.

Finally, I would like to thank Professor František Tureček. Thank you for being an outstanding research advisor and role model. Thank you for taking a chance on me, and for giving me the opportunity to get involved in awesome new research projects in your lab. I’ve learned so much from you and am so grateful to have met you. Thank you.

Dedication

I would like to dedicate this dissertation to my family. Mom, thank you for everything you’ve done for Jason, Eric, and me. You’ve sacrificed so much for us and I hope I make you proud. Jason and Eric, thank you for always having my back, even when we’re miles apart. To my grandparents, aunts, and uncles, thank you for your consistent love and support throughout the years. I would also like to dedicate this dissertation to my partner-in-crime. Trang, thank you for always believing in me. I am so lucky to have you in my life. Sincerely, from the bottom of my heart, thank you all so much.

Chapter 1: Introduction

1.1 Mass Spectrometry

What is mass spectrometry, and why is it considered a powerful analytical tool? For starters, mass spectrometry (MS) is a chemical detection method that involves the generation of gas-phase ions, separation of ions based on their mass-to-charge ratio (*m/z*), and detection of ions for the identification and analysis of chemical compounds. As such, mass spectrometers are instruments that typically consist of an ionization source, a mass analyzer, and a detection system. They produce output plots called mass spectra which depict the relative abundance of ions measured (with respect to their *m/z*), and they can be used to analyze compounds ranging from diatomic molecules to DNA complexes. Throughout the last century, significant technological advancements have greatly enhanced the effectiveness and versatility of mass spectrometry as an analytical tool for the characterization of gas-phase ions and have resulted in numerous exciting scientific discoveries. In other words, if asked, "Can you tell me what is in this unknown sample?" mass spectrometry would reply, "Of course. Let's kick some mass."

Before diving into the new capabilities of today's instruments, let's briefly recall the fascinating history of mass spectrometry, which goes back to the late 1890s. At the University of Cambridge, a physicist by the name of J.J. Thomson was using cathode ray tubes to study how electricity traveled through gas-phase mediums. With the help of his laboratory assistant, E. Everett, Thomson developed an apparatus capable of indirectly measuring the mass of the electron (from its charge-to-mass ratio, *e/m*, and charge, *e*), which led to Thomson being awarded the Nobel Prize in Physics in 1906 for "discovering" the electron. Not long after, Thomson and his apprentice Francis Aston constructed a “parabola spectrograph” (now referred to as the first mass spectrometer!) and were able to measure the atomic weight of elements. Their parabola spectrograph (**Fig. 1.**) generated gas-phase ions via electrical discharge of gas molecules between a cathode and anode, implemented electromagnetic fields to alter the trajectories of the ions and to separate them according to their *m/z*, and used a photographic plate to detect the resolved ions. That is, their parabola spectrograph was composed of an ionization source, a mass analyzer, and a detector, and laid the groundwork for future designs and applications of mass spectrometers over the next century.

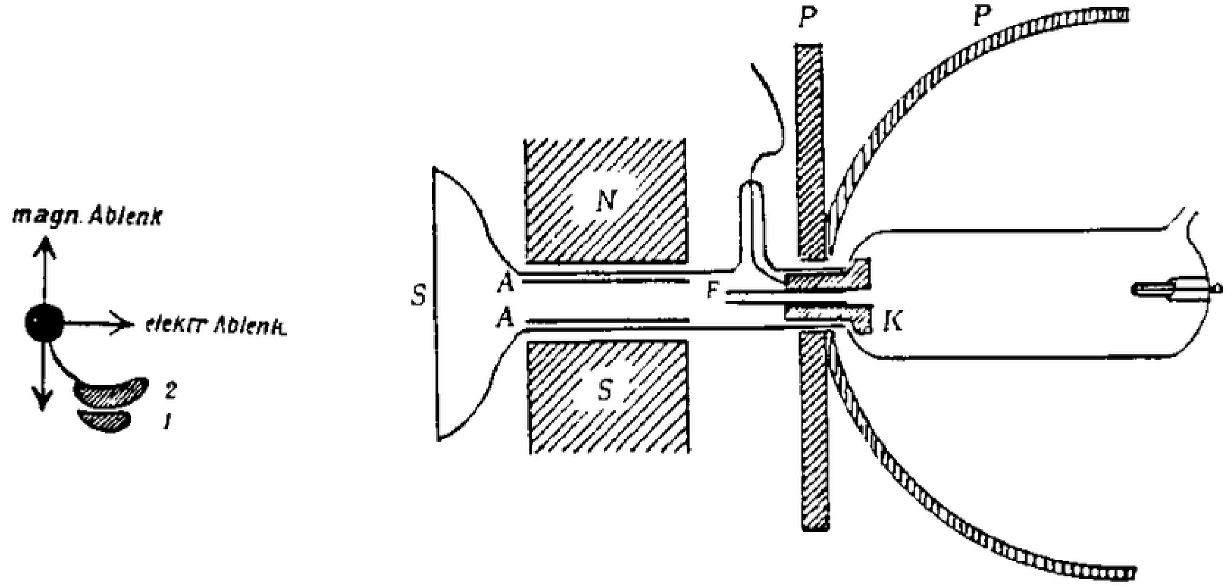

Figure 1. Schematic of Thomson and Aston’s parabola spectrograph. (K) cathode, (F) capillary between ionization source and mass analyzer, (N, S) magnetic poles, (A, A) electrically-charged parallel plates, (S) photographic plate. Image from: https://www.researchgate.net/figure/Sketch-of-a-parabola-image-spectrograph-constructed-by-Thomson-for-canal-rays-in-1897-K_fig7_26365910.

Mass spectrometry has since been involved in a plethora of noteworthy scientific contributions and continues to adapt with the demands of science and technology. Namely, soon after Thomson’s work in the early 1900s, mass spectrometers with improved resolving power were utilized to obtain experimental evidence for the existence of elemental isotopes, and to separate uranium ($^{235}U/^{238}U$) isotopes for the development of the first nuclear bomb. Over the last few decades, new mass spectrometer designs implementing new ionization sources, mass analyzers, and detection methods further pushed the method’s quantitative and qualitative capabilities, enabling the characterization of larger macromolecules like metabolites and proteins. This analytical technique is now routinely implemented in clinical, academic, and industrial laboratories for an impressive range of biological and environmental studies.[1,2] Before exploring the latest applications of novel mass spectrometry methods in detail, there are a few fundamental processes and concepts that must first be reviewed.

1.2 Ionization Sources

How can gas-phase ions be formed from different samples? Mass spectrometry often begins with the generation of gas-phase ions from some sample background with the use of an ionization source. Remarkably, today’s mass spectrometers can now employ various ionization sources to produce gas-phase ions from gas-, liquid-, and solid-phase matrices (depending on the compound of interest), and hence are notably robust and applicable for a range of chemical analyses. Common forms of positively- and negatively-charged ions generated and analyzed by mass spectrometry include protonated/deprotonated, ion-adducted, and cation-/anion-radical species (e.g. $[M + H]^+$, $[M + Na]^+$, and $[M]^{+\cdot}$, respectively, along with their negatively-charged analogues). Of the many newly engineered ionization sources developed over the last century, electron impact (EI), matrix assisted laser desorption ionization (MALDI), and electrospray ionization (ESI) have been widely utilized and will be discussed in this text.

For decades, electron impact (EI) ionization was the most popular ionization source for mass spectrometry due to its ability to generate gas-phase ions from neutral gas-phase molecules. As the name suggests, EI involves accelerating a stream of electrons at sample gases to produce charged analytes (**Fig. 2.**). That is, electrons are created by a heated filament and are accelerated toward a gaseous sample contained in an ionization chamber at reduced pressure (~10^{-5} Torr). The high-energy electrons collide with the neutral analyte molecules, causing electrons to be ejected and ions to be formed. The analyte ions can then be passed through a mass analyzer and detection system to be characterized via mass spectrometry. EI is described as a "hard" ionization method since the analytes often undergo fragmentation during the ionization process (i.e. the energy transferred from the electron impact is enough to cause dissociation of the analyte, which can leave only fragment ions of the molecular species to be detected). This could

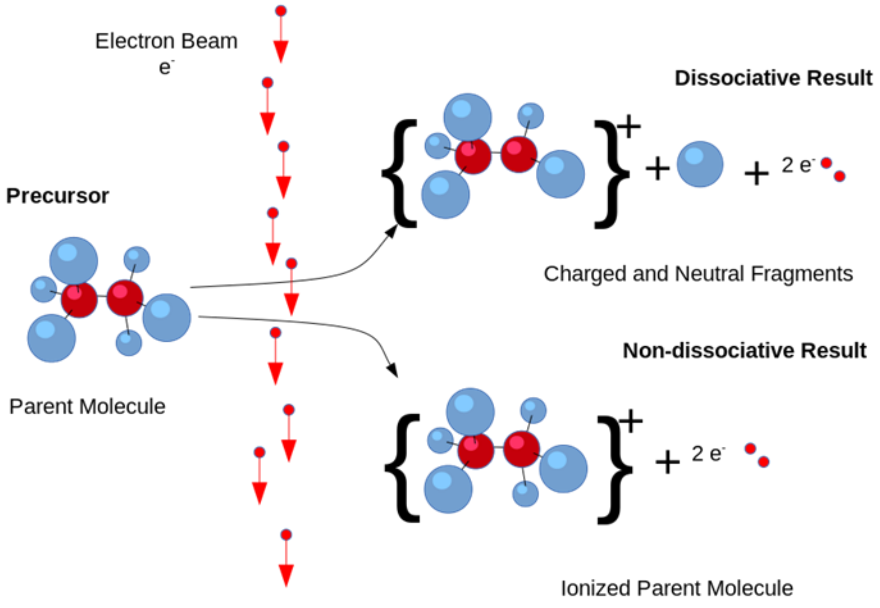

Figure 2. Schematic of electron impact ionization of a neutral molecule. Image from: https://en.wikipedia.org/wiki/Electron_ionization#/media/File:Electron_Ionization.svg.

dampen mass spectral analysis and is not desirable when it comes to the characterization of unknown compounds based on their molecular structure.[3] Although EI has demonstrated its value as an ionization source for gaseous samples, not all analytes have the volatility and gas-phase stability to undergo EI and thus different ionization methods for liquid and solid phases are needed for mass spectrometry.

A clever ionization method called matrix assisted laser desorption ionization (MALDI) now enables the formation of ions from solid matrices. MALDI involves mixing the analyte in a UV- or IR-absorbing matrix material and allowing it to dry on a sample plate. Laser pulses are directed at the solidified sample/matrix spot and are absorbed by the matrix material, which leads to ablation, desorption, and eventual ionization of the sample. The analyte ions are accelerated toward the mass analyzer and detector for mass spectrometric analysis. Opposed to EI, MALDI is considered a “soft” ionization method that can generate molecular ions without significant fragmentation. For this reason, MALDI has been shown to be valuable for the characterization of macromolecular species such as oligonucleotides and peptides, further extending the bioanalytical reach of mass spectrometers.[4]

Electrospray ionization (ESI), another soft ionization method, can facilitate the production of gas-phase ions from liquid-phase samples. For ESI, a sample solution is passed through a capillary held at a high potential (~2-3 kV) and exits the capillary tip as a fine spray of electrostatically charged droplets (**Fig. 3.**) at atmospheric pressure. As the charged droplets travel toward the mass spectrometer inlet, rapid solvent evaporation and electrostatic repulsion occur which result in charged gas-phase analyte ions being released from the electrospray. The analyte ions then enter the mass spectrometer for analysis. Compared to MALDI, ESI has the advantage of being able to readily produce large gas-phase macromolecules with relatively higher charge states, which can significantly reduce the upper limit for *m/z* detection. That is, 200 kDa proteins multiply-charged with protons can be analyzed at *m/z* 600-2000, as a higher charge *z* gives a lower *m/z*. Additionally, ESI can operate under continuous sample-injection flow conditions, making it a popular complementary component following HPLC liquid separation systems.[3] Hence, it is not surprising that ESI is now one of the most commonly used ionization sources for mass spectrometry. Other ionization methods such as chemical ionization (CI) and fast atom bombardment (FAB) have also demonstrated notable utility in mass spectrometric analyses but will not be further discussed in this text.

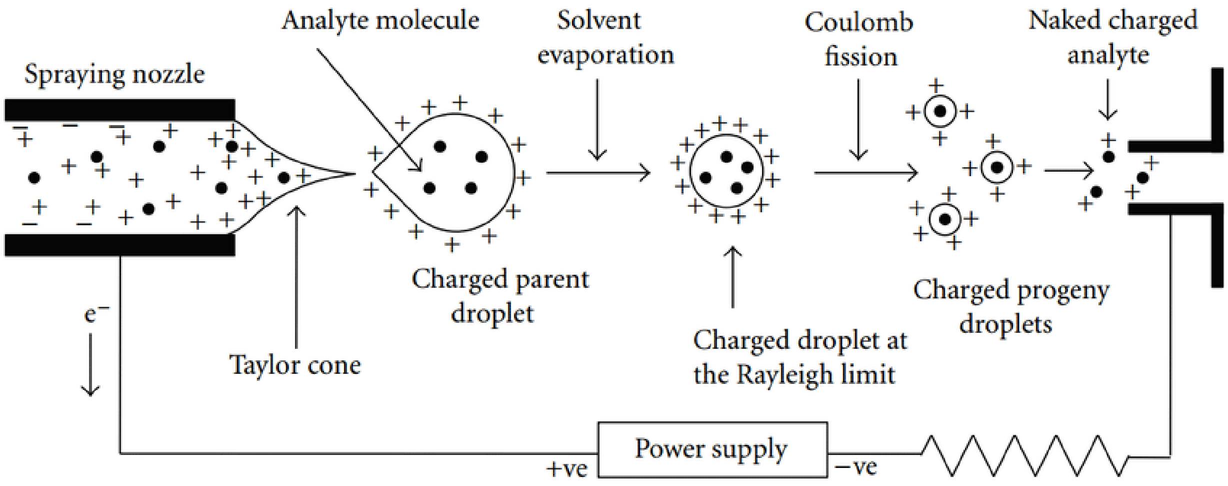

Figure 3. Schematic of gas-phase ion generation from electrospray ionization. Image from: https://www.researchgate.net/figure/Schematic-representation-of-the-electrospray-ionization-process-Adopted-from-33_fig5_307606559.

1.3 Mass Analyzers and Ion Traps

Gas-phase ions can be generated from ionization sources, but how can they be separated and isolated from one another before detection? After exiting the ionization source, gas-phase ions are typically accelerated with ion-optic systems toward a mass analyzer. A variety of mass analyzers have been developed to selectively filter charged molecules according to their *m/z* often with the use of magnetic and/or electric fields under considerably low-pressure conditions. Certain mass analyzers called ion traps also have the power to isolate (i.e. “trap”) and if desired, fragment chosen ions for better analyte characterization via tandem mass spectrometry (MS/MS or MS^n). Relatively low-pressure conditions are maintained inside mass analyzers to minimize background-gas collisions as the ions travel to the detector, as less perturbed ion trajectories can result in better mass assignment upon detection. There have been many unique mass analyzers implemented over the last century, of which magnetic sectors, quadrupole mass filters, and ion traps will be presented here.

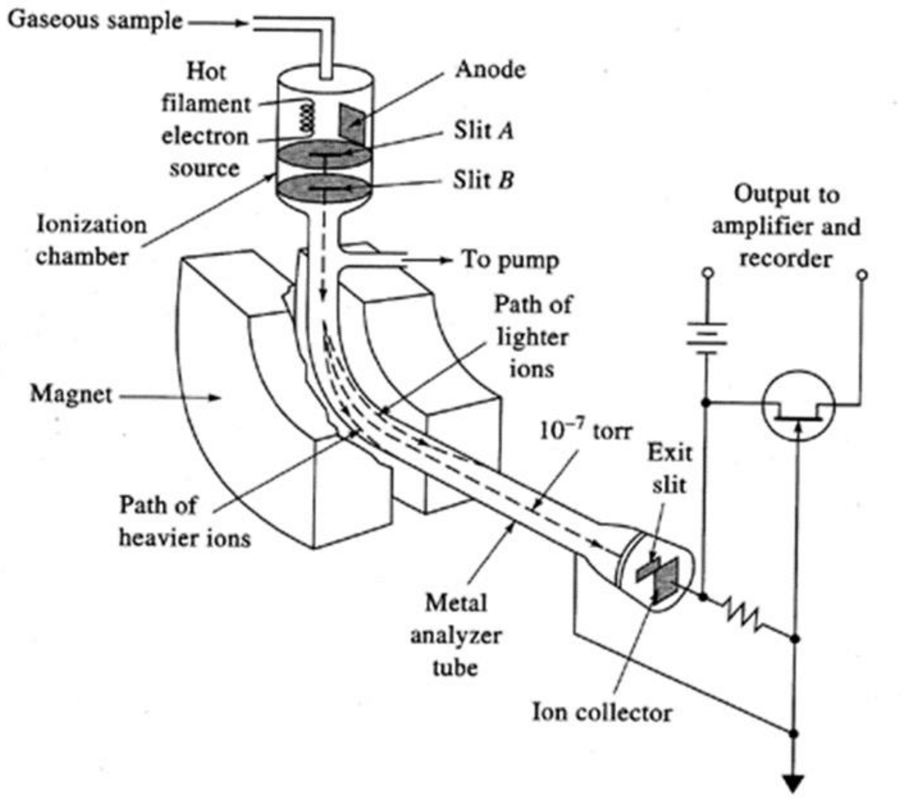

Figure 4. Schematic of magnetic sector mass analyzer with EI source. Image from: https://clu-in.org/characterization/technologies/windows/msector.htm.

Magnetic sectors employ a relatively simple design to distinguish gas-phase ions of varying *m/z* after they are formed from an ionization source. As shown in (**Fig. 4.**), sample ions released from an EI source can be propelled through a magnetic field, which alters their trajectories in space and allows for only a select group of ions to successfully pass through the exit slit and be detected. That is, ions with constant kinetic energy but different masses can be differentiated by their trajectories through a magnetic field. Therefore, by knowing the potential applied on the ions, the strength of the magnetic field, and the radius of the ion trajectory through the field, one can determine the *m/z* and identity of ions reaching the detector. Other sector-type mass analyzers (e.g. double-focusing mass spectrometers) have been developed which also implement electrostatic fields to achieve higher resolving power.[3,5]

Quadrupole mass filters and ion traps are among the most widely used mass analyzers today. In fact, Wolfgang Paul's contributions to the development of quadrupole mass analyzers earned him the Nobel Prize in Physics in 1989 (along with Norman Ramsey and UW Physics Professor Hans Dehmelt).[2] Quadrupole mass filters are composed of two oppositely-placed pairs of metal rods arranged in parallel configuration, of which a combination of direct-current (DC) and oscillating radio-frequency (RF) electrical fields are applied. As illustrated in (**Fig. 5.**), gas-phase ions exiting the ionization source enter the quadrupole mass filter axially between the four rods and their trajectories are immediately altered by the applied voltages. By adjusting the DC and RF voltages, ions of desired *m/z* can be allowed to pass entirely through the quadrupole mass filter and to the detector. Ions outside of the desired *m/z* specifications will contrastingly undergo unstable trajectories and not be detected.[3]

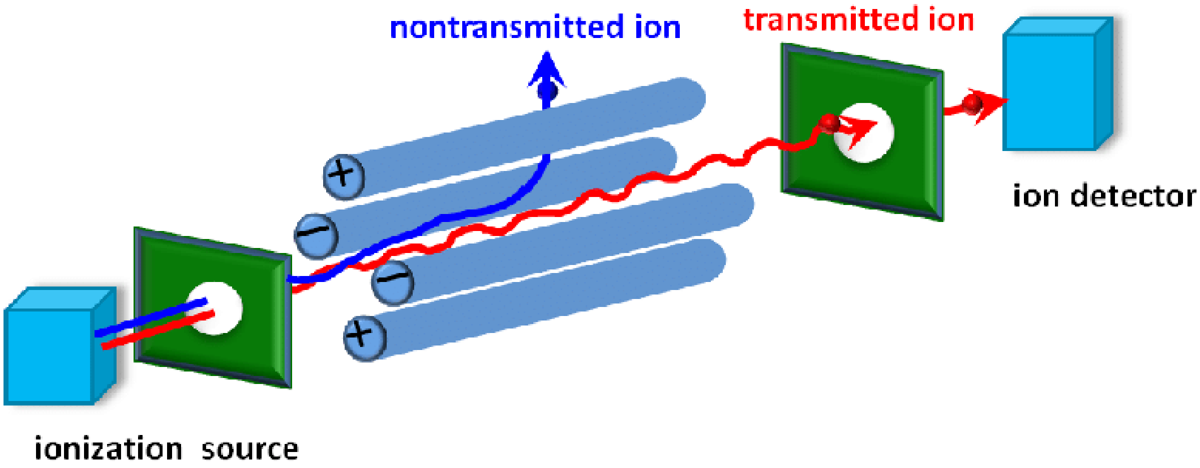

Figure 5. Schematic of quadrupole mass filter. Image from: https://www.researchgate.net/figure/Scheme-of-quadrupole-mass-analyzer-Q_fig4_329040300.

Building upon the quadrupole mass filter design, linear ion traps have been engineered to facilitate the subsequent isolation, fragmentation, and ejection of desired ions with respect to their *m/z*. Linear ion traps, also known as 2D traps, are composed of three consecutive sets of quadrupole rods (QQQ) which primarily implement RF voltages for ion trapping (**Fig. 6.**). The shorter first and third set of quadrupoles (Q1 and Q3) can act as ion gates, allowing only ions of certain *m/z* to pass into or out of the middle set (Q2), which can operate as a collision cell to facilitate ion isolation and dissociation.[3] Depending on the chemical analysis, molecular ions and/or MS^n fragment ions can be selectively sent out of the exit slot of Q2 for detection. In cases when ion-ion reactions (e.g. electron transfer dissociation) are desired, positively- or negatively-charged reagent compounds can be mass filtered from Q3 into Q2 to interact with trapped analyte ions that were sent into Q2 from Q1.[6] The ability of linear ion traps to conduct tandem MS^n experiments has enabled better qualitative characterization of mixtures and discrimination of isomeric compounds, as ions of specific *m/z* can be selectively dissociated to produce fragment ions more indicative of certain molecular structures over others.[7,8]

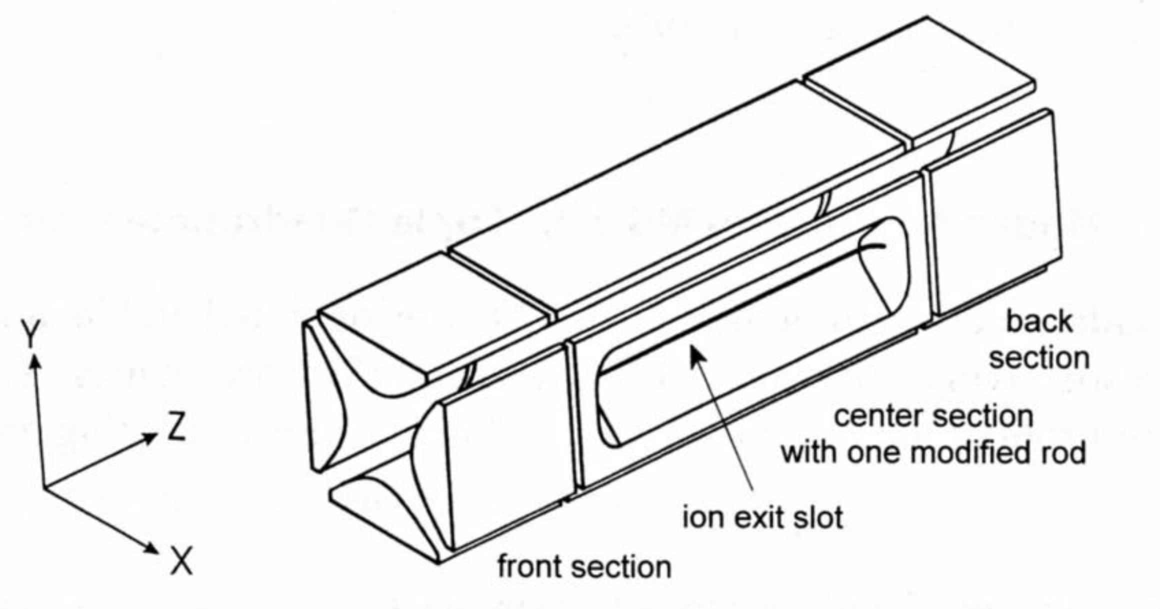

Figure 6. Schematic of linear ion trap. Image from: https://www.researchgate.net/figure/Linear-ion-trap_fig15_281755688.

Another popular ion trap mass analyzer, called the three-dimensional (3D) quadrupole ion trap, has also established itself as an effective tool for ion trapping and dissociation over the years. Similar to 2D linear ion traps, 3D ion traps utilize mostly RF voltages to conduct MS^n analyses, but with a distinct physical design. 3D ion traps are made of a ring electrode sandwiched between two hyperbolically shaped electrodes, sometimes referred to as end caps (**Fig. 7.**). By adjusting the applied DC and RF voltages, ions of desired *m/z* can be sent into the 3D ion trap through the first end cap, isolated and/or dissociated in the cavity between the electrodes, then ejected through the second end cap to be detected. Although the physical design of 2D linear ion traps generally allow for greater ion capacity and thus better sensitivity, 3D ion traps are more compact, relatively cheap, and also capable of sophisticated MS^n analyses.[3,9]

Other effective mass analyzers worth acknowledging include time-of-flight (TOF) and Orbitrap high-resolution mass spectrometers.

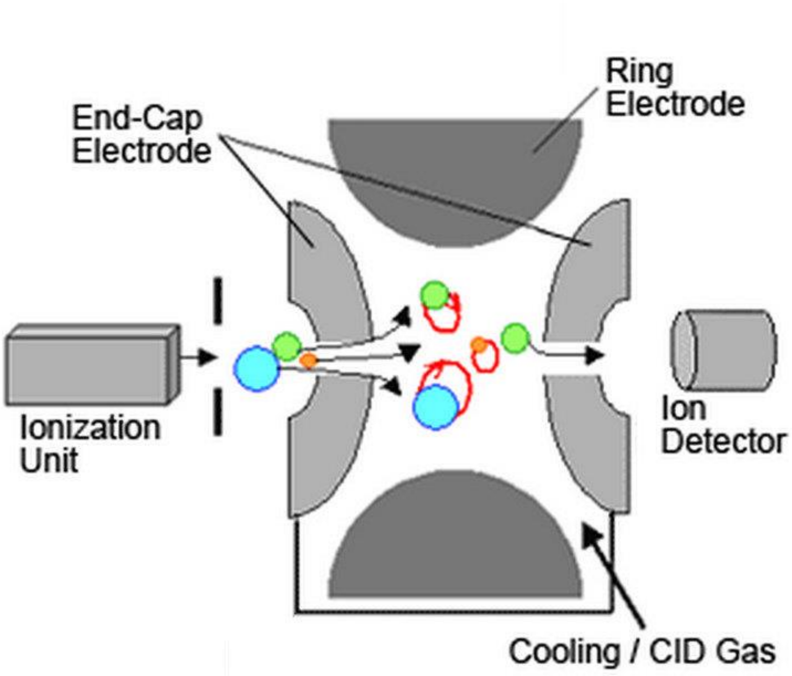

Figure 7. Schematic of 3D quadrupole ion trap. Image from: https://www.researchgate.net/figure/Schematic-arrangement-of-the-lenses-of-a-quadrupole-3D-ion-trap-OHair-2006_fig5_273134301.

1.4 Ion Activation

How can ions be selectively activated and fragmented, and why is this desired? There are a number of cases where the (MS^1) mass spectrum of the injected sample does not provide enough information for analyte characterization, especially when samples contain a mixture of isomeric species. Hence, the ability to generate various fragment ions in different ways can greatly enhance the elucidation of ion structures in the gas phase. The three ion activation methods that will be described here are collision induced dissociation (CID), electron transfer dissociation (ETD), and UV-Visible photodissociation (UVPD).

Collision induced dissociation (CID) is now the most common method to promote fragmentation of isolated ions, particularly among 2D and 3D quadrupole ion traps. As the name suggests, CID involves forcing analyte ions to collide with buffer gas molecules to induce fragmentation. This is accomplished by applying a voltage waveform to isolate only ions of desired *m/z* in the ion trap, which typically already contains inert buffer gas such as helium. An oscillating potential (i.e. resonant excitation waveform) is then used to resonantly excite the trapped ions which can increase their kinetic energies and induce more energetic collisions with the background helium atoms. These collisions can gradually raise an ion's internal energy, which is redistributed throughout the ion's vibrational modes and can lead to dissociation if the bond dissociation energy is exceeded. The extent of dissociation can be adjusted by changing the time duration and amplitude of the resonant excitation waveform for CID.[10] This ion fragmentation technique can now be achieved with most commercial ion trap mass spectrometers and can be combined with other MS^n methods like ETD and UVPD for more comprehensive ion identification.[11,12]

Electron transfer dissociation (ETD) is another ion activation method employed for MS^n structure elucidation and involves the transfer of electrons to multiply-charged cations for fragmentation. To perform ETD, multiply-charged cations of chosen *m/z* are first isolated in an ion trap. Electron donors, typically anion radicals like fluoranthene, are then directed into the ion trap to react with the trapped analyte cations (**Fig. 8.**). The electron transfer reactions can lead to the formation of neutralized electron donor molecules along with analyte cation radicals which often undergo rapid radical-driven fragmentations that cannot be attained via CID. Particularly

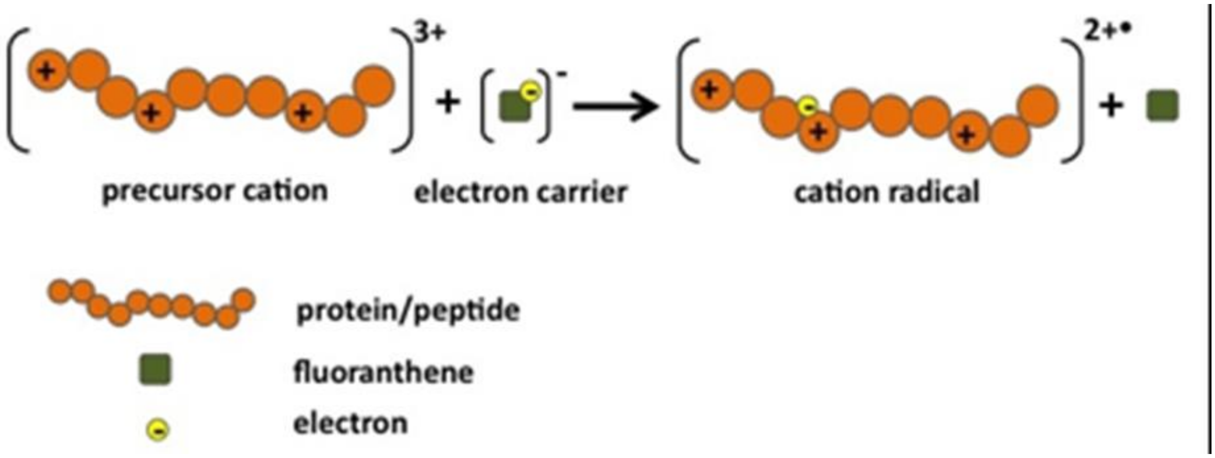

Figure 8. Schematic of charge-reduced cation radical formation via ETD. Image from: https://nationalmaglab.org/user-facilities/icr/techniques/electron-transfer-dissociation.

when it comes to peptide sequencing and characterization of post translational modifications (PTMs), ETD has been shown to induce useful *c*-/*z*-type backbone fragmentations while conserving PTMs in cases where CID produced *b*-/*y*-type dissociations with loss of PTMs.[13] Interestingly, there are also instances where dissociation after electron transfer is undesired (i.e. ET-no-D), as was the case when ET-no-D was recently used to generate and characterize hydrogen-rich DNA cation radical complexes related to DNA damage.[14] To be analyzed via ETD, analyte cations must be at least doubly-charged since the electron transfer reaction results in charge-reduced ions (i.e. a singly-charged cation would no longer have a charge after ETD and thus be not measured by the ion detector). ETD also requires a separate chemical ionization source to generate the anion radical electron donors needed for the electron transfer reaction.

A third ion activation method called UV-Vis photodissociation (UVPD) uses high energy photons to excite ions for both structure elucidation and reaction triggering. Pulses of photons in the UV-visible region (i.e. 200-700 nm) can be sent into an ion trap to be absorbed by select ions isolated according to their *m/z*. Depending on the analyte ions, absorption of photons from this wavelength region can cause rapid electronic excitations resulting in photofragmentation and in some cases, new bond formation. There are three main routes of dissociation that can result from UV-Vis photon absorption (**Fig. 9.**). The first involves a transition from the electronic ground state to an excited vibrational level in the electronic excited state that lies above the dissociation threshold, leading to fragmentation from the electronic excited state (**Fig. 9.**, left). In the second scenario, the electronic energy from the photon absorption is converted to vibrational energy via internal conversion, leading to dissociation from the electronic ground state (**Fig. 9.**, center). The third scheme includes fragmentation after excitation and curve crossing to a dissociative state (**Fig. 9.**, right).[15] Recently, an innovative application of UVPD was reported which involved peptide dimer complexes photo-tagged with diazirine chromophores. Upon photo-activation with 355 nm laser pulses, new covalent bonds can be generated intermolecularly from the diazirine tags and further probed via MS^n-CID to characterize non-covalent interactions between different

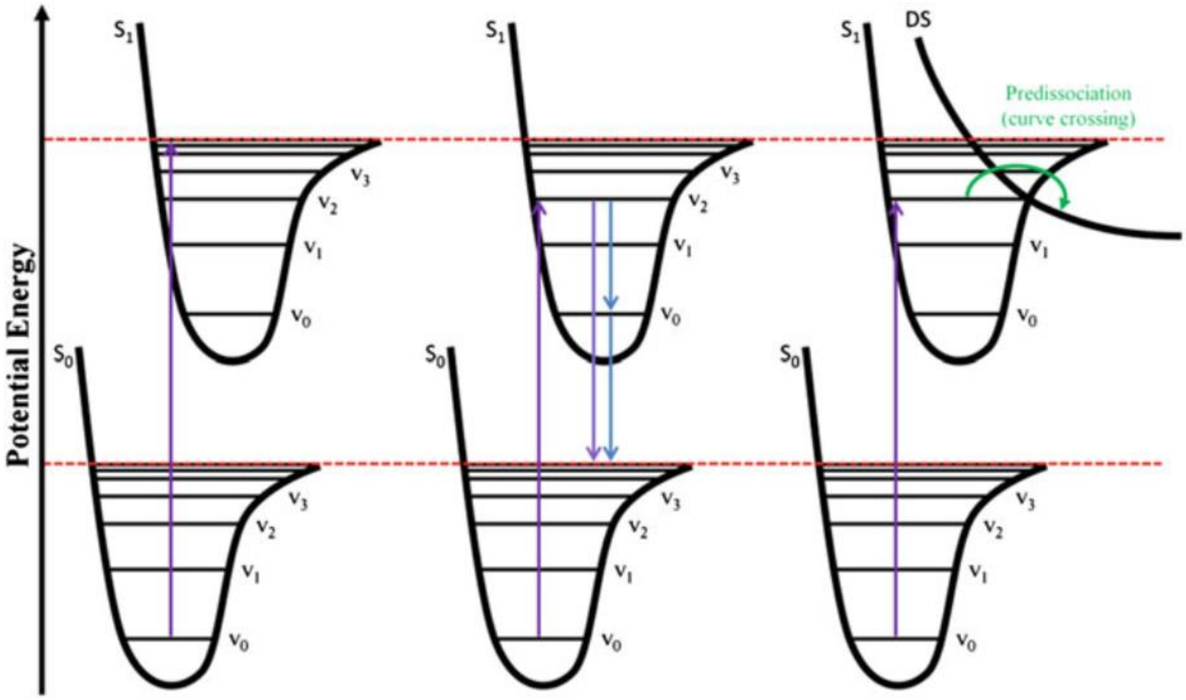

Figure 9. Schematic of photodissociation pathways after UV-visible photon absorption. Image from: N. Polfer, P. Dugourd. Laser Photodissociation and Spectroscopy of Mass-separated Bimolecular Ions: Lecture Notes in Chemistry 83. *Springer*, 2013.

peptide molecules.[16,17] Other interesting single-wavelength UVPD analyses[18] utilizing 157, 193, and 266 nm photons have also been reported, and a valuable tunable-wavelength UVPD technique called UV action spectroscopy will be presented in the next sub-chapter. Ions of interest must either contain a chromophore or functional group that absorbs light within the UV-visible wavelength region in order for these methods to be effective. UVPD also often requires instrumentation modification to allow optical access for laser pulses to enter the mass spectrometer and to reach the analyte ions, as well as synchronization of a tunable laser system, both of which will be elaborated upon in **Chapter 2**.

1.5 UV Action Spectroscopy

What is action spectroscopy and why is it used to study gas-phase ions? Action spectroscopy, sometimes referred to as consequence spectroscopy, is an MS^n technique for ion characterization that involves measuring the fragmentation that results from photon absorption.

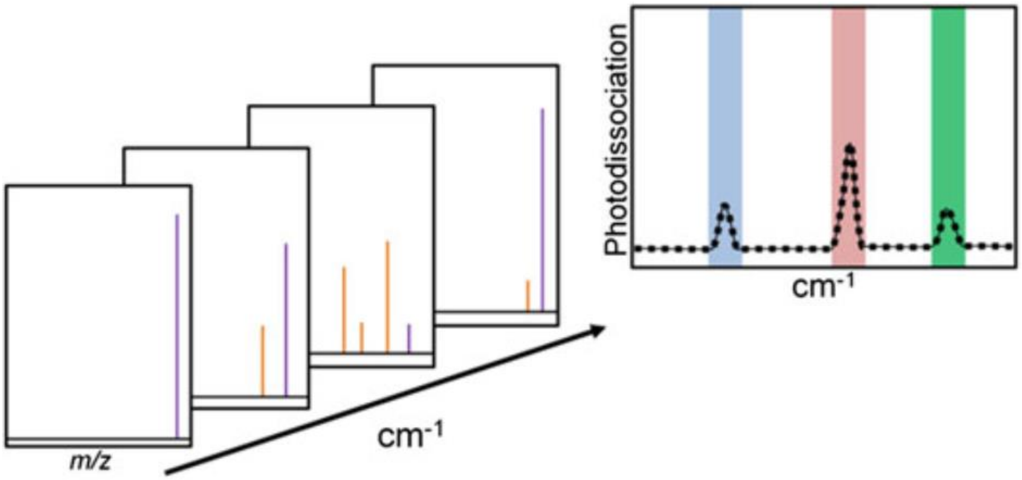

Figure 10. Schematic illustrating photodissociation mass spectra collected at different frequencies to generate an experimental action spectrum. Image from: N. Polfer, P. Dugourd. Laser Photodissociation and Spectroscopy of Mass-separated Bimolecular Ions: Lecture Notes in Chemistry 83. *Springer*, 2013.

More specifically, ions of interest can be isolated in an ion trap and subjected to photodissociation at incremental wavelengths, and the relative abundance of the photofragments can be monitored and plotted as a function of photon wavelength to generate an action spectrum (**Fig. 10.**). Depending on the range of photon energies implemented (**Fig. 11.**), the action spectrum can be representative of the isolated ion population’s different transitions (i.e. electronic, vibrational) and can be complemented with computational modeling for gas-phase structure elucidation.

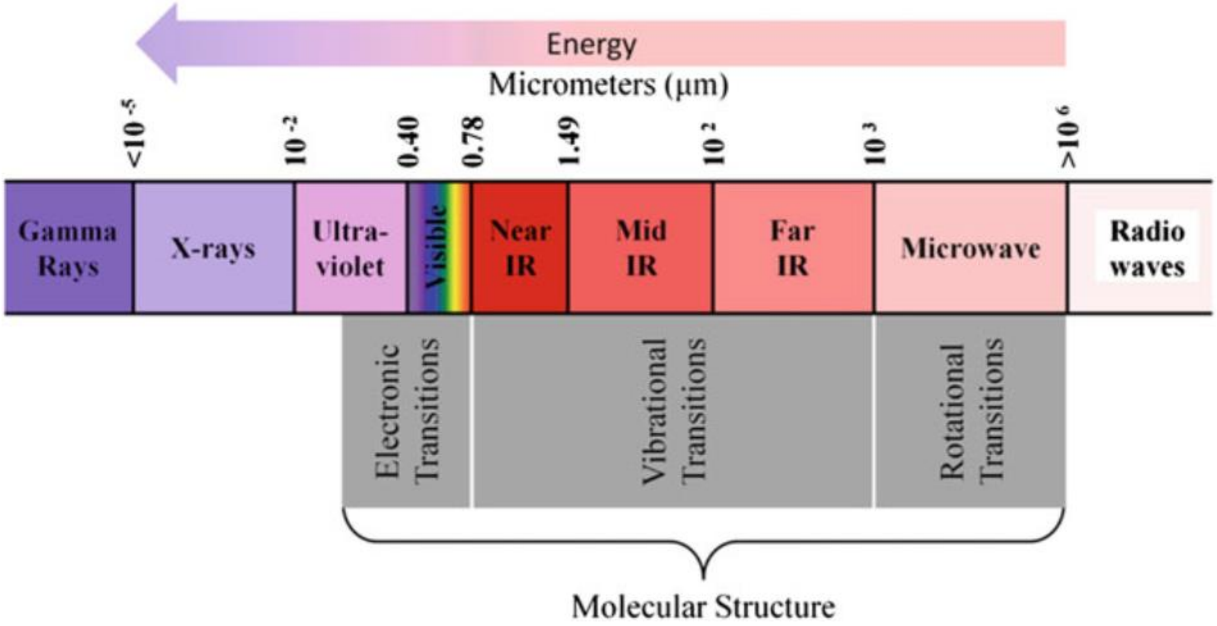

Figure 11. Schematic of electromagnetic spectrum and corresponding transitions from photon absorption. Image from: N. Polfer, P. Dugourd. Laser Photodissociation and Spectroscopy of Mass-separated Bimolecular Ions: Lecture Notes in Chemistry 83. *Springer*, 2013.

Why is action spectroscopy – and not absorption spectroscopy – used to study gas-phase analytes? For condensed-phase samples, an analyte's absorption spectrum can be obtained by shining light though a cuvette containing an optically thick sample solution and measuring the amount of light that passes through the solution (i.e. transmittance) to the detector. This direct absorption measurement method can be extremely challenging with gas-phase ions in a mass spectrometer, as the number density of gas-phase ions in an ion trap is significantly lower than the concentration of ions in a sample solution/cuvette. For this reason, mass spectrometry relies on the result, or consequence, of the photon absorption in the form of photofragmentation to study a gas-phase compound's electronic/vibrational transitions (i.e. the amount of photodissociation is related to the absorption cross section at that wavelength). By measuring the relative abundance of photofragmentation versus photon wavelength – not the absolute amount of photodissociation – MS^n action spectroscopy can attain experimental action spectra with just a few hundred gas-phase ions in an ion trap, and even with very low fragmentation yields.[15]

UVPD action spectroscopy uses higher-energy photons from the UV-visible wavelength region that can induce electronic transitions and single-photon dissociations, while infrared multiphoton dissociation (IRMPD) action spectroscopy involves lower-energy photons that can cause vibrational transitions and typically require multiple photon pulses for ion fragmentation. Both methods are implemented to produce experimental action spectra indicative of the molecular structure and are often paired with theoretical calculations to characterize ion populations. The use of UV vs. IR action spectroscopy is often dictated by the compound of interest. For example, if an ion does not absorb light in the accessible wavelength region, there will simply be no photofragmentation and thus no action spectrum to be measured. In other cases, some compounds may have higher dissociation thresholds, wherein the higher-energy photons from UV action spectroscopy could be advantageous over those from IR action spectroscopy. Additionally, if an ion can easily isomerize via pathways of low activation energy, the “slow heating” activation of IRMPD could potentially profile isomers of the original ion structure, while the more rapid electronic excitations from UVPD may better capture the ion conformation without low-energy isomerization.[15,18]

To interpret the experimental action spectra, high-level calculations are often implemented to simulate the vibrational and electronic excitations.[19,20] The computational workflow commonly includes geometry optimization of low-energy (isomeric) structures, calculation of vibrational modes and electronic transitions, and generation of predicted excitation spectra (i.e. frequencies vs. oscillator strengths). The calculated absorption spectra can be closely compared to the experimental action spectra to elucidate the predominant ion structures in the gas phase. Other analytical methods such as hydrogen-deuterium exchange experiments,[21] ion-molecule reactions,[22] and IR action spectroscopy[23] have also been employed to complement the structure assignments from UV action spectroscopy experiments. In recent reports, UV action spectroscopy was involved in the investigation of transient intermediate structures, and was able to characterize the atomic arrangements, 3D conformations, and charge/spin densities of peptide and DNA cation radicals. These studies will be further described in the following chapters.

1.6 Detection Methods

So how are all of these gas-phase ions measured to generate mass spectra? After being generated in the ionization source and isolated and/or fragmented in the mass analyzer, ions of desired *m/z* are often sent towards a detection system to track their relative abundances. Detection methods such as Faraday cups and electron multipliers have been integrated into mass spectrometers for this purpose. Compared to Faraday cups, electron multipliers operate with quicker response times and are thus better suited for more modern, fast scanning ion trap mass spectrometers. Since the remaining content in this text primarily involves the investigation of cation species, analyte “ions” will henceforth refer to positively-charged molecules.

For enhanced sensitivity, electron multipliers can implement a creative signal-amplification mechanism to serve as excellent ion detecting systems for mass spectrometers.

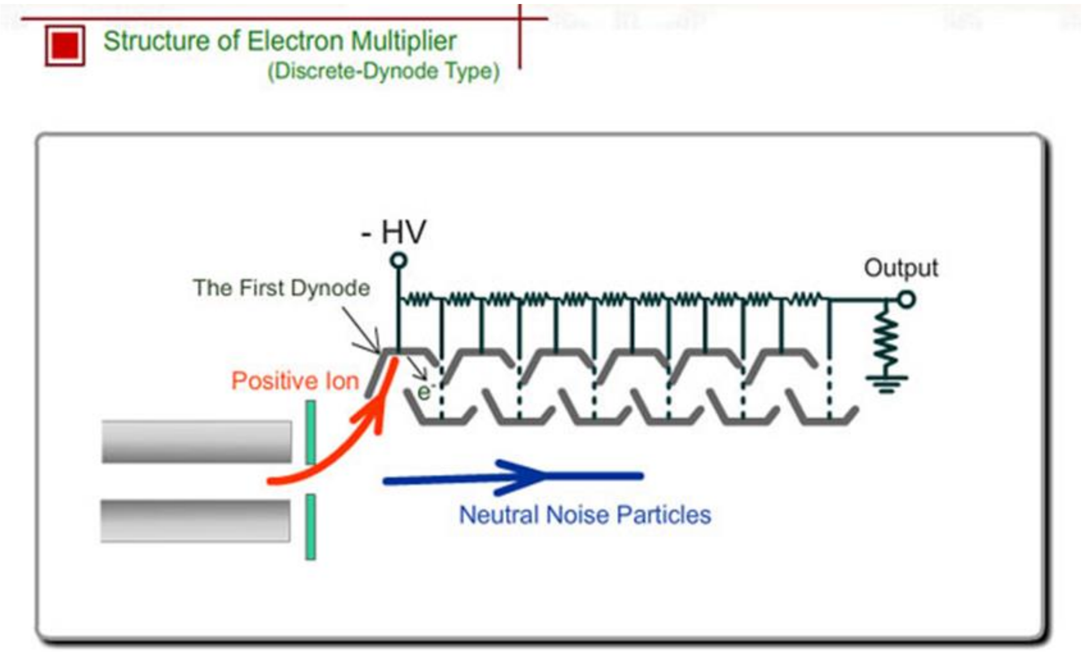

Figure 12. Schematic of signal amplification with an electron multiplier for ion detection. Image from: https://www.ssi.shimadzu.com/products/gas-chromatography-mass-spectrometry/structure_electron.html.

Gas-phase ions leaving a mass analyzer can be attracted to the electron multiplier, striking the surface and causing electron ejection (**Fig. 12.**). These electrons, sometimes referred to as secondary electrons, can then be attracted towards the output electrode via a positively-increasing applied potential. The physical shape of the electron multiplier can cause the secondary electrons to undergo additional surface collisions, generating more secondary electrons which contribute to the avalanching signal that eventually reaches the output electrode. In this manner, electron multipliers can amplify an ion signal with gains of up to multiple magnitudes (~ 10^6).[24] The number of electrons ejected (and detected) are representative of the ion abundance, and these signals can be sent to a computer system to be processed by a software program for mass spectra generation.

In the following chapters, the majority of the experimental results collected and discussed are from mass spectrometers that utilize electrospray ionization (ESI), 2D and 3D ion trap mass analyzers, and electron multiplier detectors for the characterization of positively-charged ions. Now that the basics of mass spectrometry have been addressed, let's explore some fascinating studies that exhibit the utility of new MS^n methods implementing UV action spectroscopy for the structural analysis of biologically- and environmentally-relevant transient intermediates.

1.7 References

1. Griffiths, J. A Brief History of Mass Spectrometry. *Anal. Chem.* 2008, 80, 5678-5683.
2. Borman, S.; Russell, H.; Stuzdak, G. A Mass Spec Timeline. *Today's Chemist at Work.* 2003, 47-49.
3. McLafferty, F.W.; Tureček, F. Interpretation of Mass Spectra: Fourth Edition; University Science Books, 1993; pp 6-11, 103-112.
4. Choi, K.M.; Yoon, S.H.; Sun, M.; Oh, J.Y.; Moon, J.H.; Kim, M.S. Characteristics of Photodissociation at 193 nm of Singly Protonated Peptides Generated by Matrix-Assisted Laser Desorption Ionization (MALDI). *J. Am. Soc. Mass. Spectrom.* 2006, 17, 1643-1653.

5. Cody, R.B.; Tamura, J.; Musselman, B.D. Electrospray Ionization/Magnetic Sector Mass Spectrometry: Calibration, Resolution, and Accurate Mass Measurements. *Anal. Chem.* 1992, 64, 1561-1570.
6. Korn, J. A.; Urban, J.; Dang, A.; Nguyen, H. T. H.; Tureček, F. UV-Vis Action Spectroscopy Reveals a Conformational Collapse in Hydrogen-Rich Dinucleotide Cation Radicals. J. Phys. Chem. Lett. 2017, 8, 4100−4107.
7. Nguyen, H. T., Shaffer, C. J., & Tureček, F. Probing Peptide Cation–Radicals by Near-UV Photodissociation in the Gas Phase. Structure Elucidation of Histidine Radical Chromophores Formed by Electron Transfer Reduction. *J. Phys. Chem. B*. 2015, 119(10), 3948-3961.
8. Dang, A.; Nguyen, H. T. H.; Ruiz, H.; Piacentino, E.; Ryzhov, V.; Tureček, F. Experimental Evidence for Noncanonical Thymine Cation Radicals in the Gas Phase. *J. Phys. Chem. B*. 2018, 122, 86−97.
9. Dang, A.; Korn, J.; Gladden, J.; Mozzone, B.; Tureček, F. UV-Vis Photodissociation Action Spectroscopy on Thermo LTQ-XL ETD and Bruker amaZon Ion Trap Mass Spectrometers: A Practical Guide. *J. Am. Soc. Mass. Spectrom*. 2019, DOI: 10.1007/s13361-019-02229-z.
10. Wells, J. M.; McLuckey, S. A. Collision-Induced Dissociation (CID) of Peptides and Proteins. *Methods in Enzymology*. 2005, 402, 148-185.
11. Shaffer, C.J.; Marek, A.; Pepin, R.; Slováková, K.; Tureček, F. Combining UV Photodissociation with Electron Transfer for Peptide Structure Analysis. *J. Mass. Spectrom*. 2015, 50, 470-475.

12. Dang, A.; Liu, Y.; Tureček, F. UV-Vis Action Spectroscopy of Guanine, 9-Methylguanine, and Guanosine Cation Radicals in the Gas Phase. *J. Phys. Chem. A*. 2019, 123, 3272-3284.
13. Tureček, F., Julian, R. R. Peptide radicals and cation radicals in the gas phase. *Chem. Rev*. 2013, 113(8), 6691-6733.
14. Liu, Y.; Korn, J. A.; Dang, A.; Tureček, F. Hydrogen-Rich Cation Radicals of DNA Dinucleotides. Generation and Structure Elucidation by UV-Vis Action Spectroscopy. *J. Phys. Chem. B*. 2018, 122, 9665−9680.
15. Stedwell, C.N.; Polfer, N.C. Spectroscopy and the Electromagnetic Spectrum. Polfer, N.C.; Dugourd, P.; Eds. *Laser Photodissociation and Spectroscopy of Mass-separated Biomolecular Ions. Lecture Notes in Chemistry, Vol. 83.* Springer: Heidelberg, 2013, pp. 1-18.
16. Huang, S.H.; Liu, Y.; Tureček, F. Non-Covalent Complexes of the Peptide Fragment Gly-Asn-Asn-Gln-Gln-Asn-Tyr in the Gas-Phase. Photodissociative Cross-Linking, Born-Oppenheimer Molecular Dynamics, and Ab Initio Computational Binding Study. *Phys. Chem. Chem. Phys.* 2019, DOI: 10.1039/C8CP06893C.
17. Liu, Y.; Tureček, F. Photodissociative Cross-Linking of Diazirine-Tagged Peptides with DNA Dinucleotides in the Gas Phase. *J. Am. Soc. Mass. Spectrom.* 2019, DOI: 10.1007/s13361-019-02189-4.
18. Brodbelt, J.S. Photodissociation Mass Spectrometry: New Tools for Characterization of Biological Molecules. *Chem. Soc. Rev.* 2014, 43(8), 2757-2783.
19. Barbatti, M.; Aquino, A.J.A.; Lischka, H. The UV Absorption of Nucleobases: Semi-Classical Ab Initio Spectra Simulations. *Phys. Chem. Chem. Phys*. 2010, 12, 4959-4967.

20. Tureček, F. Benchmarking Electronic Excitation Energies and Transitions in Peptide Radicals. *J. Phys. Chem. A.* 2015, 119, 10101-10111.

21. Dang, A.; Shaffer, C.J.; Bim, D.; Lawler, J.; Lesslie, M.; Ryzhov, V.; Tureček, F. Near-UV Water Splitting by Cu, Ni, and Co Complexes in the Gas Phase. *J. Phys. Chem. A.* 2018, 122, 2069-2078.

22. Dang, A.; Nguyen, H.T.; Ruiz, H.; Piancentino, E.; Ryzhov, V.; Tureček, F. Experimental Evidence for Noncanonical Thymine Cation Radicals in the Gas Phase. *J. Phys. Chem. B.* 2018, 122, 86-97.

23. Lesslie, M.; Lawler, J. T.; Dang, A.; Korn, J. A.; Bím, D.; Steinmetz, V.; Maitre, P.; Tureček, F.; Ryzhov, V. Cytosine Radical Cation: A Gas-Phase Study Combining IRMPD Spectroscopy, UVPD Spectroscopy, Ion−Molecule Reactions, and Theoretical Calculations. *ChemPhysChem*. 2017, 18, 1293−1301.

24. Mellon, F.A. Mass Spectrometry/Principles and Instrumentation. *Encyclopedia of Food Sciences and Nutrition: Second Edition.* 2003, pp. 3739-3749.

Chapter 2: UV-Vis Photodissociation Action Spectroscopy on Thermo LTQ-XL ETD and Bruker amaZon Ion Trap Mass Spectrometers

Reproduced in part with permission from Dang, A.; Korn, J.; Gladden, J.; Mozzone, B.; Tureček, F. Journal of the American Society for Mass Spectrometry. 2019, DOI: 10.1007/s13361-019-02229-z.

Abstract

We report automated procedures for multiple tandem mass spectra acquisition allowing UV-Vis photodissociation action spectroscopy measurements of ions and radicals. The procedures were developed for two commercial ion trap mass spectrometers and applied to collision-induced and electron-transfer dissociation tandem mass spectrometry modes of ion generation.

2.1 Introduction

Action spectroscopy refers to tandem mass spectrometry methods in which wavelength dependent photodissociative formation of fragment ions is used to determine the absorption properties of the precursor ion.[1-3] This approach to ion structural analysis was pioneered by Dunbar,[4] Beauchamp,[5] Freiser,[6] and Gaumann,[7] using ion-cyclotron resonance in Penning ion traps. Photodissociation and ion spectroscopy has also been performed on beam instruments[8,9] that are less readily adaptable to experiments for multistage ion preparation and analysis (MS^n). The different types of mass spectrometers used to obtain action spectra have been reviewed[3]. More recently, special ion traps have been designed and implemented for various types of action spectroscopy.[10-13] The Thermo linear ion trap (LTQ) has been adapted to allow photodissociation[14-17] and action spectroscopy measurements.[18,19] Recently, the Bruker amaZon

3D-ion trap has been adapted for infra-red multiphoton action spectroscopy (IRMPD) measurements using photons from a free-electron laser.[20] We have adapted both an LTQ-XL and an amaZon-Speed ion traps, which are both equipped with auxiliary ion sources for electron-transfer dissociation, to allow measurements of UV-visible action spectra of radical ions in the MS^n format where the precursor ions to be studied are generated by CID[21,22] or ETD.[23-24] We have developed automated data acquisition protocols that greatly facilitate action spectroscopy measurements and increase safety when handling the excitation lasers. In this Application Note, we wish to summarize our experience with operating both instruments in the action spectroscopy mode and also provide detailed protocols for UV-Vis action spectra measurements.

2.2 Design

2.2.1 Laser

An Nd-YAG EKSPLA NL301G laser (Altos Photonics, Bozeman, MT, USA) was used to generate a beam of photon pulses at 20 Hz frequency and 3-6 ns pulse width. The photon pulses were directed into a PG142C unit (Altos Photonics, Bozeman, MT, USA) which incorporated a third harmonic generator and optical parametric oscillator coupled with an optional second harmonic generator to enable wavelength tuning between 210-700 nm. The laser beam (6-mm diameter) exiting the PG142C unit was aligned and focused into the ion trap of the modified mass spectrometer by a series of mirrors, optical posts, and telescopic lenses (ThorLabs, Newton, NJ, USA) to achieve photodissociation of isolated ions. A fast steering mirror (Newport Corporation, Irvine, CA, USA) was eventually implemented in the Bruker optical setup to improve beam alignment and UVPD reproducibility. The laser pulse energies, typically ranging from 0.2-4.0 mJ, were measured at each experimental UVPD wavelength using an EnergyMax-USB J-10MB energy sensor (Coherent Inc., Santa Clara, CA, USA) to calibrate the action spectra. The optical setups also enabled the option of UVPD using a higher-powered (~12-15 mJ) single-wavelength 355 nm beam, which exited the PG142C unit from a different output beam path and hence required a separate set of optical alignment components (i.e. optical flip mount, mirrors with higher damage-thresholds). All mentioned laser components and mass spectrometers were set on optical tables to maximize laser alignment and experimental reproducibility.

2.2.2 LTQ Hardware

To provide optical access into the linear ion trap of the LTQ-XL ETD mass spectrometer (Thermo Fisher Scientific, San Jose, CA, USA), a 1-mm diameter hole was drilled into the insert block of the auxiliary chemical ionization source used for anion production, and the backside vacuum gate to the chemical ionization source was replaced by an aluminum plate with a sealed quartz window in position of the incoming beam path (Figure 1). The sample solution was electro-sprayed into the instrument's front-end inlet, the desired ions generated by MS^n-ETD and/or CID were isolated in the linear ion trap, then synchronized pulses of photons were sent into the mass spectrometer through the backside quartz window and past the chemical ionization source to induce MS^n photo-dissociation of isolated ions in the linear ion trap.

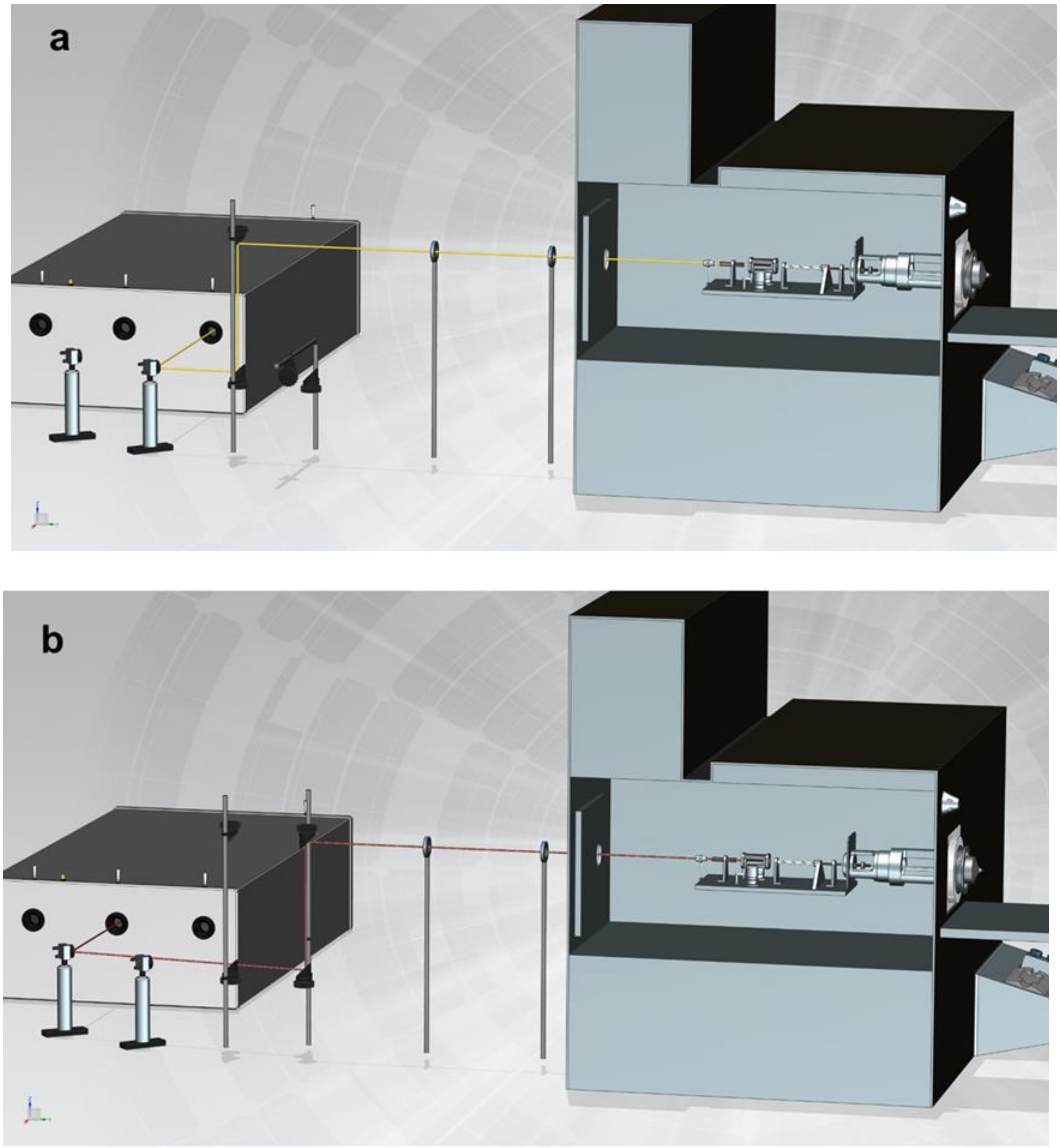

Figure 1. Optical setup and modifications of Thermo LTQ mass spectrometer for MS^n-UVPD and automated action spectroscopy, displaying (a) tunable 210-700 nm and (b) single-wavelength 355 nm capabilities using optical flip-mount.

2.2.3 LTQ Software

Tandem MS^n-UVPD on the LTQ-XL ETD was achieved by interfacing the tunable laser system to the mass spectrometer using LabView software (National Instruments, Austin, TX, USA) and by exploiting auxiliary features of the LTQ console. Specifically, pin-14 of the J1 connector on the LTQ was wired to a digital I/O device (National Instruments, Austin, TX, USA) connected to the operating PC. Additionally, the NL301G laser and PG142C unit were linked to the operating PC via USB-to-CAN connections. For every MS^n-activation (i.e. ETD, CID, UVPD) during an MS^n-UVPD sequence scan, a TTL pulse from pin-14 was sent to the digital I/O device which relayed the signal to a LabView code to synchronize the pump laser to pulse (or not pulse) photons at that activation. This LabView code ("LV1,") used LabView drivers provided by EKSPLA to control the photon pulses at specified settings (i.e. pulse energy, number of pulses per activation, number of MS^n activations). For ETD and/or CID (i.e. "non-UVPD") activations in the MS^n sequence, a "0 %" pulse energy was implemented via LV1. Instrumental MS^n sequence scan conditions including mass-to-charge ratios of desired ions, isolation widths, MS^n activation times, and sample flow rate were set using the ThermoTunePlus program; for a UVPD activation, a CID activation was set in its place at "0" collision energy. The experimental UVPD wavelength was manually set via the laser system's control pad.

Action spectroscopy involving automated MS^n photo-activation sequence scans at incremental wavelengths was achieved via Xcalibur software (ThermoElectron Fisher, San Jose, CA, USA), LV1 and additional LabView codes, and by exploiting the built-in contact closure connection on the LTQ console (for HPLC autosampler interfacing) along with feedback from the laser. In particular, the "Start In" and "Ready Out" ports on the LTQ's "Peripheral Control" interface were wired to a switchbox and digital I/O device (mentioned above) connected to the operating PC. After completion of MS^n-UVPD sequence scans (with photon settings specified using LV1) at the first desired wavelength of an action spectroscopy experiment, the LTQ's contact closure would trigger a "Ready" signal that was received by a second LabView code ("LV2,") which stepped the laser wavelength, waited, then changed the status of the contact closure to trigger the LTQ to start the MS^n-UVPD sequence scans at the next wavelength in the action spectrum. These steps were continuously repeated until the MS^n-UVPD scans for the last specified wavelength were completed. Automated photo-activation settings including starting/ending wavelength and step size were controlled via LV2, which utilized drivers provided by EKSPLA. Automated MS^n sequence scan conditions such as mass-to-charge ratios of desired ions, MS^n activation times, and sample flow rate were set using Xcalibur software, which was also used to facilitate the automated data acquisition process and contact closure status. A third LabView code ("LV3,") incorporating the EnergyMax-USB J-10MB energy sensor utilized drivers provided by Coherent and EKSPLA to perform automated power scans for more efficient spectra calibration. The automated MS^n-UVPD raw data was extracted from Xcalibur output files and exported to Excel, along with automated power scan measurements, to plot experimental action spectra.

2.2.4 Bruker Hardware

To provide optical access into the 3-D ion trap of the Bruker amaZon Speed mass spectrometer (Bruker Daltonics, Billerica, MA, USA), two 1-mm holes were drilled into the ring electrode (i.e. one in the top-center, another in the bottom-center), and the vacuum housing lid directly above the modified ring electrode was replaced with an optical breadboard containing a mounted mirror, lens, and two sealed UV windows; two mirrors were also fixed beneath the modified ring electrode (Figure 2). The sample solution was electro-sprayed into the instrument's front-end inlet, desired ions generated by MS^n-ETD and/or CID were isolated in the 3-D ion trap, then synchronized pulses of photons were sent into the ion trap through the top of the instrument to achieve MS^n photo-dissociation of ions. Residual photons exited the modified ring electrode through the bottom-centered 1-mm hole and reflected off the two mounted mirrors beneath the 3-D ion trap to exit the mass spectrometer vertically through the second UV window.

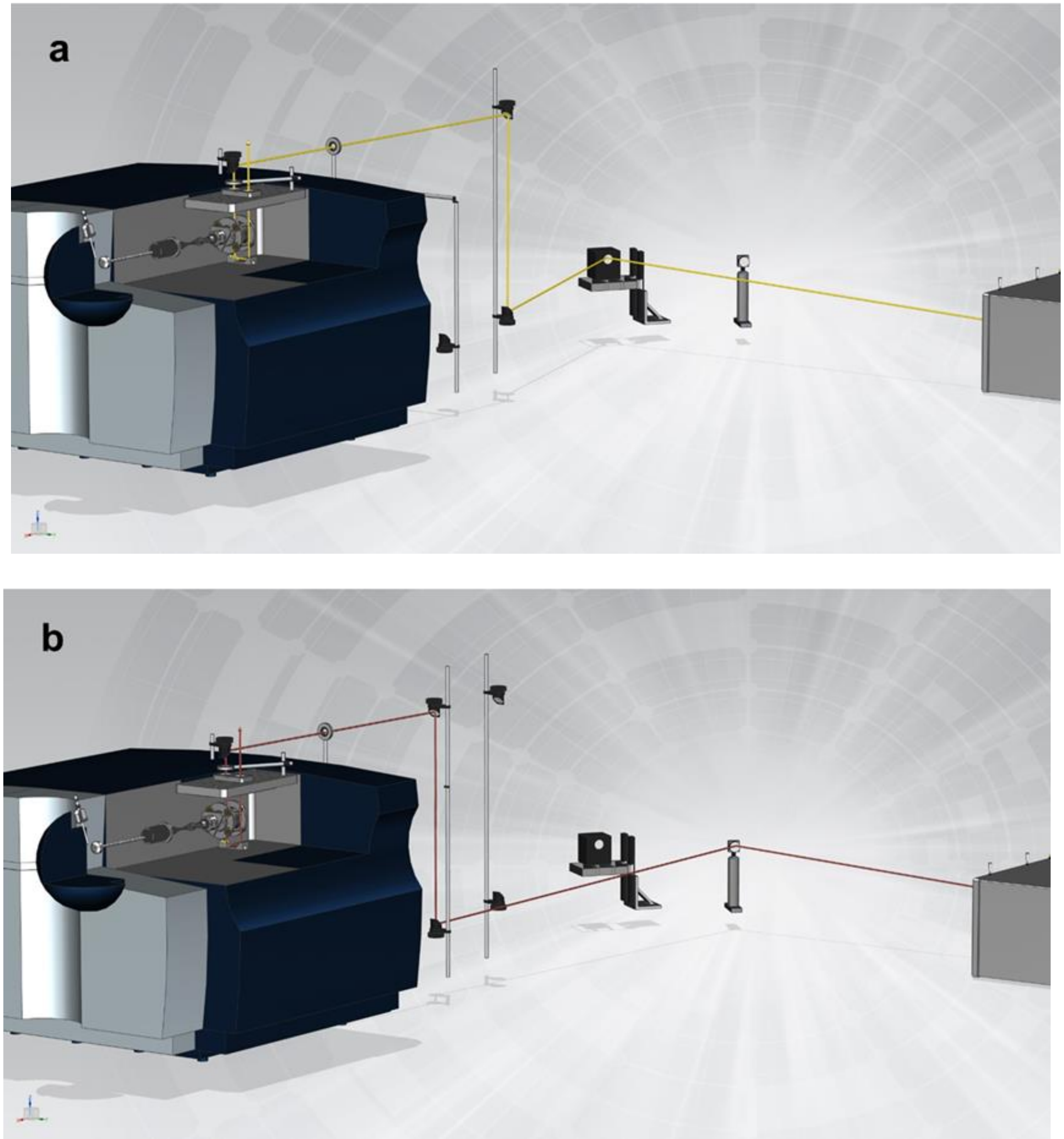

Figure 2. Optical setup and modifications of Bruker amaZon mass spectrometer for MS^n-UVPD and automated action spectroscopy, displaying (a) tunable 210-700 nm and (b) single-wavelength 355 nm capabilities using optical flip-mount. The (a) tunable setup incorporated a fast steering mirror to improve beam alignment and UVPD reproducibility.

2.2.5 Bruker Software

Tandem MS^n-UVPD and automated action spectroscopy on the Bruker amaZon were achieved by interfacing the tunable laser system to the amaZon via LabView software, the XML scripting interface in the Bruker TrapControl program, and by exploiting auxiliary features of the amaZon console. Specifically, pin-17, 26, 29, and 34 from the amaZon's auxiliary interface were wired to a multifunction I/O device (National Instruments, Austin, TX, USA) connected to the operating PC. The NL301G laser and PG142C unit were also linked to the operating PC via USB-to-CAN connections. A LabView code ("LV4,") incorporating drivers from EKSPLA and XML commands (provided by Bruker) first set the mass spectrometer to "slave mode," causing it to wait for an external hardware trigger before starting specified MSn activations; LV4 then activated the multifunction I/O device to send a TTL pulse to pin-17 to initiate the desired MS^n-UVPD/automated action spectroscopy activation sequence(s). For every MS^n-activation (i.e. ETD, CID, UVPD) during an MS^n-UVPD sequence scan, LV4 ordered the amaZon to trigger a TTL pulse from pin-26 to the multifunction I/O device which relayed the signal back to LV4 in order to synchronize the pump laser to pulse (or not pulse) photons at that activation. If performing action spectroscopy, LV4 would step the laser wavelength after completion of a specified set of MS^n scans (while the mass spectrometer would wait in "slave mode"), then trigger pin-17 to start the MS^n-UVPD sequence scans at the next desired wavelength in the action spectrum. These commands were repeated until the last specified wavelength was reached. The XML commands from LV4 were sent to a specified directory linked to the Bruker TrapControl program in order to automate the mass spectrometer at desired settings (i.e. "slave mode," MS^n activation times, external trigger configurations). Tandem MS(n)-UVPD/automated action spectroscopy settings such as starting/ending wavelength, number of wavelengths (i.e. step size), number of scans per wavelength, number of MS^n activations, MS^n activation times, photon pulse energy, and number of photon pulses per MS^n activation were set using LV4. For ETD and/or CID (i.e. “non-UVPD”) activations in the MS^n sequence, a “0 %” pulse energy was implemented via LV4. Additional MS^n sequence scan conditions such as mass-to-charge ratios of desired ions, MS^n isolation/activation settings, and sample flow rate were set using the Bruker TrapControl program; for a UVPD activation, a CID activation was set in its place at “0” collision energy. A fast steering mirror controlled using another LabView code (“LV5,”) was implemented in the optical setup to improve beam alignment and UVPD reproducibility. Like with the LTQ, LV3 (described above) was again used to perform automated power scans for more efficient spectra calibration. The automated MSn-UVPD raw data was extracted from Bruker’s Compass Data Analysis program using a data-extraction XML method (provided by Bruker), and was exported to Excel along with automated power scan measurements to generate experimental action spectra. Although the present application has been developed to obtain UV-Vis action spectra, the authors believe the this software interface can be applied to any tunable laser system that has the drivers and USB/PC connections needed to communicate and be controlled by LabView.

2.3 Experimental Results and Discussion

To compare the performance of the new automated action spectroscopy methods on the different modified mass spectrometers, we first present the MS^2-UVPD spectra of doubly protonated dGG dinucleotides (*m/z* 299) that were generated on the Bruker amazon and Thermo LTQ (Figure 3a and 3b, respectively). The Bruker spectrum was obtained for the *m/z* 152 photofragmentation channel, whereas the LTQ spectrum was expressed as a sum of photofragment intensities. The spectra are remarkably similar, showing the overlapping bands of $\pi \rightarrow \pi^*$ transitions in the guanine rings with a center at 270 nm.[25,26] To illustrate a more sophisticated experiment, we present the MS^3-ETD-UVPD action spectra of the dinucleotide cation-radical $(GG + 2H)^{+\cdot}$ (*m/z* 598) that were obtained on the Thermo LTQ and the Bruker amaZon. In brief, a sample solution of dinucleotide GG (Integrated DNA Technologies, Coralville, IA) and dibenzo-18-crown-6-ether (Sigma-Aldrich, Milwaukee, WI) in acetonitrile:water:acetic acid (80:20:1) was electro-sprayed into the mass spectrometer, the doubly-charged $(GG + DBCE + 2H)^{2+}$ complex (*m/z* 479) was isolated and subjected to MS^2-

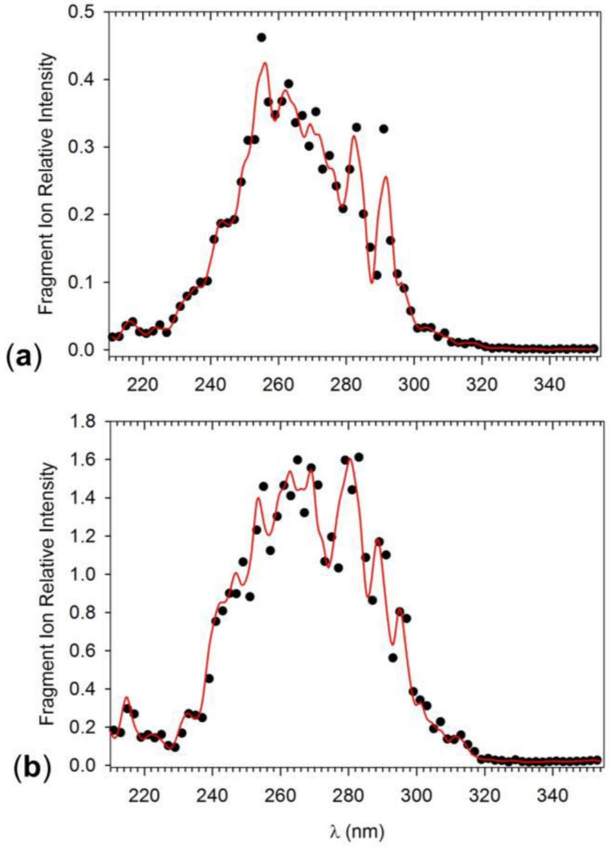

Figure 3. UVPD-MS^2 action spectra of $(dGG + 2H)^{2+}$ *m/z* 299 ions obtained at (a) Bruker amaZon, and (b) Thermo-LTQ.

ETD, then the desired (GG + 2H)$^{+\cdot}$ (m/z 598) cation-radical was isolated and exposed to MS^3-ETD-UVPD at incremental wavelengths (~210-700 nm); the relative intensities of the MS^3 photo-fragments were calibrated with automated power scan measurements and plotted as a function of UVPD wavelength to generate the action spectra.

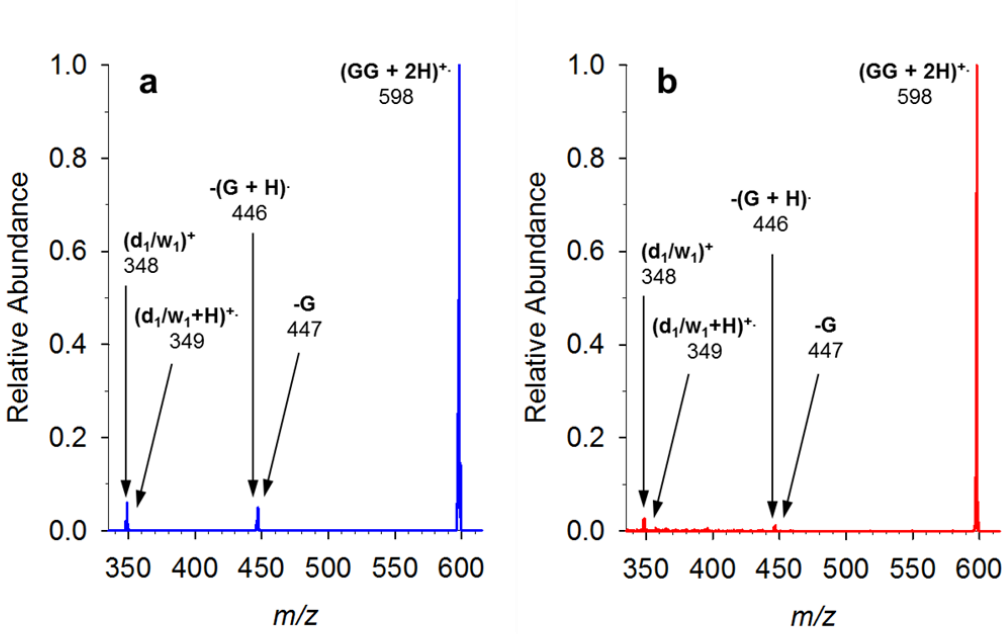

Figure 4. MS^3-ETD-UVPD of dinucleotide cation-radical [GG + 2H]$^{+\cdot}$ *m/z* 598 obtained via automated action spectroscopy on (a) the LTQ (224 nm, 1 pulse) and on (b) the amaZon (223 nm, 1 pulse).

As seen from the MS3-ETD-UVPD mass spectra of the cation-radical (GG + 2H)$^{+\cdot}$ (*m/z* 598) recorded using the LTQ (Figure 4a) and using the amaZon (Figure 4b) at ~220 nm with 1 photon pulse per UVPD activation, the same photo-fragments (*m/z* 348, 349, 446, 447) were produced; these fragment ions were also observed on MS^3-ETD-CID. Although the intensities of the photo-fragments (with respect to the parent ion *m/z* 598) were somewhat higher when performing UVPD on the LTQ, the relative distributions of the photo-fragmentation from both mass spectrometers were comparable. That is, with both the LTQ and the amaZon, the four photo-fragments were represented by two doublet peaks in the MS^3-ETD-UVPD mass spectra (at ~220 nm), with the m/z 348/349 doublet being slightly larger than the *m/z* 446/447 doublet. Furthermore, when comparing the MS^3-ETD-UVPD action spectra of the *m/z* 598 cation-radical using the LTQ (Figure 5a) and the amaZon (Figure 5b), virtually identical absorption trends are observed, with the same major bands at ~220, 275, 330, and 450 nm. The experimentally-obtained action spectra were interpreted with the help of TD-DFT calculations of excited states for structure elucidation of the isolated ions, as reported previously.[27]

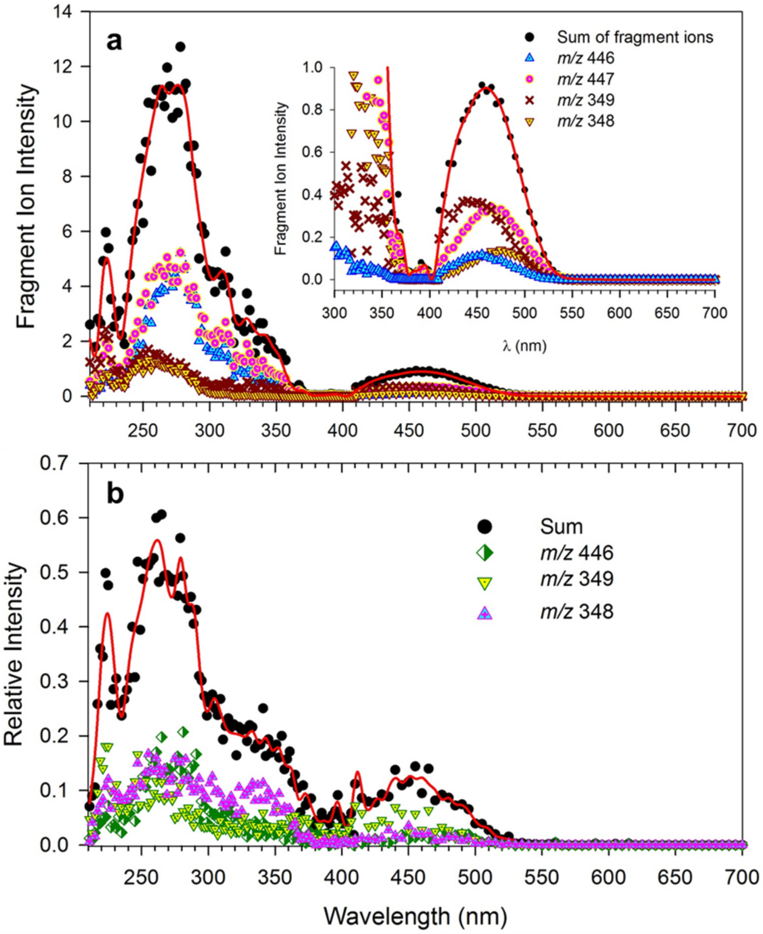

Figure 5. MS^3-ETD-UVPD action spectra of dinucleotide cation-radical $[GG + 2H]^{+\cdot}$ *m/z* 598 obtained via automated action spectroscopy on (a) the LTQ (with inset zoomed in at ~450 nm band) and on the (b) amaZon.

2.4 Conclusions

Automated MSn-UVPD action spectroscopy can be achieved on modified LTQ and amaZon mass spectrometers for a more efficient and reproducible analysis of gas-phase ions. These commercial mass spectrometers can readily be modified to allow optical access to the ion traps, and can be interfaced to a tunable laser system by exploiting various auxiliary features on the mass spectrometers with different LabView codes. The cation-radical $(GG + 2H)^{+\cdot}$ (*m/z* 598) analyzed via automated action spectroscopy on both mass spectrometer/laser systems exhibited comparable photo-fragmentation trends and MS^n photodissociation action spectra.

2.5 Acknowledgments

Financial support of this research has been provided by the NSF Chemistry Division (Grant CHE-1661815). These projects would not have been possible without help and advice from Graeme McAlister and John Syka (ThermoElectron Fisher, San Jose, CA, USA) and Christoph Gebhardt (Bruker Daltonik, GmbH, Bremen, Germany). Thanks are also due to Christopher J. Shaffer and Robert Pepin for technical assistance and contributions.

2.6 References

1. Eyler, J.R.: Infrared multiple photo dissociation spectroscopy of ions in Penning traps. *Mass Spectrom. Rev*. 2009, 28, 448-467.
2. Polfer, N.C.: Infrared multiple photon dissociation spectroscopy of trapped ions. *Chem. Soc. Rev*. 2011, 40, 2211-2221.
3. Antoine, R., Dugourd, P.: UV-Visible Activation of Biomolecular Ions. In Laser Photodissociation and Spectroscopy of Mass-separated Biomolecular Ions, Polfer, N.C.;

Dugourd, P., Eds., Lecture Notes in Chemistry, Vol. 83, Springer: Heidelberg, 2013, pp. 93-116.

4. Dunbar, R.C.: Photodissociation of the methyl chloride (CH_3Cl^+) and nitrous oxide (N_2O^+) cations. *J. Am. Chem. Soc*. 1971, 93, 4354–4358.
5. Casassa, M.P., Bomse, D.S., Beauchamp, J.L., Janda, K.C.: Infrared photochemistry of ethylene clusters. *J. Chem. Phys*. 1980, 72, 6805–6806.
6. Carlin, T.J., Freiser, B.S.: Multiphoton ionization in Fourier transform mass spectrometry. *Anal. Chem*. 1983, 55, 955–958.
7. Bensimon, M., Rapin, J., Gaumann, T.: Comparison of infrared photodissociation in a Fourier transform mass spectrometer with metastable ion decay in a double-focusing mass spectrometer. *Int. J. Mass Spectrom. Ion Process*. 1986, 72, 125–135.
8. Willey, K.F., Robbins, D.L., Yeh, C.S., Duncan, M.A.: Laser photodissociation spectroscopy of mass-selected metal clusters. *Faraday Discuss*. 1992, 92, 269-277.
9. Kirketerp, M.-B.S., Nielsen, S.B.: Absorption spectrum of isolated tris(2,2'-bipyridine)ruthenium(II) dications in vacuo. *Int. J. Mass Spectrom*. 2010, 297, 63-66.
10. Fujihara, A., Matsumoto, H., Shibata, Y., Ishikawa, H., Fuke, K.: Photodissociation and spectroscopic study of cold protonated dipeptides. *J. Phys. Chem. A*. 2008, 112, 1457-1463.
11. Feraud, G., Broquier, M., Dedonder-Lardeux, C., Gregoire, G., Soorkia, S., Jouvet, C.: Photofragmentation spectroscopy of cold protonated aromatic amines in the gas phase. *Phys. Chem. Chem. Phys*. 2014, 16, 5250-5259.

12. Kamariotis, A., Boyarkin, O. V., Mercier, S. R., Beck, R. D., Bush, M. F., Williams, E. R., Rizzo, T. R.: Infrared spectroscopy of hydrated amino acids in the gas phase: Protonated and lithiated valine. *J. Am. Chem. Soc.* 2006, 128, 905-916.
13. Kamrath, M. Z., Garand, E., Jordan, P. A., Leavitt, C. M., Wolk, A. B., Van Stipdonk, M. J., Miller, S. J., Johnson, M.A.: Vibrational characterization of simple peptides using cryogenic infrared photodissociation of H2-tagged, mass-selected Ions. *J. Am. Chem. Soc*. 2011, 133, 6440-6448.
14. Ly, T., Julian, R. R.: Residue-specific radical-directed dissociation of whole proteins in the gas phase. *J. Am. Chem. Soc*. 2008, 130, 351-358.
15. Ledvina, A.R., Beauchene, N.A., McAlister, G.C., Syka, J.E.P., Schwartz, J.C., Griep-Raming, J., Westphall, M.S., Coon, J.J.: Activated-ion electron transfer dissociation improves the ability of electron transfer dissociation to identify peptides in a complex mixture. *Anal. Chem*. 2010, 82 10068–10074.
16. Nguyen, H. T. H., Shaffer, C. J., Ledvina, A., Coon, J. J., Tureček, F.: Serine effects on collision-induced dissociation and photodissociation of peptide cation radicals of the $z^{+\cdot}$ type. *Int. J. Mass Spectrom*. 2015, 378, 20-30.
17. Shaffer, C.J.,Marek, A., Pepin, R., Slováková, K., Tureček, F.: Combining UV photodissociation with electron transfer for peptide structure analysis. *J. Mass Spectrom*. 2015, 50, 470–475.
18. Shaffer, C. J.; Pepin, R.; Tureček, F. Combining UV Photodissociation Action Spectroscopy with Electron Transfer Dissociation for Structure Analysis of Gas-Phase Peptide Cation-Radicals. *J. Mass Spectrom*. 2015, 50, 1438-1442.

19. Nguyen, H. T. H.; Shaffer, C. J.; Pepin, R.; Tureček, F.: UV Action Spectroscopy of Gas-Phase Peptide Radicals. *J. Phys. Chem. Lett*. 2015, 6, 4722-4727.
20. Martens, J.; Berden, G.; Gebhardt, C. R.; Oomens, J.: Infrared ion spectroscopy in a modified quadrupole ion trap mass spectrometer at the FELIX free electron laser laboratory. *Rev. Sci. Instrum*. 2016, 87, 103108/1-103108/8.
21. Lesslie, M., Lawler, J. T., Dang, A., Korn, J. A., Bím, D., Steinmetz, V., Maitre, P., Tureček F., Ryzhov, V.: Cytosine radical cation: a gas-phase study combining IRMPD spectroscopy, UV-PD spectroscopy, ion-molecule reactions, and theoretical calculations. *ChemPhysChem* 2017, 18, 1293-1301.
22. Brunet, C., Antoine, R., Allouche, A.-R., Dugourd. P.: Gas phase photo-formation and vacuum UV photofragmentation spectroscopy of tryptophan and tyrosine radical-containing peptides *J. Phys. Chem. A*. 2011, 115, 8933-8939.
23. Brodbelt, J.S.: Photodissociation mass spectrometry: new tools for characterization of biological molecules. *Chem. Soc. Rev*. 2014, 43, 2757–2783.
24. Cannon, J.R., Holden,D.D., Brodbelt, J.S.: Hybridizing ultraviolet photodissociation with electron transfer dissociation for intact protein characterization. *Anal. Chem*. 2014, 86, 10970-10977.
25. Barbatti, M., Aquino, A.J.A., Lischka, H. The UV absorption of nucleobases: semi-classical ab initio spectra simulations. *Phys. Chem. Chem. Phys*. 2010, 12, 4959-4967.
26. Dang, A., Liu, Y., Tureček, F. UV-Vis action spectroscopy of guanine, 9-methylguanine and 2'-deoxyguanosine cation radicals in the gas phase. *J. Phys. Chem. A*. 2019, 123, DOI:10.1021/acd.jpca.9b01542.

27. Liu, Y., Korn, J.A., Dang, A., Tureček, F.: Hydrogen-rich cation radicals of DNA dinucleotides. Generation and structure elucidation by UV-Vis action spectroscopy. *J. Phys Chem. B*. 2018, 122, 9665-9680.

Chapter 3: UV-Vis Action Spectroscopy of Guanine, 9-Methylguanine, and Guanosine Cation Radicals in the Gas Phase

Reproduced in part with permission from Dang, A,; Liu, Y.; Tureček. F. The Journal of Physical Chemistry A. 2019, 123, 3272-3284.

Abstract

Cation radicals of guanine ($G^{+\cdot}$), 9-methylguanine ($MG^{+\cdot}$), and guanosine ($rG^{+\cdot}$) were generated by dissociative oxidation of gas-phase copper complexes and characterized by UV−vis photodissociation action spectra and ab initio calculations. Comparison of the action spectra of $G^{+\cdot}$ with the calculated vibronic absorption spectra of several cation radical tautomers showed the best match for the canonical 6-oxo-N-9-H structure ($G1^{+\cdot}$). The formation of $G1^{+\cdot}$ was favored by the stability of its precursor Cu^{II} ion complexes in solution and the gas phase. $G1^{+\cdot}$ was the marginally lowest-energy guanine tautomer according to CCSD(T) calculations extrapolated to the complete basis set limit (CBS). A canonical 6-oxo structure ($MG1^{+\cdot}$) was also assigned to the 9-methylguanine cation radical on the basis of a match between the action spectrum and the calculated vibronic absorption spectra. $MG1^{+\cdot}$ was calculated by CCSD(T)/CBS to be marginally less stable than the 6-OH enol tautormer, but its formation was favored by the superior stability of its precursor Cu^{II} ion complexes in solution and the gas phase. Action spectroscopy allowed us to assign the canonical 6-oxo structure ($rG1^{+\cdot}$) to the gas-phase guanosine cation radicals that were formed as the lowest-energy tautomers. The absorption bands in the action spectra were assigned on the basis of time-dependent density functional theory calculations that were benchmarked on equation-of-motion coupled cluster calculations of $G^{+\cdot}$.

3.1 Introduction

Ionization of nucleic acids with high-energy electrons and photons creates transient cation radicals that undergo fast transformations by electron transfer followed by chemical reactions, resulting in the complex process of DNA damage.[1] Spontaneous electron transfer in randomly ionized nucleic acids is thought to follow a cascade ending at oxidized guanine as the nucleobase of the lowest ionization energy and oxidation potential.[2−8] DNA ionization and electron transfer kinetics have been studied with oligonucleotide models using ingenious methods,[9,10] including identification of reaction products.[11−14] However, spectroscopic characterization of ionized nucleic acids has been hampered by the transient nature of the primary cation radicals.[15] In a seminal study of adenosine and guanosine, Steenken and Jovanovic showed by fast UV−vis spectroscopy that adenosine and guanosine cation radicals produced by pulse radiolysis underwent rapid deprotonation, forming neutral radicals.[16] Guanosine deprotonation following ionization has also been studied by other methods.[17−21] Electron paramagnetic resonance has been the method of choice, although guanosine radicals and cation radicals have been found difficult to distinguish because of spectra similarity.[17] In contrast to ionization in the condensed phase, proton transfer and other side reactions of nucleobase and nucleoside ions can be controlled in the rarefied gas phase. Nucleobase radicals have been generated by femtosecond electron transfer in the gas phase and characterized by mass spectrometry.[22−24] A major advance in the generation of nucleobase cation radicals has been realized by collision induced intramolecular electron transfer in transition metal complexes in the gas phase. This method has been developed by Chu, Siu, and co-workers for the generation of peptide cation radicals[25] and ingeniously applied by O’Hair,[26] Bohme,[27] and their co-workers to produce nucleobase and nucleoside cation radicals in the gas phase.[28] Ternary complexes of Cu^{II}, nucleobase, and an auxiliary ligand such as 2′,2:6′,2″-terpyridine (terpy) are produced by electrospray ionization[29,30] as doubly charged ions that are selected by mass and activated by collisions with helium in a mass spectrometer. Collision-induced dissociation (CID) breaks up the complex, oxidizing the nucleobase and forming complementary Cu-(terpy)$^+$ and nucleobase cation radical products (Scheme 1) that can be isolated and further characterized by spectroscopy or ion−molecule reactions.[31−34] In particular, infrared multi-photon dissociation (IRMPD) spectroscopy[35,36] has been implemented to determine structures of gas-phase cation radicals of 9-methylguanine,[37] 2′-deoxyguanosine (dG$^{+\cdot}$),[38] and a guanine−cytosine dimer.[39] Recently, UV−vis action spectroscopy[40] has been applied to the characterization of cation radicals of cytosine[41] and thymine.[42] Action spectroscopy relies on wavelength-resolved photodissociation of mass-selected ions whereby the relative intensities of fragment ions are used to reconstruct the absorption bands of the precursor ion.[35,40] Recently, an alternative method of producing cation radicals has been introduced that relies on electron transfer dissociation of doubly charged nucleotide ions[43] that has been combined with UV−vis action spectroscopy, as reported for dAA,[44] chimeric ribonucleotides,[44] dGG, dGC, and dCG dinucleotides.[45] Here we apply UV−vis action spectroscopy to characterize the cation radicals of guanine (G$^{+\cdot}$), 9- methylguanine (MG$^{+\cdot}$), and guanosine (rG$^{+\cdot}$), and we analyze their electronic excitations in the gas phase. We wish to show by experiment and theory that tautomeric forms of guanine-related cation radicals can be distinguished by UV−vis spectra, and we provide their electronic structure and thermodynamic analysis at a high level of theory.

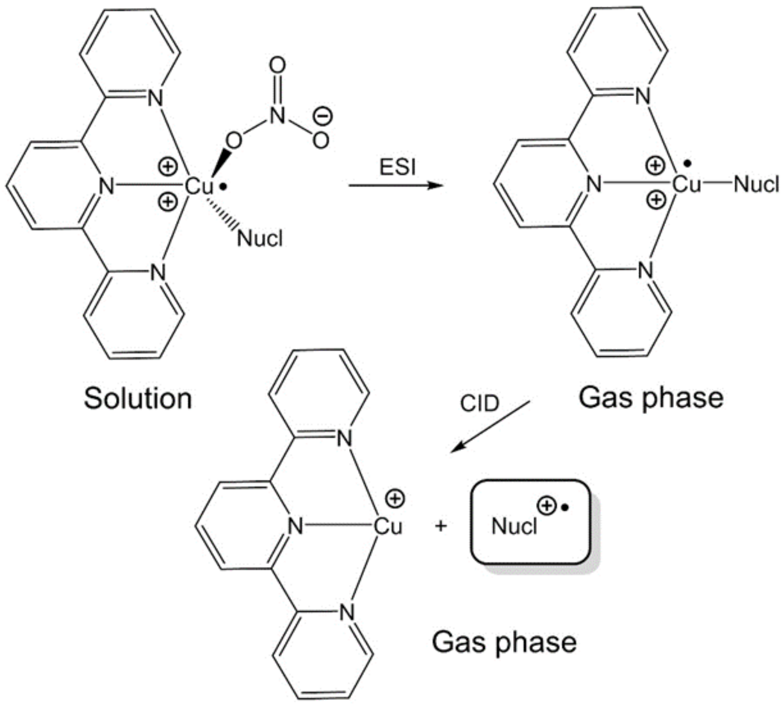

Scheme 1. Formation of gas-phase nucleobase cation radicals.

3.2 Experimental Section

3.2.1 Materials and Methods

Guanine, 9-methylguanine, guanosine, 2′,2:6′,2″-terpyridine, and copper nitrate were purchased from Sigma-Aldrich (St. Louis, MO, USA) and used as received. Complexes were made in situ from equimolar concentrations of the components in 50:50 methanol−water and electrosprayed into a Bruker Daltonik (Bremen, Germany) amaZon Speed 3D ion trap mass spectrometer. The ion trap was modified[46] and equipped with lenses and mirrors to allow irradiation of trapped ions with a laser beam. The beam was generated by an EKSPLA NL301G (Altos Photonics, Bozeman, MT, USA) Nd:YAG laser that was equipped with a PG142C optical parametric oscillator, as described previously for a linear ion trap.[47] A detailed description of the amaZon ion trap laser UVPD instrument will be published elsewhere.

3.2.2 Calculations

Standard ab initio and density functional theory (DFT) calculations were run with the Gaussian 16 program suite (Revision A01).[48] A conformation search of guanosine cation radical structures was performed with Born−Oppenheimer molecular dynamics calculations (BOMD) using the semi-emprirical PM6-D3H4 method[49] run by MOPAC[50] under the Cuby4 platform.[51] This generated 20 ps trajectories from which several low-energy structures were selected and re-optimized with ωB97X-D[52] and M06-2X[53] hybrid density functional methods using the 6-31+G(dp) basis set. Tautomers of $G^{+\cdot}$, $MG^{+\cdot}$, and Cu(terpy) complexes were optimized from initial guess geometries without extensive conformational search. Structures and energies of copper complexes were calculated with CAM-B3LYP,[54] ωB97X-D, and M06-2X DFT methods using the 6-311+G(2d,p) basis set. Solvation energies were calculated with self-consistent reaction field methods using the polarizable continuum model[55] with parameters from Gaussian 16. Additional optimized geometries were obtained with Møller−Plesset calculations,[56] MP2(FULL)/6-31+G- (d,p). The DFT and MP2 geometry optimizations gave very similar structures for individual tautomers of $G^{+\cdot}$, $MG^{+\cdot}$, and $dG^{+\cdot}$ and similar rankings of relative energies. Single-point energies were run on the M06-2X/6-31+G(d,p) optimized geometries with MP2(frozen core) and the aug-cc-pVTZ and aug-cc-pVQZ correlation-consistent basis sets.[57] Another set of single-point energies was obtained with coupled-clusters calculations[58] with single, double, and disconnected triple excitations, CCSD(T)[59] with the aug-cc-pVDZ basis set. Hartree−Fock (HF) and MP2 single-point energies were used to estimate the complete basis set (CBS) limits of correlation energy by fitting with least-squares the formula Ecorr(HF) = a + be−cX, where where X = 2−4 is the ζ split in the aug-cc-pVXZ basis set.[60] Energies extrapolated to the CBS limit were calculated according to the formula E[CCSD(T)/ CBS] = E[HF/aug-cc-pVQZ] + Ecorr(HF, $X \rightarrow \infty$) + E[CCSD(T)/aug-cc-pVDZ] − E[MP2/aug-cc-pVDZ]. Spin projection[61,62] was used to annihilate higher spin states in HF and MP2 calculations. Vertical excitation energies and oscillator strengths of guanine cation radicals were obtained by equation-of-motion coupled-cluster calculations, EOMCCSD[63,64] with the 6-31+G(d,p) basis set. EOM-CCSD energies were calculated for 10 excited states and used to benchmark time-dependent DFT (TD-DFT) calculations[65,66] of several $G^{+\cdot}$ tautomers. On the basis of the benchmarks, we selected UM06-2X/6-31+G(d,p) TD-DFT for calculations of an extensive set of vertical and vibronic transitions in $G^{+\cdot}$, $MG^{+\cdot}$, and $rG^{+\cdot}$. To calculate vibronic excitations, we used 300 Boltzmann-ranked ground-state configurations that were generated by the Newton X program[67] from the harmonic normal modes of each cation radical at 310 K and submitted for TD-DFT calculations. The number of excited states (15− 25) was chosen to include excitations with wavelengths down to below 200 nm, covering the experimental wavelength range of 210−700 nm. Unimolecular rate constants were obtained by Rice−Ramsperger−Kassel−Marcus calculations[68] using the program of Zhu and Hase[69] that was recompiled for Windows.[70]

3.3 Results and Discussion

3.3.1 Cation Radical Generation

Guanine ($G^{+\cdot}$) and 9- methylguanine ($MG^{+\cdot}$) cation radicals were generated in two steps (Scheme 1), which essentially followed the previously reported procedures.[26] In the first step, nucleobase complexes with 2:2′,6’:2″-terpyridine (terpy) and copper nitrate were made in solution and electrosprayed to produce doubly charged 2:2′,6’:2″-terpyridine-Cu-nucleobase complex ions in the gas phase at *m/z* 223.5 and 230.5 for G and MG, respectively, both for the

^{63}Cu isotope. Following mass selection and collisional activation in the ion trap (CID-MS^2), the complexes underwent intramolecular electron transfer that oxidized the nucleobase while dissociating the complex and forming the nucleobase cation radicals at *m/z* 151 and 165 for $G^{+\cdot}$ and $MG^{+\cdot}$, respectively. Because guanine is sparsely soluble, which limits Cu(terpy) complex formation in aqueous solution, the guanine cation radical was also generated from a Cu(terpy) complex with guanosine that upon CID eliminated the sugar moiety to form $[Cu(terpy)G]^{2+\cdot}$ (*m/z* 298.5). This intermediate complex was isolated by mass and subjected to CID-MS^3, forming $G^{+\cdot}$.[33] The guanosine cation radical ($rG^{+\cdot}$) was conveniently generated by CID of a doubly charged gas-phase Cu complex, $(rG)_3Cu^{2+\cdot}$, *m/z* 456, according to the reported procedure.[27,33] The gas-phase ions, $G^{+\cdot}$, $MG^{+\cdot}$, $rG^{+\cdot}$, and their Cu-complex precursors, were characterized by accurate mass measurements and CID mass spectra.

3.3.2 UV-Vis Photodissociation Action Spectra

Photodissociation of $G^{+\cdot}$ produced three main fragment ions at *m/ z* 110 (loss of N=C=NH radical), *m/z* 108 (loss of HN=C=O), and *m/z* 83 (combined loss of N=C−NH and HCN). The mass-resolved fragment ion channels showed different wavelength profiles (Figure 1a−c). The *m/z* 110 channel (Figure 1a) displayed bands with distinct maxima at 295 and 350 nm and broad, lower-intensity bands at 450−560 nm. The *m/z* 108 channel (Figure 1b) exhibited bands with maxima at 295 and 380 nm, with a low-intensity tail extending to ca. 500 nm. The *m/z* 83 channel (Figure 1c) had a major band at 285 nm that coincided with the 295 nm bands of the other fragment ions. In addition, the *m/z* 83 channel showed broad, low-intensity bands at ca. 350 and 410−550 nm. The total action spectrum, produced by summing the fragment ion intensities, is shown in Figure 1d. The action spectra of $G^{+\cdot}$ generated by CID-MS^3 of the $[Cu(terpy)guanosine]^{2+\cdot}$ complex were virtually identical to those shown in Figure 1a−d.

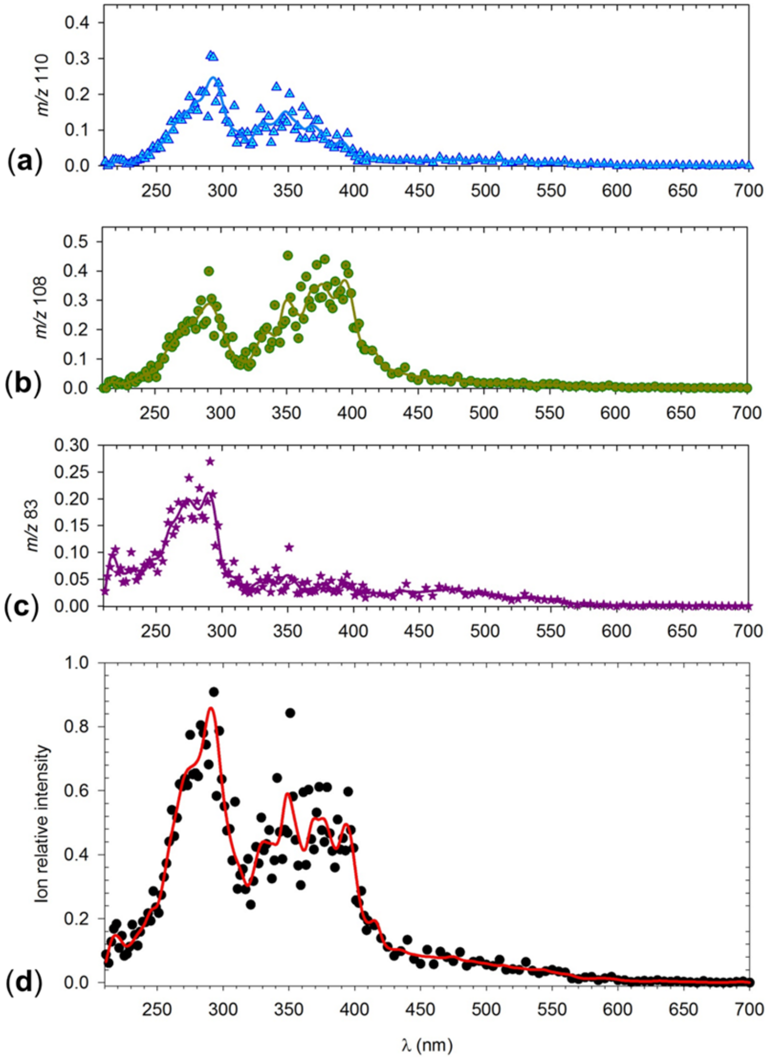

Figure 1. UV−vis photodissociation action spectrum of $G^{+\cdot}$ generated by CID-MS^2 of the $[Cu(terpy)G]^{2+\cdot}$ complex. (a) *m/z* 110 photofragment channel; (b) *m/z* 108 photofragment channel; (c) *m/z* 83 photofragment channel; (d) sum of photofragment ion intensities. The lines are polynomial fits to the data.

Photodisociation of $MG^{+\cdot}$ generated two main fragment ions at *m/z* 138 (loss of HCN) and *m/z* 97 by combined loss of HCN and N=C=NH (Figure 2a). The mass-resolved wavelength profiles showed major bands with maxima at 295 and 350 nm. In addition, the *m/z* 97 channel showed a very weak band at 450−500 nm. Summing the fragment ion intensities produced the total action spectrum shown in Figure 2b.

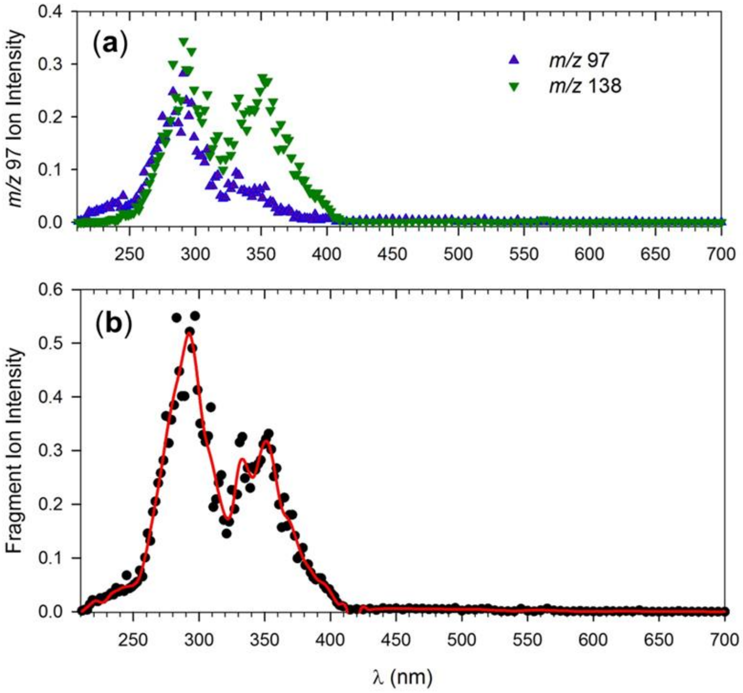

Figure 2. UV−vis photodissociation action spectrum of $MG^{+\cdot}$ generated by CID-MS^2 of the $[Cu(terpy)MG]^{2+\cdot}$ complex. (a) *m/z* 97 and 138 photofragment channels; (b) sum of photofragment ion intensities.

Photodissociation of $rG^{+\cdot}$ resulted in the dominant loss of a ribose $C_5H_8O_4$ neutral fragment forming the $G^{+\cdot}$ ion. The action spectrum displayed two major bands with maxima at 295 and 370 nm and a shoulder at 400 nm extending to 470 nm. There also was a broad, low-intensity band at 530−650 nm with a maximum at 580 nm (Figure 3). Two features of these UV−vis action spectra are noteworthy. First, one-electron oxidation of the guanine ring has a notable effect on light absorption of the cation radicals. The UV−vis spectrum of neutral guanine in the form of 2′-deoxyguanosine phosphate in aqueous solution has two bands at 255 and 275 nm but no absorption above 300 nm.[71] Absorption spectra of gas-phase guanine have not been recorded because of decomposition,[72] but high-level calculations by Barbatti, Lischka, and co-workers indicated guanine absorption bands at 225 and 247 nm.[73] Hence, the bands at $\lambda > 280$ nm that we observed in the UVPD action spectra must be associated with transitions that are typical for the open-shell electronic system of the cation radicals.

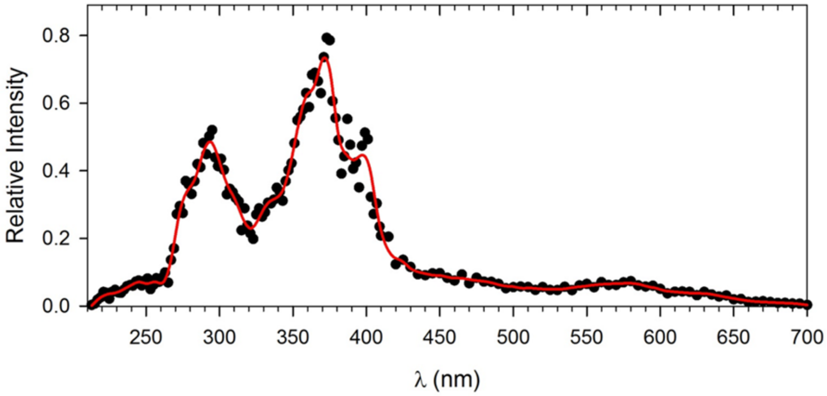

Figure 3. UV−vis photodissociation action spectrum of $rG^{+\cdot}$ generated by CID-MS^2 of the $[Cu(rG)_3]^{2+\cdot}$ complex.

Second, it is noteworthy that the fragment ions formed by photodissociation were the same as those from CID. Because ion excitation by collisions in the ion trap proceeds by stepwise vibrational energy deposition in a slow-heating mode, the observed CID fragment ions represent products of the lowest-energy dissociations accessed on the ground electronic state. The fact that UVPD and CID of guanine-related cation radicals produced similar fragment ions indicated that the excited electronic states from photoexcitation decayed to a vibrationally excited ground electronic state before dissociation. This is consistent with the well-known fast internal conversion of nucleobase excited electronic states, which is considered to be crucial for DNA resistance to UV radiation damage. In particular, guanosine $\pi \rightarrow \pi^*$ excited states were reported to have 2.5−11 ps lifetimes in aqueous solution,[74] while guanine showed 148−360 fs decay times in the gas phase.[75] Our data indicate that fast excited-state conversion also operates in guanine-related cation radicals in the gas phase.

3.3.3 Cation Radical Structures and Relative Energies

To aid the interpretation of the UV−vis action spectra, we carried out extensive calculations that were aimed at three goals. First, we investigated the energetics of guanine and 9-methylguanine Cu(terpy) complexes in water and the gas phase. This was motivated by the mode of cation radical formation in our experiments that involved Cu complexes as precursor ions that were produced from solution and transferred to the gas phase by electrospray ionization. Second, we investigated the relative energies of gas-phase cation radicals of guanine ($G^{+\cdot}$), 9- methylguanine ($MG^{+\cdot}$), 2′-deoxyguanosine ($dG^{+\cdot}$), and guanosine ($rG^{+\cdot}$) to establish their stabilities and potential for isomerization upon CID. We note that the energetics of $MG^{+\cdot}$ and $dG^{+\cdot}$ have been addressed by O'Hair and coworkers using DFT calculations.[37,38] We now extend the energy calculations to the CCSD(T)/CBS level of theory, which is the gold standard for thermochemical calculations. Finally, we use TD-DFT calculations to produce excitation energies and oscillator strengths for several low-energy $G^{+\cdot}$, $MG^{+\cdot}$, and $rG^{+\cdot}$ tautomers to be compared with the UV−vis action spectra. The TD-DFT-calculated spectra were benchmarked on the equation-of-motion CCSD calculations of low-energy $G^{+\cdot}$ tautomers.

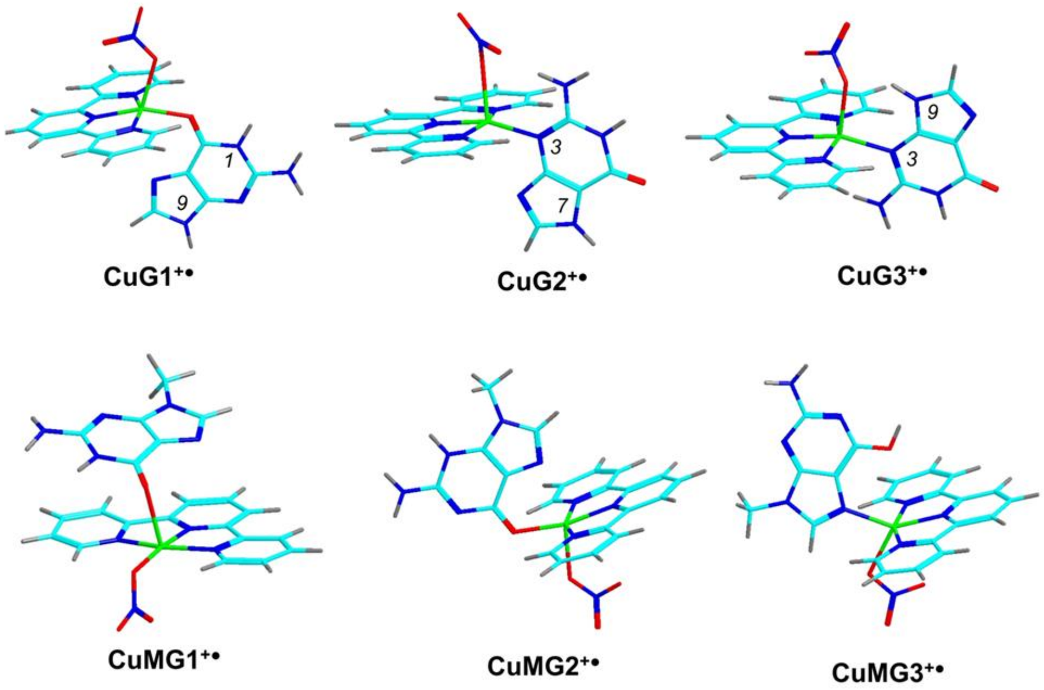

Figure 4. M06-2X/6-311+G(2d,p) optimized structures of $[Cu(terpy)(NO_3)G]^{+\cdot}$ and $[Cu(terpy)(NO_3)MG]^{+\cdot}$ complexes. Atom color coding is as follows: light green = Cu, cyan = C, blue = N, red = O, gray = H.

Table 1. Relative energies of $[\text{guanine}]^{+\cdot}$ isomers.

Ion or Reaction		Relative Energy^{a,b}				
		M06-2X^{c}	ωB97X-D^{d}	PMP2^{c}	CCSD(T)^{c,e}	CCSD(T)^{f}
		6-311++G(2d,p)		aug-cc-pVTZ		CBS
Guan1	$G1^{+\cdot}$	0.0	0.0	0.0	0.0	0.0 (0.0)^{g}
GuanO6-syn	$G2^{+\cdot}$	0.8	8.7	0.0	3.5	2.8 (2.9)
GuanO6-anti	$G3^{+\cdot}$	7.4	15	3.7	9.1	8.6 (9.2)
Guan7	$G4^{+\cdot}$	8.7	9.0	7.2	6.2	5.6 (5.6)
GuanO7	$G5^{+\cdot}$	18	27	15	18	18 (18)
Guan3	$G6^{+\cdot}$	69	68	64		
Guan79	$G7^{+\cdot}$	76	72	66		
Guan36	$G8^{+\cdot}$	66	73	54		
$G1^{+\cdot}$ → *m/z* 108 + HNCO		361	354	336	342	349
$G1^{+\cdot}$ → *m/z* 110 + $HNC{=}N^{\cdot}$		310	325	294	283	271

[a]In kJ mol^{-1}. [b]Including B3LYP/6-31+G(d,p) zero-point energies and referring to 0 K unless stated otherwise. [c]Single-point energies on M06-2X/6-31+G(d,p) optimized geometries. [d]Single-point energies on ωB97X-D/6-31+G(d,p) optimized geometries. [e]Extrapolated single-point energies: E[CCSD(T)/aug-cc-pVTZ)] ≈ E[CCSD(T)/aug-cc-pVDZ)] + E[PMP2/aug-cc-pVTZ)] – E[PMP2/aug-cc-pVDZ)]. [f]Single point energies extrapolated to the complete basis set. [g]Relative free energies at 310 K.

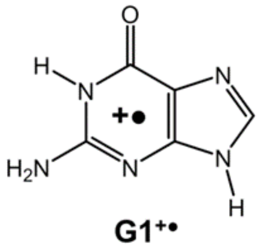
$G1^{+\bullet}$

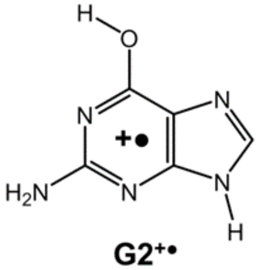
$G2^{+\bullet}$

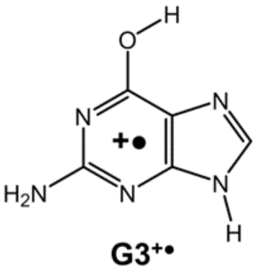
$G3^{+\bullet}$

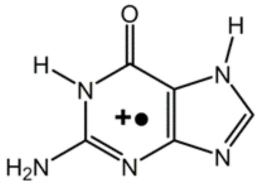
$G4^{+\bullet}$

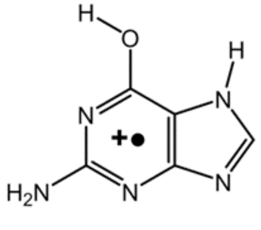
$G5^{+\bullet}$

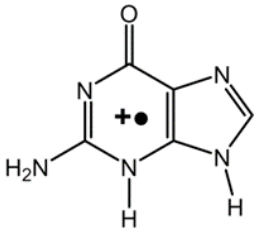
$G6^{+\bullet}$

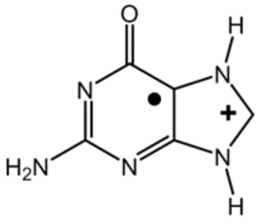
$G7^{+\bullet}$

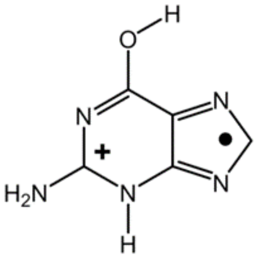
$G8^{+\bullet}$

3.3.4 Guanine Structures and Energies

Structures and relative free energies of aqueous quaternary complexes of guanine tautomers with [Cu(terpy)NO3]$^{+\cdot}$ were obtained by three DFT methods. According to these calculations, guanine preferred binding to [Cu(terpy)NO$_3$]$^{+\cdot}$ as a canonical 6-oxo-N-9-H tautomer (complexes CuG1$^{+\cdot}$ and CuG3$^{+\cdot}$) or as an 6-oxo-N-7-H tautomer (CuG2$^{+\cdot}$), forming low free-energy complexes (Figure 4). Complexes of other guanine 6-oxo tautomers (CuG4$^{+\cdot}$ − CuG8$^{+\cdot}$) were less stable. Binding to [Cu(terpy)NO$_3$]$^{+\cdot}$ of the guanine 6-OH-N-9-H tautomer CuG4$^{+\cdot}$ was ca. 30 kJ mol^{-1} weaker than that for the N-9-H tautomer. DFT calculations of solvated neutral guanine also indicated the 6-oxo-N-9-H and 6-oxo-N-7-H tautomers as the preferred low-free energy structures that are expected to be predominantly represented in aqueous solution to form Cu complexes. According to the calculations, dissociation of the lowest free-energy solvated quaternary complex CuG1$^{+\cdot}$ to [Cu(terpy)NO$_3$]$^{+\cdot}$ (aq) + G(aq) and [Cu^{II}(terpy)G]$^{2+\cdot}$ (aq) + NO$_3^-$ (aq) was endothermic, $\Delta G_{298,aq}$ = 25 and 34 kJ mol^{-1} , respectively, indicating micromolar formation constants in water and justifying our representation of the solution complexes shown in Scheme 1. We note that weak peaks of the quaternary complexes were present in the electrospray spectra.

After transfer to the gas phase and counterion separation, the ternary [Cu(terpy)G]$^{2+\cdot}$ complexes favored the structure with an N-3 and O-6 dicoordinated canonical guanine (G1Cu$^{2+\cdot}$, Figure 5). The second lowest-energy complex (G2Cu$^{2+\cdot}$) included the N-3-H, N-7-H guanine tautomer coordinated to Cu by O-6. The other complexes (G3Cu$^{2+\cdot}$ − G7Cu$^{2+\cdot}$), including that of the 6-OH enol form of guanine, were disfavored by ca. 40 kJ mol^{-1}.

Relative energies of gas-phase G$^{+\cdot}$ tautomers were calculated at several levels of theory and are displayed in Table 1. According to the calculations, the gas-phase canonical structure G1$^{+\cdot}$ with the 6-oxo, N-1-H, and N-9-H arrangement was the lowest-energy tautomer. Because this tautomer also formed low-energy solvated quaternary and gas-phase ternary complexes with Cu(terpy), we considered it the best candidate for the gas-phase ion formed in the ion trap. The *syn*- and *anti*-6- OH tautomers G2$^{+\cdot}$ and G3$^{+\cdot}$ were 3−9 kJ mol^{-1} less stable than G1$^{+\cdot}$ when based on the CCSD(T)/CBS energies. These tautomers did not form low-energy Cu complexes, and therefore, their potential presence in the gas phase could only be because of isomerization upon CID. The N-7-H tautomer (G4$^{+\cdot}$) was within 5.6 kJ mol^{-1} of G1$^{+\cdot}$ (Table 1) and formed a low-energy quaternary Cu complex in solution. Thus, G4$^{+\cdot}$ was considered a plausible candidate for the gas-phase ions. We note that the relative energies of G1$^{+\cdot}$ − G4$^{+\cdot}$ obtained from M06-2X calculations were in a very good agreement with the benchmark CCSD(T)/CBS data and thus appeared to be reliable for estimates of relative energies of larger ions where CCSD(T) calculations may not be feasible. Several other tautomeric combinations were investigated ($G5^{+\cdot}$ − $G8^{+\cdot}$) but were found to be much less stable than $G1^{+\cdot}$.

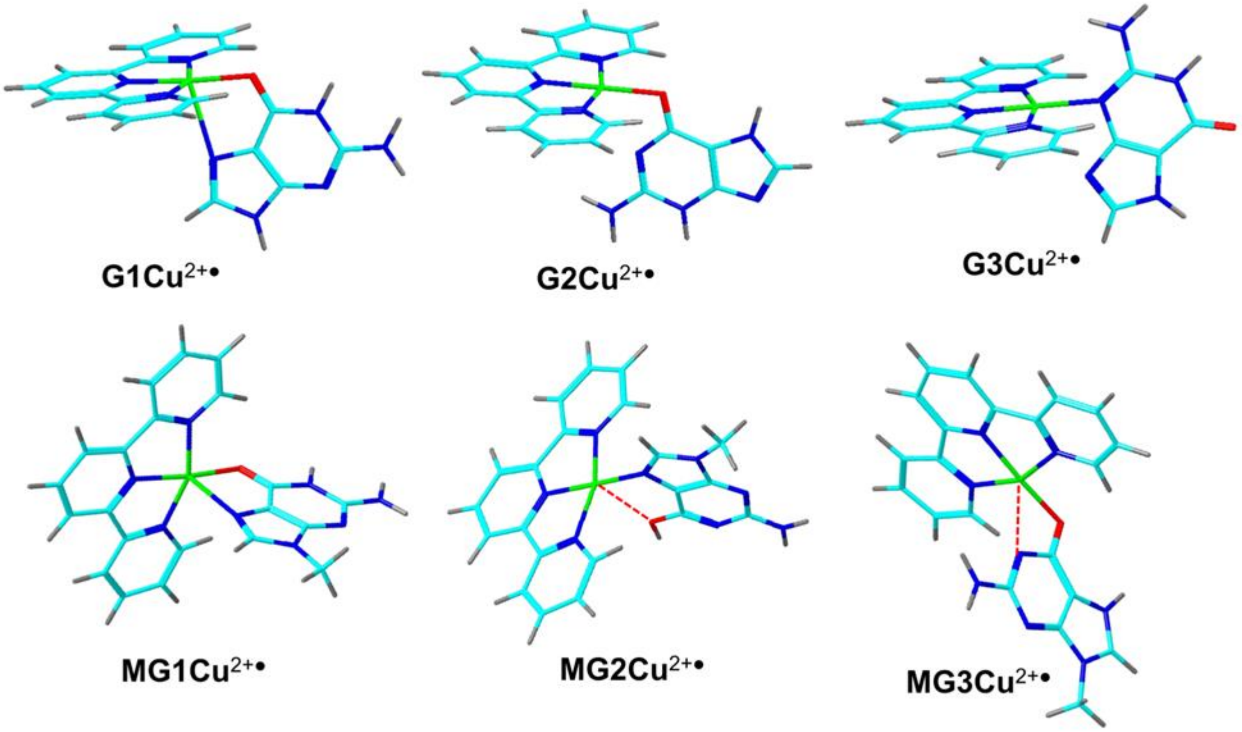

Figure 5. M06-2X/6-311+G(2d,p) optimized structures of low-energy gas-phase $[Cu(terpy)G]^{2+\cdot}$ and $[Cu(terpy)MG]^{2+\cdot}$ complexes. Atom color coding is as in Figure 4.

Table 2. Relative energies of $[9\text{-methylguanine}]^{+\cdot}$ isomers.

Ion or Reaction		Relative Energy[a,b]				
		M06-2X[c]	ωB97X-D[d]	PMP2[c]	CCSD(T)[c,e]	CCSD(T)[f]
		6-311++G(2d,p)		aug-cc-pVTZ		CBS
MeGuan1	**MG1**$^{+\cdot}$	0.0	0.0	0.0	0.0	0.0 (0.0)[g]
GuanO6-syn	**MG2**$^{+\cdot}$	–0.4	9.3	–3.9	–3.7	–2.2 (–1.0)

GuanO6-anti	**MG3**$^{+\cdot}$	5.5	17	–0.7	2.0	1.8 (3.0)
Guan7	**MG4**$^{+\cdot}$	66	9.0	7.2	6.2	5.6 (5.6)
Guan3	**MG5**$^{+\cdot}$	111	66	53	58	
Guan18	**MG6**$^{+\cdot}$	85	85	96		

[a]In kJ mol^{-1}. [b]Including B3LYP/6-31+G(d,p) zero-point energies and referring to 0 K unless stated otherwise. [c]Single-point energies on M06-2X/6-31+G(d,p) optimized geometries. [d]Single-point energies on ωB97X-D/6-31+G(d,p) optimized geometries. [e]Extrapolated single-point energies: E[CCSD(T)/aug-cc-pVTZ)] ≈ E[CCSD(T)/aug-cc-pVDZ)] + E[PMP2/aug-cc-pVTZ)] – E[PMP2/aug-cc-pVDZ)]. [f]Single point energies extrapolated to the complete basis set. [g]Relative free energies at 310 K.

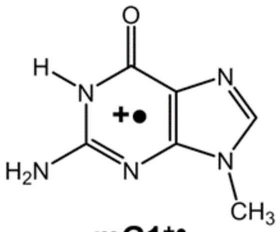

mG1$^{+\bullet}$

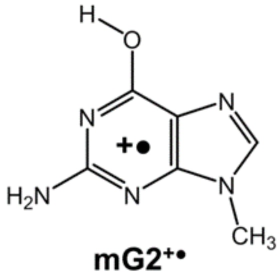

mG2$^{+\bullet}$

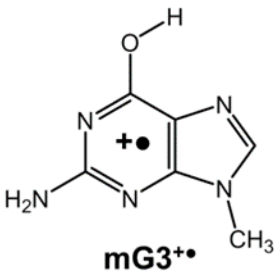

mG3$^{+\bullet}$

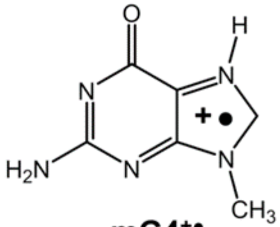

mG4$^{+\bullet}$

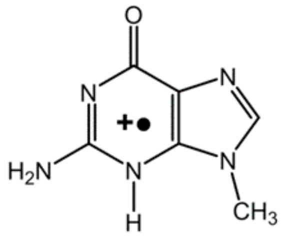

mG5$^{+\bullet}$

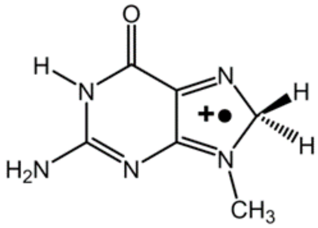

mG6$^{+\bullet}$

3.3.5 9-Methylguanine Structures and Energies

Aqueous quaternary complexes of MG with [Cu(terpy)NO$_3$]$^{+\cdot}$ showed preference for structure CuMG1$^{+\cdot}$ (Figure 4) in which MG was in the canonical 6-oxo, N-1-H form that was coordinated to Cu^{II} by the 6-oxo group. Complexes of the N-3- H (CuMG2$^{+\cdot}$), 6-OH (CuMG3$^{+\cdot}$), and N-7-H (CuMG4$^{+\cdot}$) tautomers were substantially less stable and were not expected to be present in solution at equilibrium. The gas-phase MG complexes also largely favored the canonical 6-oxo form MG1Cu$^{2+\cdot}$ in which MG was coordinated to Cu^{II} by O-6 and N-7 (Figure 5). MG1Cu$^{2+\cdot}$ can be formed from the lowest-energy quaternary complex CuMG1$^{+\cdot}$ by ion separation upon electrospray. Hence, coordination to Cu^{II}(terpy) in both solution and the gas-phase complexes favored the canonical MG tautomer over isomers.

The gas-phase $MG^{+\cdot}$ tautomers showed three structures of very similar energy (Table 2). The syn-6-OH tautomer $MG2^{+\cdot}$ was the lowest-energy structure, which was within 1 kJ mol^{-1} of the canonical 6-oxo tautomer $MG1^{+\cdot}$ according to CCSD(T)/CBS calculations. The anti-6-OH rotamer ($MG3^{+\cdot}$) was within 3−6 kJ mol^{-1} of $MG1^{+\cdot}$, whereas the 6-oxo-N-7-H tautomer ($MG4^{+\cdot}$) was 58 kJ mol^{-1} less stable (Table 2). We note that only $MG1^{+\cdot}$ can be formed without rearrangement from the low-energy Cu complexes $CuMG1^{+\cdot}$ and $MG1Cu^{2+\cdot}$ that were expected to dominate in solution and the gas phase. The other low-energy $MG^{+\cdot}$ tautomers can be produced only by CID-triggered proton transfer isomerizations.

Table 3. Relative energies of [guanosine]$^{+\cdot}$ isomers.

Ion or Reaction		Relative Energy[a,b]				
		M06-2X[c] 6-311++G(2d,p)	ωB97X-D[d] 6-311++G(2d,p)	PMP2[c] aug-cc-pVTZ	CCSD(T)[c,e] aug-cc-pVTZ	CCSD(T)[f] CBS
N-1-H	**rG1**$^{+\cdot}$	0.0	0.0	0.0	0.0	0.0 (0.0)[g]
O-6-syn	**rG2**$^{+\cdot}$	7.9	17	8.2	9.9	8.8 (9.8)
O-6-anti	**rG3**$^{+\cdot}$	12	21	15	14	13 (14)
N-7-H	**rG4**$^{+\cdot}$	53	50			
N-3-H	**rG5**$^{+\cdot}$	76	73			
TS		138	133	138	132	131
Complex	**rG6**$^{+\cdot}$	132	129	134	130	126
Complex2	**rG7**$^{+\cdot}$	38	35	35	33	31 (23)
G1$^{+\cdot}$ + $C_5H_8O_4$		103	103	111	105	96 (48)

[a] In kJ mol^{-1}. [b] Including B3LYP/6-31+G(d,p) zero-point energies and referring to 0 K unless stated otherwise. [c] Single-point energies on M06-2X/6-31+G(d,p) optimized geometries. [d] Single-point energies

on ωB97X-D/6-31+G(d,p) optimized geometries. [e]Extrapolated single-point energies: E[CCSD(T)/aug-cc-pVTZ)] ≈ E[CCSD(T)/aug-cc-pVDZ)] + E[PMP2/aug-cc-pVTZ)] – E[PMP2/aug-cc-pVDZ)]. [f]Single point energies extrapolated to the complete basis set. [g]Relative free energies at 310 K.

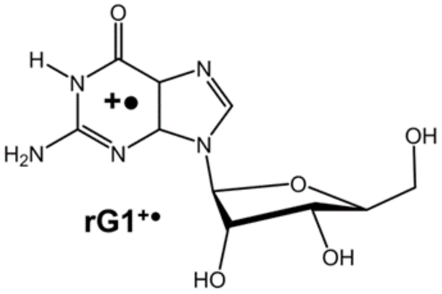

rG1$^{+\bullet}$

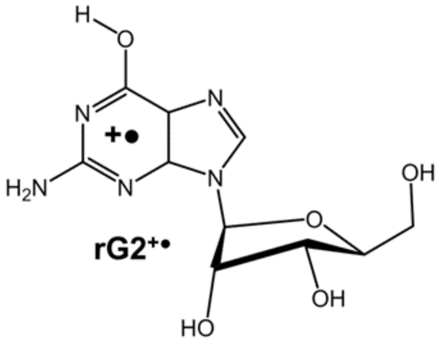

rG2$^{+\bullet}$

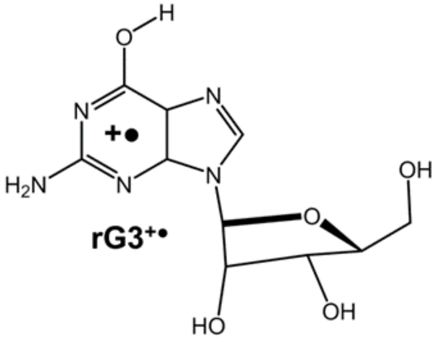

rG3$^{+\bullet}$

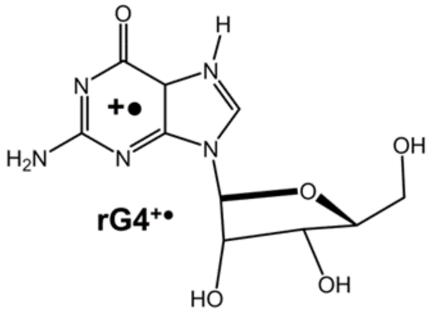

rG4$^{+\bullet}$

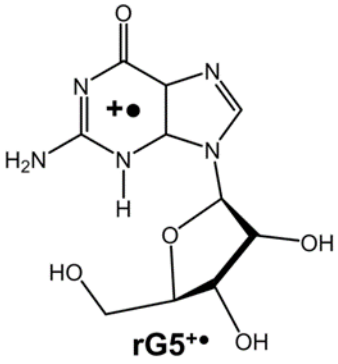

rG5$^{+\bullet}$

3.3.6 Guanosine Structures and Energies

Similar to $G^{+\cdot}$, the guanosine cation radicals favored the canonical tautomer rG1$^{+\cdot}$ as the lowest-energy structure. The *syn*- and *anti*-6-OH enol forms (rG2$^{+\cdot}$ and rG3$^{+\cdot}$, respectively) had higher relative energies at all levels of theory that we investigated. Further, 6-oxo tautomers with the N-7-H (rG4$^{+\cdot}$) and N-3-H (rG5$^{+\cdot}$) arrangements had substantially higher relative energies (Table 3). We found a similar ranking of relative energies for the four lowest-energy tautomers of [deoxyguanosine]$^{+\cdot}$ (dG1$^{+\cdot}$ − dG5$^{+\cdot}$) that were analyzed at the same level of theory for comparison.

We investigated the dissociation energy of rG1$^{+\cdot}$ that was of interest with regard to the CID and UVPD spectra that indicated facile loss of the ribose moiety. G1$^{+\cdot}$ -forming dissociation was found to essentially follow the route elucidated by O’Hair et al. for [deoxyguanosine]$^{+\cdot}$.[38] This consisted of cleavage of the N-9-C-1′ bond to reach a complex of the guanyl radical with the ribose cation (rG6$^{+\cdot}$). In contrast to O’Hair et al., we found the electron distribution in the intermediate complex of guanosine to involve a ribose C-1′ cation and a guanine radical. This was obvious from the analysis of spin densities that pointed to ∼100% of unpaired electron density to be in the guanine ring (Scheme 2). Also, the planar geometry at the ribose C-1′ in rG6$^{+\cdot}$ was highly indicative of a carbocation. The further reaction course involved a transition state (TS(rG)$^{+\cdot}$) undergoing simultaneous closure of the 1,5′-anhydroribose ring and proton transfer onto N-9 and forming a low-energy complex (rG7$^{+\cdot}$, Scheme 2). In accord with the previous analysis of O’Hair et al., TS(rG)$^{+\cdot}$ at 131 kJ mol^{-1} relative to rG1$^{+\cdot}$ was also the highest energy point on the potential energy surface for rG1$^{+\cdot}$ dissociation.[38] The threshold energy for the separation of G1$^{+\cdot}$ and 1,5-anhydroribose was calculated to be 96 kJ mol^{-1} relative to rG1$^{+\cdot}$ at the CCSD(T)/CBS level of theory, and this final step of dissociation in rG7$^{+\cdot}$ was presumed to be continuously endothermic. Compared to the CCSD(T)/CBS energetics of the analogous dissociation of [deoxyguanosine]$^{+\cdot}$, the dissociation of rG1$^{+\cdot}$ required a slightly higher energy transition state and intermediates. This was consistent with the formation of a ribose C-1′ cation in rG6$^{+\cdot}$ and TS(rG$^{+\cdot}$), which was destabilized in the presence of the electron-withdrawing 2′-OH group. Interestingly, attempts at exploring participation by the 2′-OH group in the cleavage of the

C-1′- N-9 bond in rG1$^{+\cdot}$ did not result in the formation of stable intermediates as the system collapsed to rG6$^{+\cdot}$ upon gradient geometry optimization.

With regard to the photodissociation experiments, we used the TS(rG$^{+\cdot}$) energy to calculate the unimolecular rate constants for dissociation of rG1$^{+\cdot}$ when driven by the absorbed photon energy. The results indicated that absorption of a single photon of λ < 650 nm can trigger dissociation on the 50 ms experimental time scale. Furthermore, the rG1$^{+\cdot}$ lifetime dropped to a few ns at excitation energies achieved by absorption of photons of λ < 250 nm. This indicated that rG1$^{+\cdot}$ can dissociate within a 3−6 ns laser pulse, and the resulting [guanosine] $^{+\cdot}$ can absorb another photon from the same pulse to drive its consecutive dissociation.

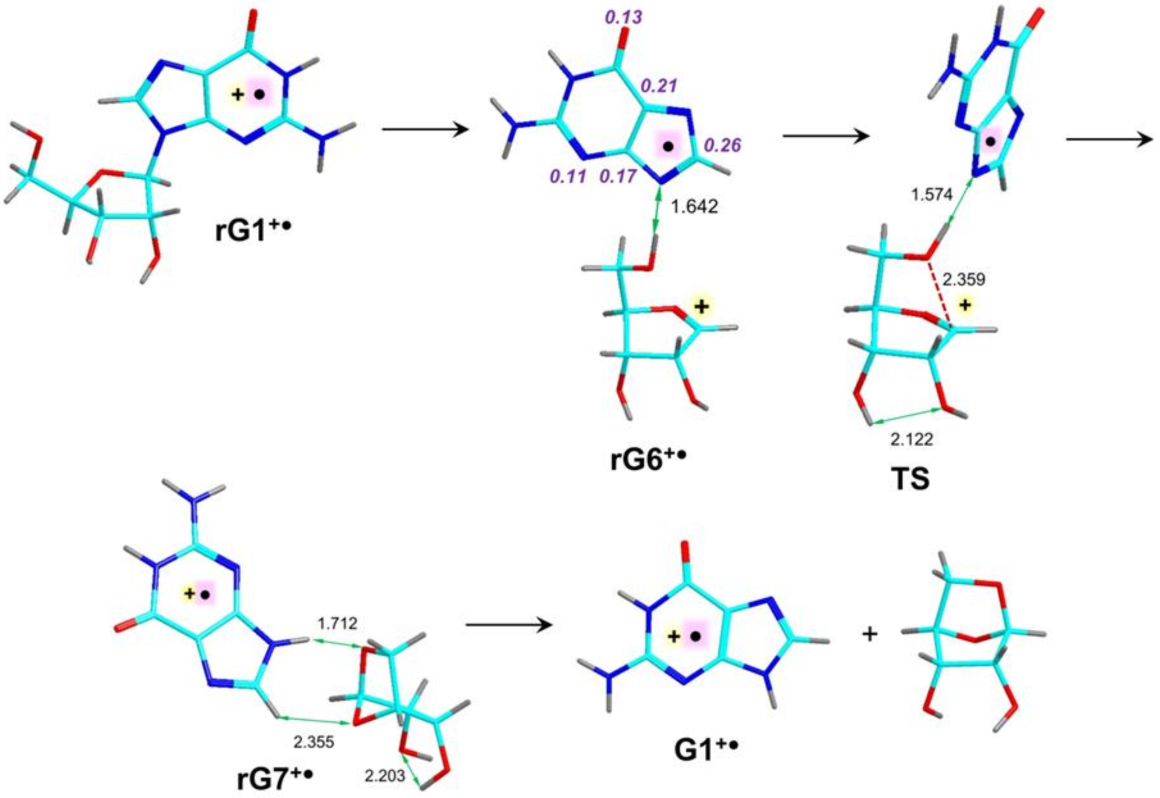

Scheme 2. Intermediates and transition state for dissociations of [guanosine]$^{+\cdot}$ isomer rG1$^{+\cdot}$ (italics show the calculated atomic spin densities in rG6$^{+\cdot}$).

3.3.7 Excited Electronic States and Comparison of Theoretical Absorption and Experimental Action Spectra

To interpret the UV−vis action spectra, we carried out calculations of excited-state energies and oscillator strengths for multiple tautomers of $G^{+\cdot}$, $MG^{+\cdot}$, and $rG^{+\cdot}$ that allowed us to obtain theoretical absorption spectra. The calculations were augmented by including excitations from multiple Boltzmann-populated vibrational states to produce vibronic absorption spectra at 310 K. The excited-state calculations were carried out with TD-DFT M06-2X that was benchmarked to EOMCCSD with the 6-31+G(d,p) basis set.

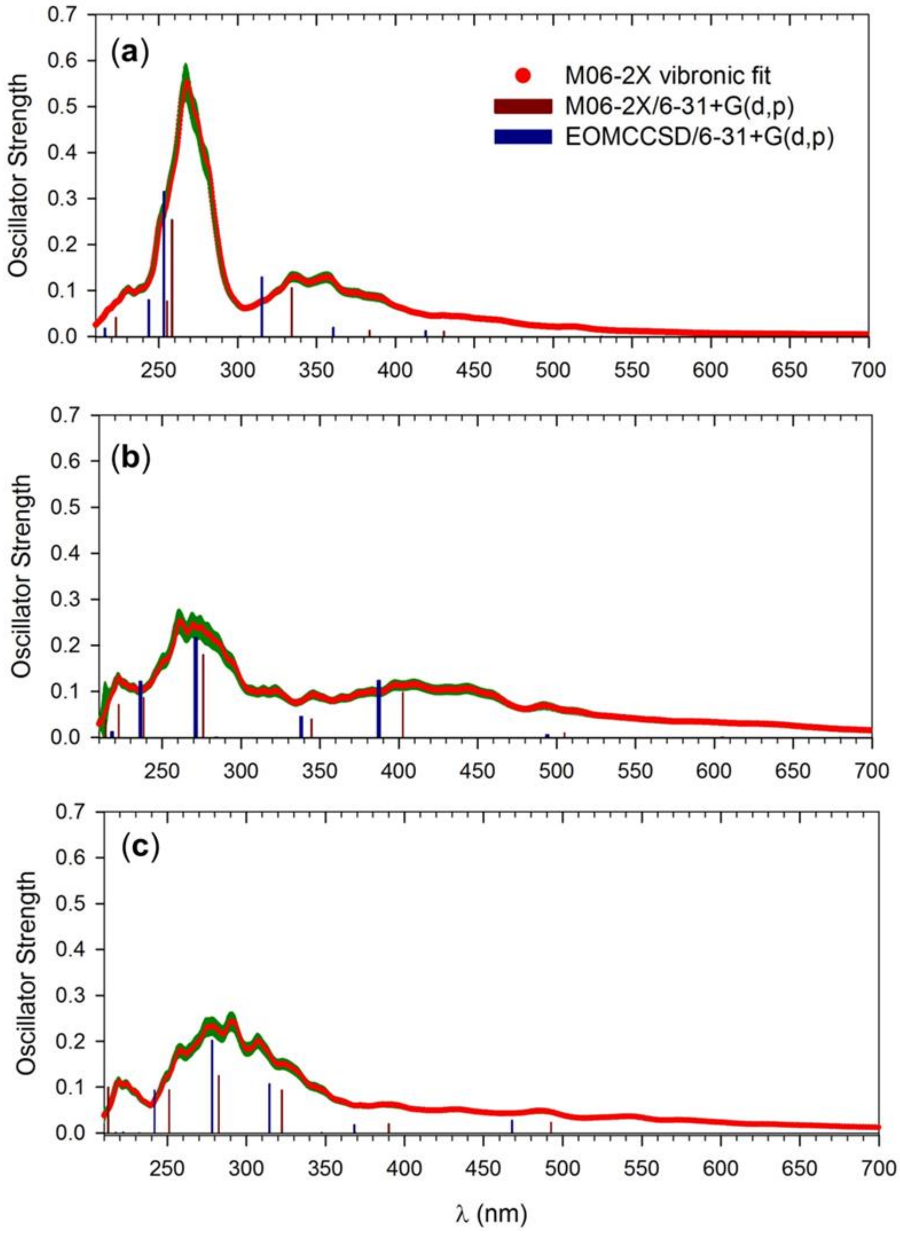

Figure 6. M06-2X/6-31+G(d,p) TD-DFT line, vibronic, and EOM-CCSD line spectra fits for (a) $G1^{+\cdot}$, (b) $G2^{+\cdot}$, and (c) $G4^{+\cdot}$. Green vertical lines indicate error bars in the vibronic spectra calculations.

3.3.8 Guanine Cation Radicals

Starting with $G1^{+\cdot}$, the calculated absorption spectrum (Figure 6a) showed six major lines that were broadened to overlapping bands with maxima at 230, 270, 340, 360, and 440 nm and extended as a weak broad shoulder to 530 nm. Another very weak line appeared at 610 nm. The excitation lines from the benchmarking EOM-CCSD calculations (blue lines in Figure 6a) were generally blue-shifted relative to those from TD-DFT M06-2X, but both sets showed correlating wavelengths and oscillator strengths. We note that a previous benchmarking study of radical excitations66 found that increasing the basis set in EOM-CCSD calculations resulted in 0.1−0.2 eV red shifts of the excitation energies. Thus, through error cancellation, the current TD-DFT M06-2X calculations were expected to achieve a reasonably accurate description of electronic excitations in the nucleobase radicals. The calculated absorption spectra of the *syn*- and *anti*-OH rotamers $G2^{+\cdot}$ and $G3^{+\cdot}$ were very similar and are here represented by the calculated excitation lines and vibronic spectrum of $G2^{+\cdot}$ (Figure 6b). The TD-DFT lines appeared at 214, 222, 238, 276, 345, 403, and 505 nm that were broadened into bands with maxima at 223, 262, 275, 345, 400, and 495 nm in the vibronic spectrum. The EOM-CCSD excitation lines showed a close correlation and a blue shift relative to the M06-2X ones. A different absorption spectrum was calculated for $G4^{+\cdot}$ (Figure 6c), which showed major TD-DFT lines at 213, 251, 282, 322, 390, and 493 nm, in close correlation with EOM-CCSD. Vibronic broadening resulted in bands with maxima at 220, 280, 390, and 490 nm for $G4^{+\cdot}$.

When comparing the calculated vibronic spectra of $G1^{+\cdot}$ − $G4^{+\cdot}$ with the action spectrum (Figure 1), we found the closest match for $G1^{+\cdot}$ (Figure 6a). The match was based on (1) the low intensity in the action spectrum of the 230 nm band, (2) the shape and position of the main band at 290 nm, and (3) the composite band at 340−380 nm. The 420−550 nm tail in the action spectrum also had a matching feature in the vibronic spectrum of $G1^{+\cdot}$ (Figure 6a), although this region was also represented in the vibronic spectra of $G2^{+\cdot}$ and $G4^{+\cdot}$. We note that small (estimated <5%) fractions of $G2^{+\cdot}$ and $G4^{+\cdot}$ could not be excluded on the basis of the spectra alone. However, attempts at fitting the action spectrum by a Boltzmann-weighed mixture of vibronic spectra of $G1^{+\cdot} - G4^{+\cdot}$, when based on the CCSD(T)/CBS free energies (Table 1), resulted in a poor match. Hence, we conclude that the canonical guanine cation radical structure $G1^{+\cdot}$ was represented in the gas phase, originating from the most stable quaternary Cu(terpy)NO_3 complex in solution via a ternary Cu(terpy) complex produced by electrospray. The formation of $G1^{+\cdot}$ from the guanosine complex, as evidenced by the matching action spectrum, was consistent with the proposed dissociation mechanism.

The electronic excitations in $G1^{+\cdot}$ for several excited states are illustrated with the relevant molecular orbitals in Figure 7. The first (A) excited state of ΔE_{exc} = 2.03 eV corresponded to a dipole-disallowed transition from the highest π_{xy} orbital (MO38) to the singly occupied molecular orbital (MO39, SOMO), which was of π_z type. MO38 was a combination of n-type orbitals at N-3, N-7, and O-6. This transition had a very low oscillator strength (0.0002) and appeared in neither the calculated absorption nor the action spectrum. The second (B) excited state, corresponding to the transition π_{xy}(MO36) → SOMO of ΔE_{exc} = 2.55 eV, was likewise dipole-forbidden and was not observed. The longest-wavelength band that appeared in the spectrum was due to the C excited state, arising from the dipole-allowed π_z(MO35) → SOMO excitation of ΔE_{exc} = 2.88 eV. Further dipole-allowed excitations to the SOMO accounted for the D (π_z(MO37), ΔE_{exc} = 3.23 eV) and E states (π_z(MO34), ΔE_{exc} = 3.71 eV). The most intense transition at 258 nm of ΔE_{exc} = 4.80 eV involved electron excitation from the SOMO to the virtual orbital space, chiefly involving the π_z(MO40) and π_z(MO41) orbitals (Figure 7).

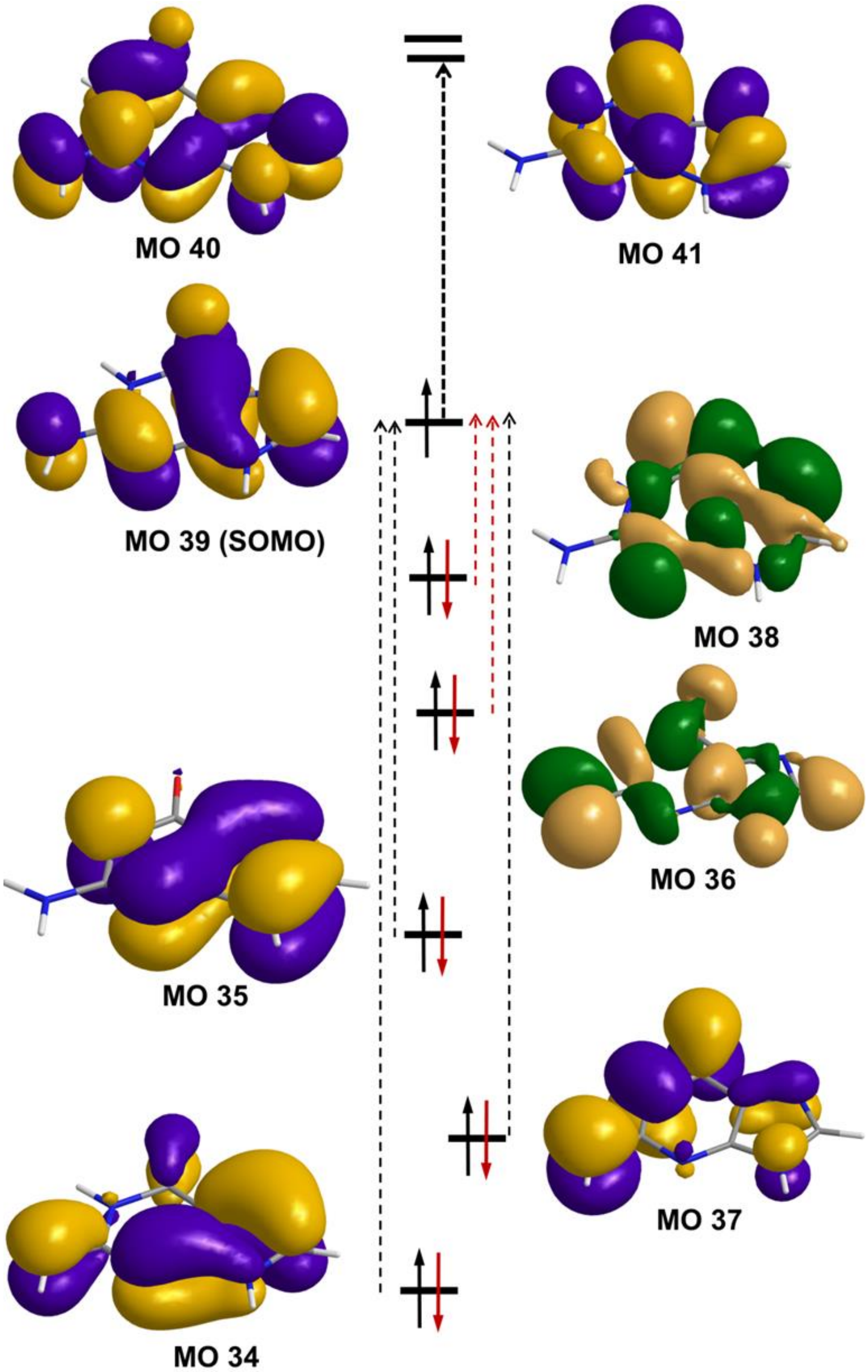

Figure 7. Molecular orbitals of ground and excited electronic states in G1$^{+\cdot}$ from M06-2X/6-31+G(d,p) calculations. Black broken-line arrows indicate dipole-allowed electronic excitations, and red arrows are for dipole-disallowed ones.

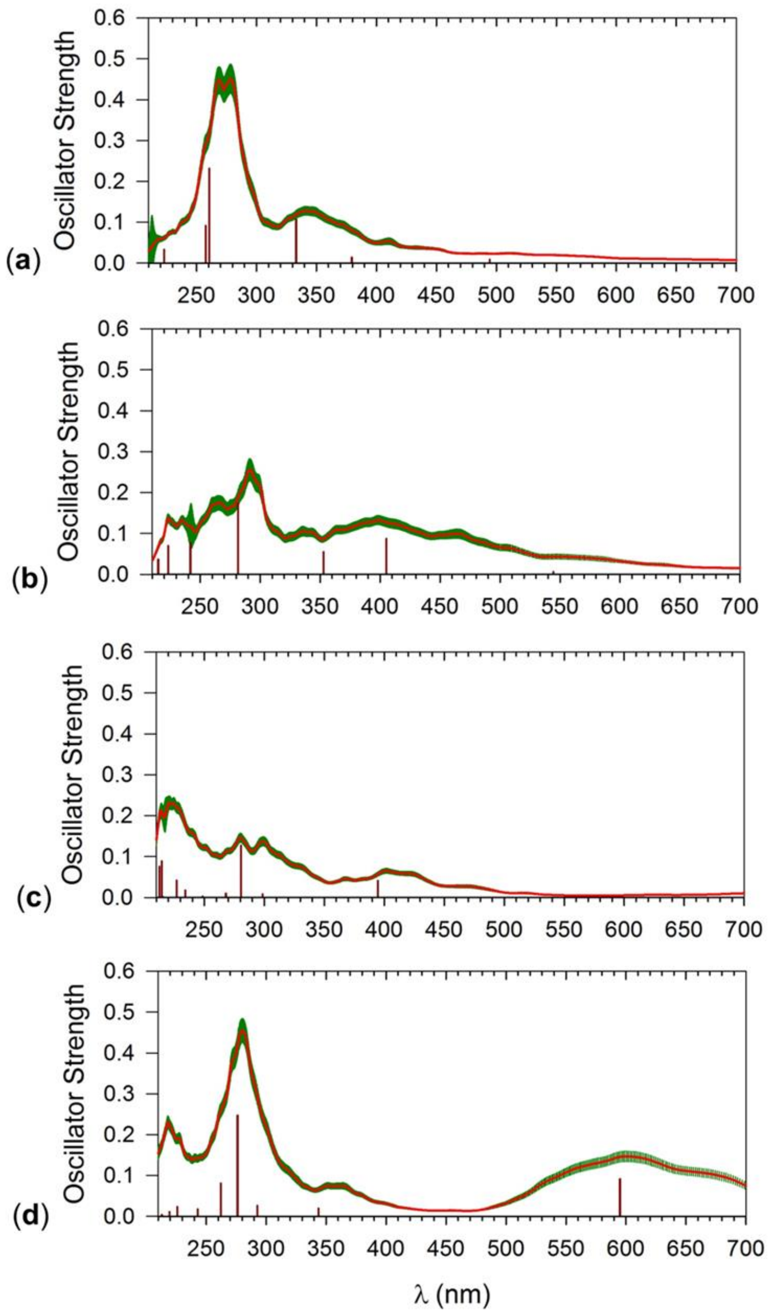

Figure 8. M06-2X/6-31+G(d,p) TD-DFT line, vibronic, and EOM-CCSD line spectra fits for (a) MG1$^{+\cdot}$, (b) MG2$^{+\cdot}$, (c) MG3$^{+\cdot}$, and (d) MG6$^{+\cdot}$. Green vertical lines indicate error bars in the vibronic spectra calculations.

3.3.9 Methylguanine Cation Radicals

The calculated absorption spectra of 9-methyl guanine tautomers displayed different bands (Figure 8a–d) to be compared with the action spectrum (Figure 2). The canonical isomer MG1$^{+\cdot}$ had five major excitation lines at 223, 258, 261, 333, and 379 and a very weak line at 494 nm that gave rise to vibronically broadened bands in the spectrum (Figure 8a). The absorption spectrum of MG1$^{+\cdot}$ showed an excellent match with the action spectrum of [9-methylguanine]$^{+\cdot}$ (Figure 2). In contrast, the absorption spectra of low-energy tautomers MG2$^{+\cdot}$ and MG3$^{+\cdot}$ (Figure 8b,c) were distinctly different in that they had different patterns of dominant bands at 220–230 and 400 nm that were much less evident in the action spectrum. A less stable isomer (MG6$^{+\cdot}$, Figure 8d) had an intense band at 276 nm that was analogous to the 290 nm band in the action spectrum. However, MG6$^{+\cdot}$ further displayed a composite band at 220 nm and a broad band at 595 nm that were not pronouncedly represented in the action spectrum. Our assignment of the action spectrum belonging to the canonical isomer MG1$^{+\cdot}$ is in perfect agreement with the previous conclusion by O'Hair and co-workers that they made on the basis of an infrared action spectrum.[37] The electronic excitations in MG1$^{+\cdot}$ occurred on a manifold of excited states that closely resembled that for G1$^{+\cdot}$. It is worth noting that MG1$^{+\cdot}$ is not the lowest free-energy isomer among the [9-methylguanine] $^{+\cdot}$ ions (Table 2). However, the canonical structure was highly energetically preferred in the ion precursors that were the Cu^{II}(terpy) complexes in solution and the gas phase. Under equilibrium conditions in solution, the calculated relative free energies suggested CuMG1$^{+\cdot}$ to represent >99% of the isomer population. Hence, the dominant formation of MG1$^{+\cdot}$ in the gas-phase ion population can be explained by selection of the canonical MG1 tautomer when binding in the Cu^{II} complex. At the same time, the absence of low-energy isomers MG2$^{+\cdot}$ and MG3$^{+\cdot}$ among the gas-phase ion population indicated that the

Cu^{II}-coordinated nucleobase ligand did not undergo proton transfer isomerization in the course of electron transfer oxidation upon CID.

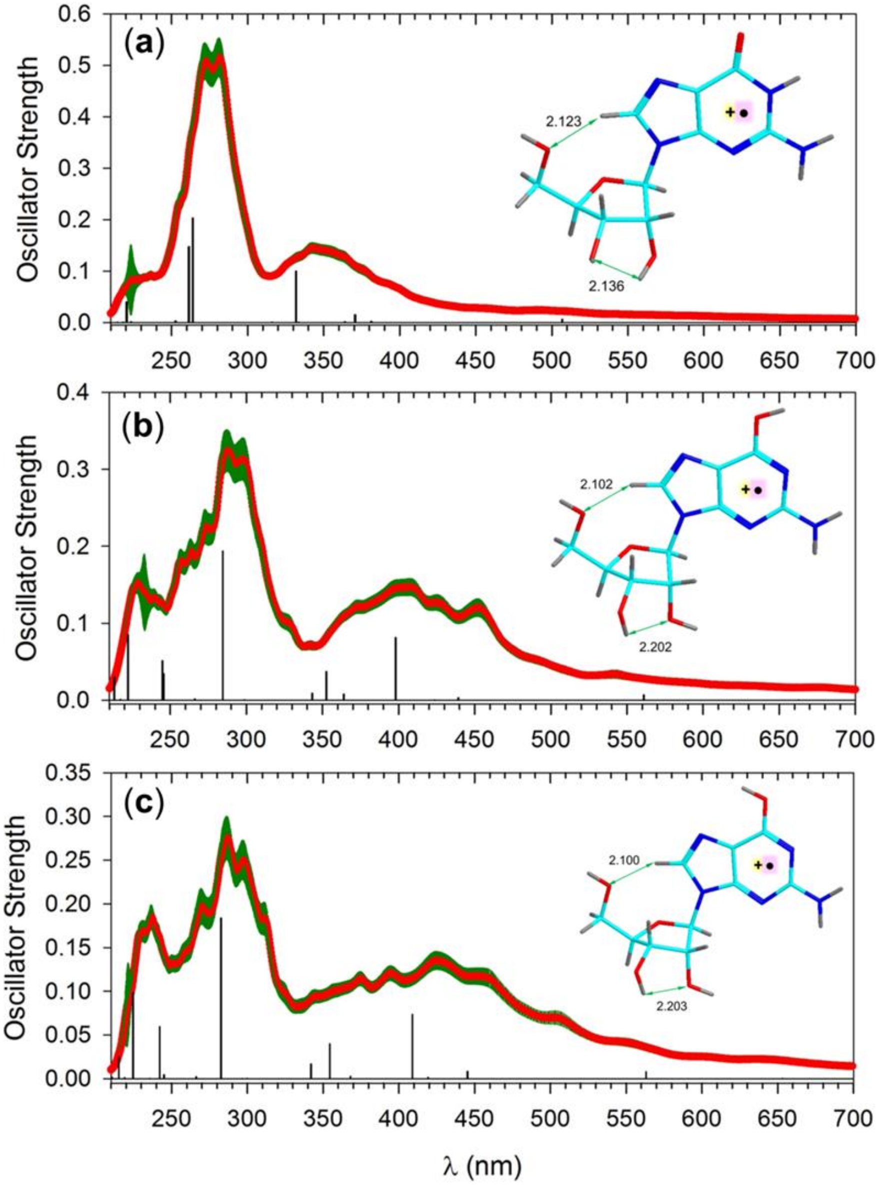

Figure 9. M06-2X/6-31+G(d,p) TD-DFT line and vibronic spectra fits for (a) rG1$^{+\cdot}$, (b) rG2$^{+\cdot}$, and (c) rG3$^{+\cdot}$.

3.3.10 Guanosine Cation Radicals

The calculated absorption spectra of guanosine tautomers differed in displaying several distinct bands (Figure 9a−c). The canonical isomer $rG1^{+\cdot}$ had two prominent absorptions at 261 and 264 nm that were accompanied by weaker lines at 221, 332, 371, and 507 nm (Figure 9a). The *syn*- and *anti*-6-OH isomers showed stronger lines at 222 and 245 nm and prominent lines at 282−284 nm. Further distinction was indicated by four lines in the 340−450 nm region and weak lines at 560−563 nm (Figure 9b,c). In addition, the vibronic spectra showed distinctly different transitions from higher vibrational states, which is particularly illustrated by broad bands with maxima at 400−420 nm for $rG2^{+\cdot}$ and $rG3^{+\cdot}$. This broad band was not represented in the action spectrum of [guanosine] $^{+\cdot}$ (Figure 3), indicating that $rG2^{+\cdot}$ and $rG3^{+\cdot}$ were not substantially populated among the gas-phase ions. The absorption spectrum of $rG1^{+\cdot}$ provided matching wavelengths for the band maxima with those in the action spectrum. However, the band relative intensities differed. In particular, the band group at 250 and 290 nm was weaker than the 370 nm band in the action spectrum, contrasting the corresponding band intensities in the calculated vibronic spectrum. We propose an explanation of this discrepancy on the basis of the kinetics for the main photodissociation channel, which was loss of 1,5-anhydroribose (Scheme 2). The dissociation can be accomplished at the 50 ms time scale by single-photon absorption at wavelengths of up to ca. 650 nm. At photon wavelengths below ca. 300 nm, the excited ion lifetime dropped below 5 ns, producing vibrationally excited products. On the basis of energy balance, the excitation energy was estimated to be $E_{exc} = E(h\nu) - E(diss) = 400-96 = 304$ kJ mol^{-1} at 300 nm that was partitioned between the $G1^{+\cdot}$ and 1,5-anhydroribose products. Assuming that the excess energy was partitioned according to the fragments’ heat capacities at the equivalent temperature of 940 K,[76] the $G1^{+\cdot}$ ion received an energy of 163 kJ mol^{-1} from photodissociation at 300 nm. Note that this internal excitation would be insufficient to drive the dissociation of G1$^{+\cdot}$ that had a calculated energy threshold at 271 kJ mol^{-1} (Table 1). However, because of the extremely fast photofragmentation, the nascent G1$^{+\cdot}$ ion can absorb a photon from the same laser pulse and undergo consecutive dissociation. The nearly matching bands at 220 and 280−290 nm in the action spectra of rG1$^{+\cdot}$ and G1$^{+\cdot}$ would allow absorption of consecutive photons. The dissociation of G1$^{+\cdot}$ depleted the primary photofragment ion intensity and resulted in reduced intensity of the short-wavelength bands in the action spectrum of rG1$^{+\cdot}$. Note that the photodissociation of rG1$^{+\cdot}$ on the laser pulse 5 ns time scale rapidly dropped at $\lambda > 350$ nm, indicating that the main 370 nm band in the action spectrum should not be affected. On the basis of this analysis, we assign the action spectrum of [guanosine]$^{+\cdot}$ to the lowest-energy isomer rG1$^{+\cdot}$. We note that our assignment for [guanosine]$^{+\cdot}$ is consistent with the conclusion of O'Hair et al. for [2′-deoxyguanosine]$^{+\cdot}$ that was made on the basis of infrared action spectra.[38] The electron transitions leading to excited states in rG1$^{+\cdot}$ were analogous to those in MG1$^{+\cdot}$. The ribose moiety was not involved in the dominant excitations that involved the $\pi_z \rightarrow$ SOMO(MO74) and SOMO $\rightarrow \pi_z^*$ type transitions forming excited states H (λ_{max} = 332 nm), K (λ_{max} = 264 nm), L (λ_{max} = 261 nm), and O (λ_{max} = 221 nm). Charge transfer transitions involving ribose ionization were apparent in excited states E (λ_{max} = 371 nm) and M (λ_{max} = 253 nm).

3.4 Conclusions

Action spectroscopy in the gas phase allowed us to obtain mass-resolved UV−vis spectra of canonical forms of guanine, 9-methylguanine, and guanosine cation radicals that were free of interferences from proton transfer and radical reaction products. The spectra showed common bands at 350−400 nm that were assigned to internal $\pi_z \rightarrow$ SOMO electron excitations within the β-orbital manifold and were found to be characteristic of the open-shell electronic system. The two lowest excited states of guanine, 9-methylguanine, and guanosine cation radicals were calculated to be dark states of near-zero oscillator strength in the visible region of the spectrum. The UV−vis spectra of the canonical cation radical isomers were distinctly different from those calculated for tautomers and can be used for isomer identification. The common band features found in the action spectra may represent benchmarks for the identification of transient guanine cation radicals produced by DNA ionization.

3.5 Acknowledgments

Financial support from the Chemistry Division of the National Science Foundation (Grants CHE-1661815 for experiments and CHE-1624430 for calculations) is gratefully acknowledged. F.T. acknowledges the Klaus and Mary Ann Saegebarth Endowment for general support.

3.6 References

1. Khanna, K. K.; Jackson, S. P. DNA Double-Strand Breaks: Signaling, Repair and the Cancer Connection. *Nat. Genet*. 2001, 27, 247−254.
2. Hush, N. S.; Cheung, A. S. Ionization Potentials and Donor Properties of Nucleic Acid Bases and Related Compounds. *Chem. Phys. Lett*. 1975, 34, 11−13.
3. Sugiyama, H.; Saito, I. Theoretical Studies of GG-Specific Photocleavage of DNA via Electron Transfer: Significant Lowering of Ionization Potential and 5′-Localization of HOMO of Stacked GG Bases in B-Form DNA. *J. Am. Chem. Soc*. 1996, 118, 7063−7068.

4. Jovanovic, S. V.; Simic, M. G. One-Electron Redox Potentials of Purines and Pyrimidines. *J. Phys. Chem*. 1986, 90, 974−978.
5. Psciuk, B. T.; Lord, R. L.; Munk, B. H.; Schlegel, H. B. Theoretical Determination of One-Electron Oxidation Potentials for Nucleic Acid Bases. *J. Chem. Theory Comput*. 2012, 8, 5107−5123.
6. Langmaier, J.; Samec, Z.; Samcova, E.; Hobza, P.; Reha, D. Origin of Difference between One-Electron Redox Potentials of Guanosine and Guanine: Electrochemical and Quantum Chemical Study. *J. Phys. Chem. B.* 2004, 108, 15896−15899.
7. Bi, S.; Liu, B.; Fan, F.-R. F.; Bard, A. J. Electrochemical Studies of Guanosine in DMF and Detection of Its Radical Cation in a Scanning Electrochemical Microscopy Nanogap Experiment. *J. Am. Chem. Soc*. 2005, 127, 3690−3691.
8. Crespo-Hernandez, C. E.; Close, D. M.; Gorb, L.; Leszczynski, J. Determination of Redox Potentials for the Watson-Crick Base Pairs, DNA Nucleosides, and Relevant Nucleoside Analogs. *J. Phys. Chem. B.* 2007, 111, 5386−5395.
9. O'Neill, M. A.; Barton, J. K. Sequence-Dependent DNA Dynamics: The Regulator of DNA-mediated Charge Transport. In Charge Transfer in DNA: From Mechanism to Application; Wagenknecht, H.-A., Ed.; Wiley-VCH: Weinheim, 2005; pp 27−77.
10. Kim, H.; Budzinski, E. E.; Box, H. C. The Radiation-Induced Oxidation and Reduction of Guanine: Electron Spin ResonanceElectron Nuclear Double Resonance Studies of Irradiated Guanosine Cyclic Monophosphate. *J. Chem. Phys*. 1989, 90, 1448−1451.
11. Meggers, E.; Dussy, A.; Schafer, T.; Giese, B. Electron Transfer in DNA from Guanine and 8-Oxoguanine to a Radical Cation of the Carbohydrate Backbone. *Chem. - Eur. J*. 2000, 6, 485−492.

12. Shukla, L. I.; Pazdro, R.; Huang, J.; DeVreugd, C.; Becker, D.; Sevilla, M. D. The Formation of DNA Sugar Radicals from Photoexcitation of Guanine Cation Radicals. *Radiat. Res*. 2004, 161, 582−590.
13. Onyemauwa, F. O.; Schuster, G. B. The Reaction of Water with Guanosine Radical Cation in DNA. *Photochem. Photobiol*. 2006, 82, 729−732.
14. Khanduri, D.; Collins, S.; Kumar, A.; Adhikary, A.; Sevilla, M. D. Formation of Sugar Radicals in RNA Model Systems and Oligomers via Excitation of Guanine Cation Radical. *J. Phys. Chem. B*. 2008, 112, 2168−2178.
15. Shafirovich, V.; Geacintov, N. E. Spectroscopic Investigation of Charge Transfer in DNA. In Charge Transfer in DNA: From Mechanism to Application; Wagenknecht, H.-A., Ed.; Wiley-VCH: Weinheim, 2005; pp 175−196.
16. Steenken, S.; Jovanovic, S. V. How Easily Oxidizable Is DNA? One-Electron Reduction Potentials of Adenosine and Guanosine Radicals in Aqueous Solution. *J. Am. Chem. Soc.* 1997, 119, 617−618.
17. Bachler, V.; Hildenbrand, K. EPR-Detection of the Guanosyl Radical Cation in Aqueous Solution. Quantum Chemically Supported Assignment of Nitrogen and Proton Hyperfine Couplings. *Radiat. Phys. Chem*. 1992, 40, 59−68.
18. Kobayashi, K.; Tagawa, S. Direct Observation of Guanine Radical Cation Deprotonation in Duplex DNA Using Pulse Radiolysis. *J. Am. Chem. Soc*. 2003, 125, 10213−10218.
19. Morozova, O. B.; Saprygina, N. N.; Fedorova, O. S.; Yurkovskaya, A. V. Deprotonation of Transient Guanosyl Cation Radical Catalyzed by Buffer in Aqueous Solution: TR-CIDNP Study. *Appl. Magn. Reson*. 2011, 41, 239−250.

20. Morozova, O. B.; Fishman, N. N.; Yurkovskaya, A. V. Indirect NMR Detection of Transient Guanosyl Radical Protonation in Neutral Aqueous Solution. *Phys. Chem. Chem. Phys*. 2017, 19, 21262− 21266.

21. Choi, J.; Yang, C.; Fujitsuka, M.; Tojo, S.; Ihee, H.; Majima, T. Proton Transfer of Guanine Radical Cations Studied by Time Resolved Resonance Raman Spectroscopy Combined with Pulse Radiolysis. *J. Phys. Chem. Lett*. 2015, 6, 5045−5050.

22. Wolken, J. K.; Syrstad, E. A.; Vivekananda, S.; Turecek, F. ˇ Uracil Radicals in the Gas Phase. Specific Generation and Energetics. *J. Am. Chem. Soc*. 2001, 123, 5804−5805.

23. Syrstad, E. A.; Vivekananda, S.; Turecek, F. Direct Observation ˇ of a Hydrogen Atom Adduct to C-5 in Uracil. A Neutralization Reionization Mass Spectrometric and ab initio Study. *J. Phys. Chem. A*. 2001, 105, 8339−8351.

24. Yao, C.; Cuadrado-Peinado, M.; Polaśek, M.; Turec ˇ ek, F. ˇ Specific Generation of 1-Methylcytosine Radicals in the Gas-Phase. *Angew. Chem*., Int. Ed. 2005, 44, 6708−6711.

25. Chu, I. K.; Rodriquez, C. F.; Lau, T.-C.; Hopkinson, A. C.; Siu, K. W. M. Molecular Radical Cations of Oligopeptides. *J. Phys. Chem. B*. 2000, 104, 3393−3397.

26. Wee, S.; O'Hair, R. A. J.; McFadyen, W. D. Can Radical Cations of the Constituents of Nucleic Acids Be Formed in the Gas Phase Using Ternary Transition Metal Complexes? *Rapid Commun. Mass Spectrom*. 2005, 19, 1797−1805.

27. Cheng, P.; Bohme, D. K. Gas-Phase Formation of Radical Cations of Monomers and Dimers of Guanosine by Collision-Induced Dissociation of Cu(II)-Guanosine Complexes. *J. Phys. Chem. B*. 2007, 111, 11075−11082.

28. Zhang, S.; Xu, L.; Dong, J.; Cheng, P.; Zhou, Z.; Fu, J. Collision-Induced Dissociation of Singly and Doubly Charged Cu^{II}Cytidine Complexes in the Gas Phase: An Experimental and Computational Study. *RSC Adv*. 2012, 2, 2568−2575.
29. Gatlin, C. L.; Turecek, F.; Vaisar, T. Copper(II) Amino Acidˇ Complexes in the Gas Phase. *J. Am. Chem. Soc*. 1995, 117, 3637− 3638.
30. Turecek, F. Copper-Biomolecule Complexes in the Gas Phase.ˇThe Ternary Way. *Mass Spectrom. Rev*. 2007, 26, 563−582.
31. Sun, Y.; Zhou, W.; Moe, M. M.; Liu, J. Reactions of Water with Radical Cations of Guanine, 9-Methylguanine, 2'-Deoxyguanosine and Guanosine: Keto-Enol Isomerization, C8-Hydroxylation, and Effects of N9-Substitution. *Phys. Chem. Chem. Phys*. 2018, 20, 27510− 27522.
32. Liguori, A.; Napoli, A.; Sindona, G. Electron Transfer vs. Proton Transfer within Radical-Cation Clusters of Guanosine and Deoxyguanosine with Substituted Naphthalenes and Sinapinic Acid. *J. Am. Soc. Mass Spectrom*. 2001, 12, 176−179.
33. Feketeova, L.; Yuriev, E.; Orbell, J. D.; Khairallah, G. N.; O'Hair, R. A. J. Gas-Phase Formation and Reactions of Radical Cations of Guanosine, Deoxyguanosine and Their Homodimers and Heterodimers. *Int. J. Mass Spectrom*. 2011, 304, 74−82.
34. Cheng, P.; Li, Y.; Li, S.; Zhang, M.; Zhou, Z. Collision-Induced Dissociation (CID) of Guanine Radical Cation in the Gas Phase: An Experimental and Computational Study. *Phys. Chem. Chem. Phys*. 2010, 12, 4667−4677.
35. Polfer, N. C., Dugourd, P., Eds. Laser Photodissociation and Spectroscopy of Mass Separated Biomolecular Ions. Lecture Notes in Chemistry; Springer: Cham, 2013; Vol. 83, pp 13−20.

36. Dunbar, R. C. Photodissociation of Trapped Ions. *Int. J. Mass Spectrom*. 2000, 200, 571−589.
37. Feketeova, L.; Khairallah, G. N.; Chan, B.; Steinmetz, V.; Maitre, P.; Radom, L.; O'Hair, R. A. J. Gas-Phase Infrared Spectrum and Acidity of the Radical Cation of 9-Methylguanine. *Chem. Commun*. 2013, 49, 7343−7345.
38. Feketeova, L.; Chan, B.; Khairallah, G. N.; Steinmetz, V.; Maitre, P.; Radom, L.; O'Hair, R. A. J. Gas-Phase Structure and Reactivity of the Keto Tautomer of the Deoxyguanosine Radical Cation. *Phys. Chem. Chem. Phys*. 2015, 17, 25837−25844.
39. Feketeova, L.; Chan, B.; Khairallah, G. N.; Steinmetz, V.; Maitre, P.; Radom, L.; O'Hair, R. A. J. Watson-Crick Base Pair Radical Cation as a Model for Oxidative Damage in DNA. *J. Phys. Chem. Lett*. 2017, 8, 3159−3165.
40. Antoine, R.; Dugourd, P. UV-Visible Activation of Biomolecular Ions. (Laser Photodissociation and Spectroscopy of Mass Separated Biomolecular Ions). Lect. Notes Chem. 2013, 83, 93−116.
41. Lesslie, M.; Lawler, J. T.; Dang, A.; Korn, J. A.; Bím, D.; Steinmetz, V.; Maitre, P.; Turecek, F.; Ryzhov, V. Cytosine Radicalˇ Cation: A Gas-Phase Study Combining IRMPD Spectroscopy, UVPD Spectroscopy, Ion−Molecule Reactions, and Theoretical Calculations. *ChemPhysChem*. 2017, 18, 1293−1301.
42. Dang, A.; Nguyen, H. T. H.; Ruiz, H.; Piacentino, E.; Ryzhov, V.; Turecek, F. Experimental Evidence for Non-Canonical Thymineˇ Cation Radicals in the Gas Phase. *J. Phys. Chem. B*. 2018, 122, 86−97.
43. Hari, Y.; Leumann, C. J.; Schurch, S. What Hinders Electron Transfer Dissociation (ETD) of DNA Cations? *J. Am. Soc. Mass Spectrom*. 2017, 28, 2677−2685.

44. Korn, J. A.; Urban, J.; Dang, A.; Nguyen, H. T. H.; Turecek, F. UV-Vis Action Spectroscopy Reveals a Conformational Collapse in Hydrogen-Rich Dinucleotide Cation Radicals. *J. Phys. Chem. Lett*. 2017, 8, 4100−4107.

45. Liu, Y.; Korn, J. A.; Dang, A.; Turecek, F. Hydrogen-Rich Cation Radicals of DNA Dinucleotides. Generation and Structure Elucidation by UV-Vis Action Spectroscopy. *J. Phys. Chem. B*. 2018, 122, 9665−9680.

46. Martens, J.; Berden, G.; Gebhardt, C. R.; Oomens, J. Infrared ion spectroscopy in a modified quadrupole ion trap mass spectrometer at the FELIX free electron laser laboratory. *Rev. Sci. Instrum*. 2016, 87, 103108/1−103108/8.

47. Shaffer, C. J.; Pepin, R.; Tureček, F. Combining UV Photodissociation Action Spectroscopy with Electron Transfer Dissociation for Structure Analysis of Gas-Phase Peptide CationRadicals. *J. Mass Spectrom*. 2015, 50, 1438−1442.

48. Frisch, M. J.; Trucks, G. W.; Schlegel, H. B.; Scuseria, G. E.; Robb, M. A.; Cheeseman, J. R.; Scalmani, G.; Barone, V.; Petersson, G. A.; Nakatsuji, H.; et al. Gaussian 16, revision A01; Gaussian, Inc.: Wallingford, CT, 2016.

49. Ř ezać , J.; Fanfrlík, J.; Salahub, D.; Hobza, P. Semi-Empiricalˇ Quantum Chemical PM6 Method Augmented by Dispersion and H Bonding Correction Terms Reliably Describes Various Types of Noncovalent Complexes. *J. Chem. Theory Comput*. 2009, 5, 1749−1760.

50. Stewart, J. J. P. MOPAC 16; Stewart Computational Chemistry: Colorado Springs, CO, 2016.

51. Ř ezać , J. Cuby: An Integrative Framework for Computationalˇ Chemistry. *J. Comput. Chem*. 2016, 37, 1230−1237.

52. Chai, J. D.; Head-Gordon, M. Long-Range Corrected Hybrid Density Functionals with Damped Atom-Atom Dispersion Corrections. *Phys. Chem. Chem. Phys*. 2008, 10, 6615−6620.
53. Zhao, Y.; Truhlar, D. G. The M06 Suite of Density Functionals for Main Group Thermochemistry, Thermochemical Kinetics, Noncovalent Interactions, Excited States, and Transition Elements: Two New Functionals and Systematic Testing of Four M06-Class Functionals and 12 Other Functionals. *Theor. Chem. Acc*. 2008, 120, 215−241.
54. Yanai, T.; Tew, D. P.; Handy, N. C. A New Hybrid Exchange Correlation Functional Using the Coulomb-Attenuating Method (CAM-B3LYP). *Chem. Phys. Lett.* 2004, 393, 51−57.
55. Tomasi, J.; Mennucci, B.; Cammi, R. Quantum Mechanical Continuum Solvation Models. *Chem. Rev*. 2005, 105, 2999−3093.
56. Møller, C.; Plesset, M. S. A Note on an Approximation Treatment for Many-Electron Systems. *Phys. Rev*. 1934, 46, 618−622
57. Dunning, T. H., Jr. Gaussian Basis Sets for Use in Correlated Molecular Calculations. I. The Atoms Boron Through Neon and Hydrogen. *J. Chem. Phys*. 1989, 90, 1007−1023.
58. Č ízek, J. On the Use of the Cluster Expansion and the ˇ Technique of Diagrams in Calculations of Correlation Effects in Atoms and Molecules. *Adv. Chem. Phys*. 2007, 14, 35−89.
59. Purvis, G. D., III; Bartlett, R. J. A. Full Coupled-Cluster Singles and Doubles Model − the Inclusion of Disconnected Triples. *J. Chem. Phys*. 1982, 76, 1910−1918.

60. Halkier, A.; Helgaker, T.; Jørgensen, P.; Klopper, W.; Koch, H.; Olsen, J.; Wilson, A. K. Basis Set Convergence in Correlated Calculations on Ne, N2, and H2O. *Chem. Phys. Lett*. 1998, 286, 243− 252.

61. Schlegel, H. B. Potential Energy Curves Using Unrestricted M?ller-Plesset Perturbation Theory with Spin Annihilation. *J. Chem. Phys*. 1986, 84, 4530.

62. Mayer, I. Spin-Projected UHF Method. IV. Comparison of Potential Curves Given by Different One-Electron Methods. *Int. J. Quantum Chem*. 1978, 14, 29−38.

63. Sekino, H.; Bartlett, R. J. A Linear Response, Coupled-Cluster Theory for Excitation Energy. *Int. J. Quantum Chem*. 1984, 26, 255− 265.

64. Comeau, D. C.; Bartlett, R. J. The Equation-of-Motion Coupled- Cluster Method. Applications to Open- and Closed-Shell Reference States. *Chem. Phys. Lett*. 1993, 207, 414−423.

65. Furche, F.; Ahlrichs, A. Adiabatic Time-Dependent Density Functional Methods for Excited State Properties. *J. Chem. Phys*. 2002, 117, 7433−7447.

66. Turecek, F. Benchmarking Electronic Excitation Energies and Transitions in Peptide Radicals. *J. Phys. Chem. A*. 2015, 119, 10101− 10111.

67. Barbatti, M.; Ruckenbauer, M.; Plasser, F.; Pittner, J.; Granucci, G.; Persico, M.; Lischka, H. Newton-X: A Surface-Hopping Program for Nonadiabatic Molecular Dynamics. Wiley Interdisciplinary Reviews: Comput. Mol. Sci. 2014, 4, 26−33.

68. Gilbert, R. G.; Smith, S. C. Theory of Unimolecular and Recombination Reactions; Blackwell Scientific Publications: Oxford, 1990; pp 52−132.

69. Zhu, L.; Hase, W. L. Quantum Chemistry Program Exchange, Program No. QCPE 644; Indiana University: Bloomington, IN, 1994.

70. Frank, A. J.; Sadílek, M.; Ferrier, J. G.; Turecek, F. Sulfur Oxoacids and Radicals in the Gas Phase. A Variable-Time Neutralization-Photoexcitation- Reionization Mass Spectrometric and Ab initio/RRKM Study. *J. Am. Chem. Soc*. 1997, 119, 12343− 12353.

71. Petroselli, G.; Dantola, M. L.; Cabrerizo, F. M.; Capparelli, A. L.; Lorente, C.; Oliveros, E.; Thomas, A. H. Oxidation of 2'- Deoxyguanosine 5′-Monophosphate Photoinduced by Pterin: Type I versus Type II Mechanism. *J. Am. Chem. Soc*. 2008, 130, 3001−3011.

72. Clark, L. B.; Peschel, G. G.; Tinoco, I. Vapor Spectra and Heats of Vaporization of Some Purine and Pyrimidine Bases. *J. Phys. Chem*. 1965, 69, 3615−3618.

73. Barbatti, M.; Aquino, A. J. A.; Lischka, H. The UV Absorption of Nucleobases: Semi-Classical ab Initio Spectra Simulations. *Phys. Chem. Chem. Phys*. 2010, 12, 4959−4967.

74. Kang, H.; Lee, K. T.; Jung, B.; Ko, Y. J.; Kim, S. K. Intrinsic Lifetimes of the Excited State of DNA and RNA Bases. *J. Am. Chem. Soc*. 2002, 124, 12958−12959.

75. Canuel, C.; Mons, M.; Piuzzi, F.; Tardivel, B.; Dimicoli, I.; Elhanine, M. Excited States Dynamics of DNA and RNA Bases: Characterization of a Stepwise Deactivation Pathway in the Gas Phase. *J. Chem. Phys*. 2005, 122, 074316.

76. Pepin, R.; Turecek, F. Kinetic Ion Thermometers for Electronˇ Transfer Dissociation. *J. Phys. Chem. B*. 2015, 119, 2818−2826.

Chapter 4: Experimental Evidence for Noncanonical Thymine Cation Radicals in the Gas Phase

Reproduced in part with permission from Dang, A.; Nguyen, H.; Ruiz, H.; Piancentino, E.; Ryzhov, V.; Tureček, F. The Journal of Physical Chemistry B. 2018, 122, 86-97.

Abstract

Thymine cation radicals were generated in the gas phase by collision induced intramolecular electron transfer in [Cu(2,2’:6,2”-terpyridine)(thymine)]$^{2+\cdot}$ complexes and characterized by ion−molecule reactions, UV−vis photodissociation action spectroscopy, and ab initio and density functional theory calculations. The experimental results indicated the formation of a tautomer mixture consisting chiefly (77%) of noncanonical tautomers with a C-7-H_2 group. The canonical 2,4-dioxo-N-1,N-3-H isomer was formed as a minor component at ca. 23%. Ab initio CCSD(T) calculations indicated that the canonical [thymine]$^{+\cdot}$ ion was not the lowest-energy isomer. This contrasts with neutral thymine, for which the canonical isomer is the lowest-energy structure. Exothermic unimolecular isomerization by a methyl hydrogen migration in the canonical [thymine]$^{+\cdot}$ ion required a low energy barrier, forming a C-7-H_2,O-4-H isomer. Noncanonical thymine tautomers with a C-7-H_2 group were also identified by calculations as low-energy isomers of 2’-deoxythymidine phosphate cation radicals. The relative energies of thymidine ion isomers were sensitive to the computational method used and were affected by solvation. The noncanonical [thymine]$^{+\cdot}$ ions have extremely low adiabatic recombination energies (RE_{adiab} < 5.9 eV), making them potential ionization hole traps in ionized nucleic acids.

4.1 Introduction

DNA ionization triggers degradation chemical reactions that can lead to DNA damage such as nucleobase loss and strand breaks.[1] The processes involved in DNA ionization have been studied at several levels, ranging from individual nucleobases through nucleotides to double-stranded oligonucleotide DNAmodels.[2−4] A phenomenon of particular interest has been the propagation of the cation-radical defect (a "hole") from the initial site, generated randomly at a nucleobase, along the DNA strand. Model studies have tremendously contributed to our understanding of the hole migration at the nanoscale level. Nucleobase cation radicals have been generated by targeted photooxidation by intercalated transition metal complexes,[5] organic groups,[6] or photoinduced electron transfer.[7] Among the DNA nucleobases, thymine has the highest ionization energy (8.8 − 9.4 eV), as established by photoelectron spectroscopy,[8 − 10] photoionization,[11,12] and computational studies.[13−16] Perhaps even more relevant for solution studies, thymine also has the highest electrochemical oxidation potential among the DNA nucleobases.[17,18] These properties make the thymine cation radical a likely electron acceptor by transfer from other nucleobases, and because of its high ionization potential, thymine might be considered a nonreactive spacer in studies of hole propagation by hopping between guanine bases.6 In contrast, recent studies of A-T-rich DNA models[19−24] demonstrated the high reactivity of the ionized thymine nucleobase. Reaction of thymidine with photoexcited 2-methyl-1,4-naphthoquinone[25,26] in the presence of molecular oxygen gave intermediates that were hydroperoxylated at the C-5 methyl group, indicating deprotonation followed by oxygen addition to the C-7-H2 radical.[27] The methyl group is also a preferred site of attack by OH radicals, forming thymine C-7-H2 radicals.[28] The reactivity of thymine cation radicals has been addressed by density functional theory (DFT) calculations in studies that focused on intra- and intermolecular proton transfer.[29−31] An important finding in these studies was the theoretical existence of a low-energy tautomer of $[\text{thymine}]^{+\cdot}$ that was separated from the canonical 2,4-dioxo form by a relatively low-energy barrier.[29]

Thymine cation radicals have been produced as transient species by photoionization[32,33] and radiolytic[34−36] or chemical oxidation[37−40] in solution, where they were exposed to solvents, additives, and side-reaction products. In contrast, the rarefied gas phase provides an ideal medium for studying isolated reactive species to investigate their intrinsic properties in the absence of solvent, counterions, and surfaces.[41] Among nucleobase radicals, hydrogen adducts of cytosine, adenine, and uracil have been generated in the gas phase by femtosecond electron transfer to the corresponding cations, and their structure, energetics, and unimolecular dissociations have been investigated.[42−44] Synthetic routes to gas-phase biomolecular cation radicals also rely on reductive or oxidative electron transfer.[45,46] For example, intramolecular oxidation of the biomolecule (M) in a complex with a transition metal (Cu^{2+}, Fe^{3+}) and an auxiliary ligand such as 2:2',6':2"-terpyridine (terpy) has been used to produce gas-phase peptide and nucleobase cation radicals.[47,48] The oxidation is driven by collision-induced dissociation (CID) of a doubly charged complex generated by electrospray ionization and selected by mass, according to the equation:

$$[\text{Cu(terpy)(M)}]^{2+\cdot} \rightarrow [\text{Cu(terpy)}]^{+} + \text{M}^{+\cdot} \qquad (1)$$

Gas-phase chemistry analogous to eq 1 has been used to generate cation radicals of 9-methylguanine[49] and cytosine,[50] as well as the more complex systems of deoxyguanosine[51] and the Watson−Crick cytosine−guanine pair.[52] The mass-selected cation radicals generated by eq 1 chemistry have been characterized by specific radical and electron transfer ion−molecule reactions,[50] infrared multiphoton dissociation (IRMPD) action spectroscopy,[49−52] and single-photon UV−vis photodissociation action (UVPD) spectroscopy.[50] The action spectroscopy methods rely on resonant photon absorption by a gas-phase ion to induce dissociation (“action”), whereby the fragment ions formed are detected by mass spectrometry.[53] Action spectra can provide a detailed characterization of vibrational modes (IRMPD) or electronic excitations (UVPD) of the gas-phase ion that are used for structure assignment. In particular, action spectroscopy has been used to elucidate structures of isomeric cytosine cation radicals[50] and deoxyadenosine dinucleotides.[46] Here, we report the generation and structure elucidation of isomeric thymine cation radicals. The high ionization energy of thymine represents a potential challenge for the efficient generation of thymine cation radicals.[54] We show that thymine cation radicals produced in the gas phase exist in unexpected, low-energy tautomeric forms of potential relevance for the process of DNA ionization.

4.2 Experimental Section

4.2.1 Materials

Thymine, thymine-6,7,7,7-d4, 2’-deoxythymidine, $Cu(NO_3)_2$, and 2,2’:6’,2”-terpyridine were purchased from Sigma-Aldrich (St. Louis, MO) and used as received. Stock solutions (1 mg mL^{-1}) of thymine and terpy were prepared in methanol, and those of thymidine and $Cu(NO_3)_2$ were made in water/methanol (50:50). The stock solutions of terpy and $Cu(NO_3)_2$ were combined in a 1:1 ratio and diluted 10-fold in methanol. An aliquot of this solution was combined with the thymine or thymidine solution, vortexed, and allowed to react for 10 min at room temperature. The resulting solution was diluted with methanol and used for direct infusion into the electrospray ion source.

4.2.2 Methods

Mass spectra were measured on an LTQ-XL-ETD linear ion trap (Thermo Electron Fisher, San Jose, CA) furnished with a home-built microspray electrospray ion source. Photodissociation action spectra were measured as described previously.[55] Briefly, a laser beam from an EKSPLA NL301G Nd:YAG laser source (Altos Photonics, Bozeman, MT) was processed and mixed by an optical parametric oscillator (PG142C, Altos Photonics), and the output was focused into the linear ion trap to drive photodissociation of stored mass-selected [thymine]$^{+\cdot}$ ions. The laser optical parametric oscillator (OPO) operates at 20 Hz with a 3−6-ns pulse width. The laser power (0.52−12.69 mJ per pulse peak) was measured at each wavelength and used to normalize the photofragment ion intensities. The spectra were reproduced twice on different days. High-resolution mass spectra were measured on an Orbitrap Velos mass spectrometer (Thermo Electron Fisher) at a resolving power of 60000. Ion−molecule reactions of mass selected [thymine]$^{+\cdot}$ ions were measured on a modified Bruker Esquire 3000 quadrupole ion trap mass spectrometer (Bruker Daltonics, Bremen, Germany) as described previously.[56] Furan, anisole, water, and acetic acid were introduced through a leak valve. The reaction time was defined by the delay between the ion isolation and product scans.

4.2.3 Calculations

Standard ab initio and density functional theory calculations were performed with the Gaussian 09 suite of programs.[57] The thymine ion and neutral geometries were optimized with the B3LYP,[58] M06-2X,[59] and ωB97X-D[60] hybrid DFT methods using the 6-311+G(2d,p) basis set. Local energy minima and first-order saddle points were characterized by harmonic frequency analysis as having the appropriate numbers of imaginary frequencies. Solvation energies were calculated with the M06-2X and ωB97X-D methods using the polarizable continuum model[61] available in Gaussian 09. Single-point energies were calculated using Møller − Plesset perturbation theory[62] truncated at second order [MP2(frozen core)] with the aug-cc-pVTZ basis set.[63] The MP2 energies were corrected for spin contamination by annihilation of higher spin states to provide spin-projected (PMP2) energies.[64,65] Alternatively, restricted open-shell calculations (ROMP2) were used for radicals.[66] Another set of single-point energies was obtained by coupled-cluster calculations with single, double, and disconnected triple excitations [CCSD(T)][67,68] using the aug-cc-pVDZ and 6-311++G(3df,2p) basis sets. The CCSD(T)/aug-cc-pVDZ calculations were expanded to aug-cc-PVTZ using the linear relationship E[CCSD(T)/aug-cc-pVTZ] ≈ E[CCSD(T)/aug-ccpVDZ] + E[PMP2/aug-cc-pVTZ] − E[PMP2/aug-cc-pVDZ].

Excited states were treated by equation-of-motion- (EOM-) CCSD calculations[69,70] using the 6-31+G(d,p) basis set. Further sets of excitation energies and oscillator strength values were obtained by time-dependent DFT (TD-DFT) calculations[71] with the M06-2X and ωB97X-D methods using the 6-31+G(d,p) and 6-311+G(2d,p) basis sets. TD-DFT calculations of polyatomic radicals have been found to show only a very weak dependence on the basis set.[50,72,73] This was also the case for $[\text{thymine}]^{+\cdot}$, where excitation energies calculated by TD-DFT for 20 excited states with the 6-31+G(d,p) and 6-311+G(2d,p) basis sets showed a close correlation ($r^2 = 0.9997$) and small root-mean-square deviations [rmsd(ΔEexc) = 0.046 eV, rmsd(λ) = 3.8 nm]. In contrast, EOM-CCSD-calculated excitation energies depend on the basis set, exhibiting a 0.1−0.2 eV downward shift upon use of a larger basis set compared [6-311++G(2d,p)] to 6-31+G(d,p).[72] Comparison of the TD-DFT and EOM-CCSD excitation wavelengths indicated a close correlation of the main lines. The M06-2X excitations showed a red shift that was coincidentally of similar magnitude as that observed using EOM-CCSD calculations with a larger basis set. Therefore, TD-DFT M06-2X/6-31+G(d,p) calculations were used to calculate electronic transitions in multiple Boltzmann-weighed configurations of thermal (300 K) ions using the Newton-X program.[74] This generated vibronically corrected absorption spectra that are discussed later in this article. Rice−Ramsperger−Kassel−Marcus (RRKM) calculations of unimolecular rate constants[75] were performed using the QCEP program[76] that was recompiled for MS-DOS[77] and run under Windows 7. Rotational states were treated adiabatically, and the microcanonical rate constants k(E,J), were Boltzmann averaged over the rotational state distribution at >298 K.

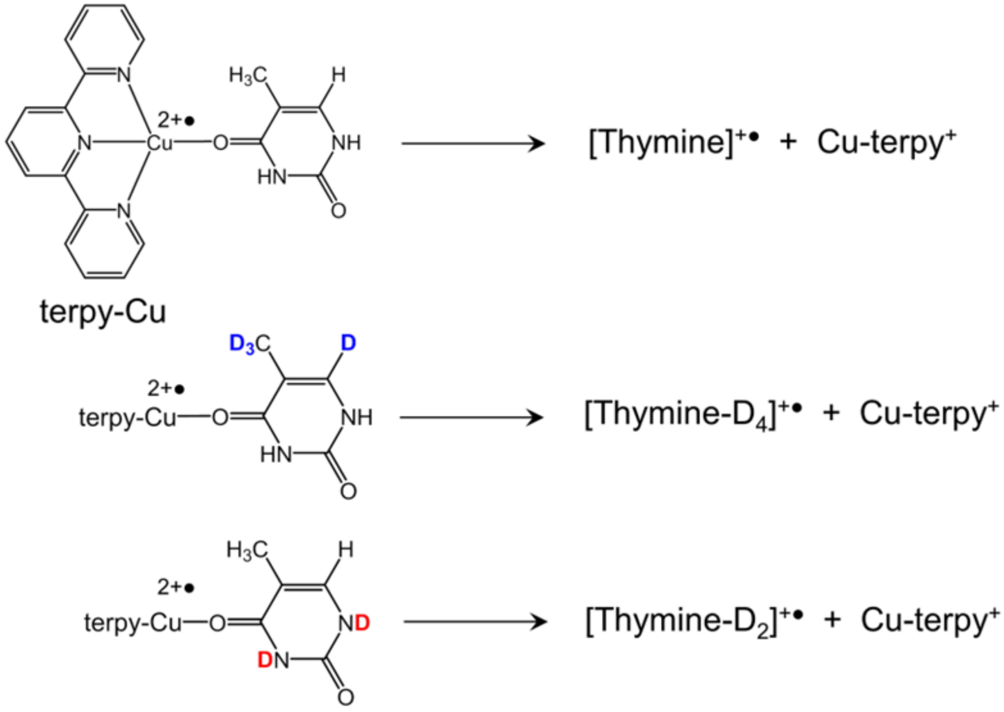

Scheme 1. Formation of [Thymine]$^{+\cdot}$ Ions from Cu-terpy Complexes

4.3 Results and Discussion

4.3.1 Generation of Thymine Cation Radicals

Thymine cation radicals were produced by collision-induced dissociation (CID) of [Cu(terpy)thymine]$^{2+\cdot}$ ions that were formed by the electrospray of water/methanol solutions containing equimolar concentrations of $Cu(NO_3)_2$, terpy, and thymine (Figure 1a). The Cu complex was isolated as a mixture of ^{63}Cu and ^{65}Cu isotopologues, and its CID resulted in a major loss of neutral thymine, forming the [Cu(terpy)]$^{2+\cdot}$ ions (*m/z* 148 and 149 for the ^{63}Cu and ^{65}Cu isotopes, respectively; 64%) and the corresponding water adducts at *m/z* 157 and 158 (30%). The competitive collision-induced intramolecular electron transfer in [Cu(terpy)thymine]$^{2+\cdot}$ yielded the complementary [thymine]$^{+\cdot}$ (*m/z* 126) and [Cu(terpy)]$^{+}$ (*m/z* 296, 298) ions that were produced in a 6% relative fragment yield. The identity of the [thymine]$^{+\cdot}$ ion was supported by accurate mass measurements (measured 126.0427, theoretical 126.0424 for $C_5H_6N_2O_2^{+\cdot}$, error < 2.5 ppm). The branching ratio of the competing channels changed only very slightly (±0.2%) with the applied collision energy. CID with electron transfer provided a sufficient [thymine]$^{+\cdot}$ ion count for further multistep tandem mass spectrometry (MS^{n}) studies. H/D exchange in D_2O/CD_3OD solution and electrospray were used to generate [Cu(terpy)(thymine-d$_2$)]$^{2+\cdot}$ precursor ions, and upon mass isolation and CID, [thymine-d$_2$]$^{+\cdot}$ ions were obtained (Scheme 1, Figure 1b). [Thymine-d$_4$]$^{+\cdot}$ ions were prepared analogously in 5.7% yield from mass-selected [^{63}Cu-(terpy)(thymine-d$_4$)]$^{2+\cdot}$ and [^{65}Cu(terpy)(thymine-d$_4$)]$^{2+\cdot}$ complexes using thymine-6,7,7,7-d$_4$ as the ligand (Figure 1c). The [thymine]$^{+\cdot}$ ions and their d$_2$

and d_4 analogues were characterized by multistep tandem mass spectrometry (CID-MS^3) spectra that showed loss of HNCO and (HNCO + CO) from [thymine]$^{+\cdot}$ and [thymine-6,7,7,7-d_4]$^{+\cdot}$. These are also major dissociations upon electron ionization of gaseous thymine.[78–81] CID-MS^3 of [thymine-1,3-d_2]$^{+\cdot}$ resulted in loss of DNCO and HNCO in a 86:14 ratio.

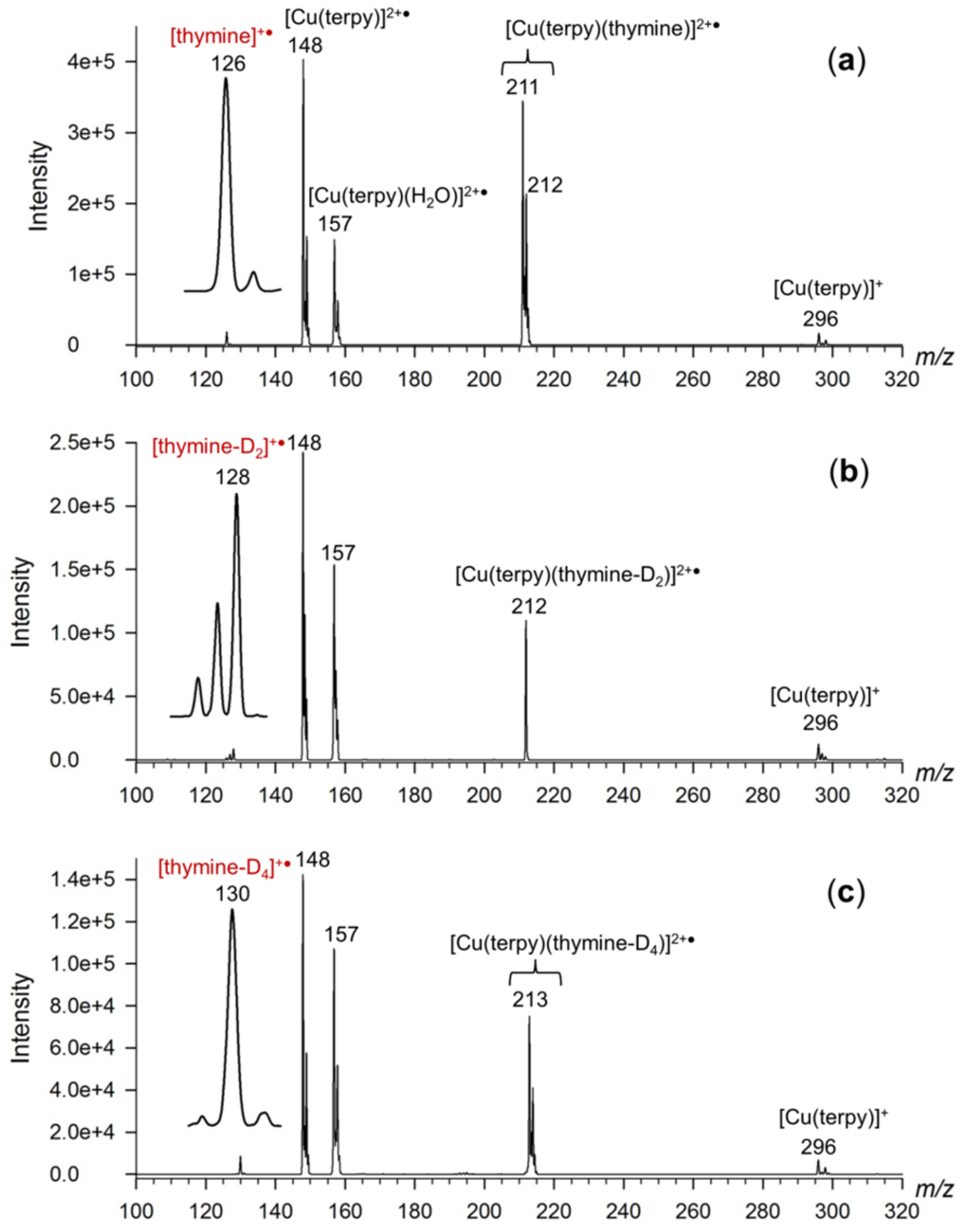

Figure 1. Collision-induced dissociation MS^2 spectra of (a) [Cu(terpy)(thymine]$^{2+\cdot}$ at *m/z* 211, 212, (b) [Cu(terpy)(thymine-1,3-D$_2$)]$^{2+\cdot}$ at *m/z* 212, 213, (c) [Cu(terpy)(thymine-6,7,7,7-D$_4$)]$^{2+\cdot}$ at *m/z* 213, 214.

4.3.2 Ion-Molecule Reactions

The mass-selected and thermalized (300 K) $[\text{thymine}]^{+\cdot}$ ions were probed by ion−molecule reactions. Exothermic charge-transfer ion−molecule reactions typically proceed at the collision rate[82] and provide a sensitive probe of ion structure in situations where isomeric ions differ in their adiabatic recombination energies (REs).[50] Previous photoelectron spectroscopic measurements[8–10] established the adiabatic ionization energy of gas-phase thymine as 8.8−9.40 eV, which is equal to the absolute value of the RE. The gas-phase charge-exchange reaction of $[\text{thymine}]^{+\cdot}$ with gaseous furan (IE = 8.88 eV) did not proceed at a measurable rate, as evidenced by the fact that <1% of $C_4H_4O^{+\cdot}$ ions formed. Upon long reaction times (5 s), we observed a minor (2%) $C_4H_5O^+$ product from proton transfer to furan. Interestingly, the charge-exchange reaction of $[\text{thymine}]^{+\cdot}$ with gaseous anisole (IE = 8.42 eV) proceeded incompletely (Figure 2). The relative intensities of the $[\text{thymine}]^{+\cdot}$ (*m/z* 126) and $[\text{anisole}]^{+\cdot}$ (*m/z* 108) ions showed a bimodal time course that was fitted with an exponential equation for the $[\text{thymine}]^{+\cdot}$ relative intensity I(t): $I(t) = I_0(0.77 + 0.23e^{-5.15t})$, giving a 1.6% root-mean-square deviation (rmsd). This left 77% nonreactive $[\text{thymine}]^{+\cdot}$ ions after ca. 1 s. This surprising result indicated that the population of $[\text{thymine}]^{+\cdot}$ produced from the $[\text{Cu(terpy)thymine}]^{2+\cdot}$ complex consisted of only a minor fraction of isomers with RE > 8.42 eV, whereas the major fraction of isomers had low recombination energies preventing charge transfer to anisole.

To investigate these new isomers, we performed additional ion−molecule reactions investigating proton transfer of $[\text{thymine-1,3-}d_2]^{+\cdot}$ and $[\text{thymine-6,7,7,7-}d_4]^{+\cdot}$ with gaseous water and acetic acid. $[\text{Thymine-1,3-}d_2]^{+\cdot}$, with a canonical 2,4-dioxo structure, has the N-1-D and N-3-D in exchangeable positions and was expected to undergo gas-phase D/H exchange, gradually forming $[\text{thymine-}d_1]^{+\cdot}$ and $[\text{thymine}]^{+\cdot}$ ions. The time course of the D/H exchange reaction with residual water that was measured in the linear ion trap can be expressed by the following pseudo first-order kinetic equation: I(thymine-d_2) = $I_0e^{-0.135t}$ with rmsd = 2.3%. These experiments established that the water partial pressure in the ion trap was sufficient to promote D/H exchange in exchangeable positions of the trapped ions.

In contrast, the canonical 2,4-dioxo isomer of [thymine-6,7,7,7-d_4]$^{+\cdot}$ has the deuterium in nonexchangeable C−D positions and was not expected to undergo D/H exchange with water vapor. Nevertheless, the [thymine-6,7,7,7-d_4]$^{+\cdot}$ ion was found to undergo slow D/H exchange in the gas-phase reaction with water and acetic acid, forming the d_3 isotopologue. This result indicates that a fraction of the [thymine-6,7,7,7-d_4]$^{+\cdot}$ ions formed from the [Cu(terpy)]$^{2+\cdot}$ complex did not have the canonical structure but rather underwent a prototropic rearrangement that moved the CD_3 or 6-D atoms into an exchangeable position (O-2 or O-4). In addition, these isomers must have recombination energies of <8.4 eV to be consistent with the above-mentioned charge-exchange measurements. Considering the 0.23 mole fraction of canonical [6,7,7,7-d_4]-2,4-dioxo isomer that cannot undergo D/H exchange, the [thymine-6,7,7,7-d_4]$^{+\cdot}$ mole fraction from D/H exchange with water was fitted with the bimodal curve $I(t) = I_0(0.77e^{-0.033t} + 0.23)$ with rmsd = 0.9%. Independent D/H exchange measurements with water and acetic acid vapor in a three-dimensional ion trap yielded very similar fits.

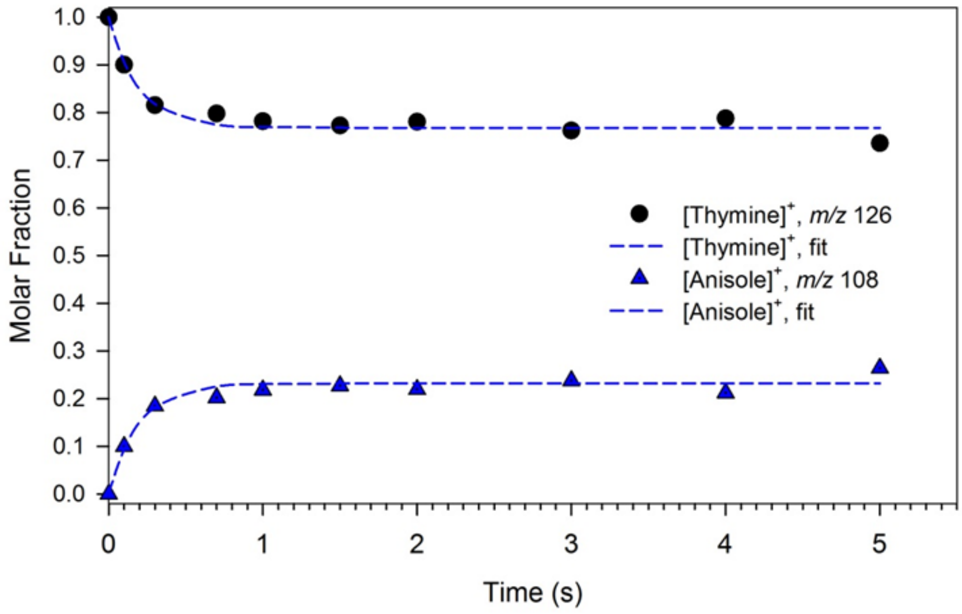

Figure 2. Kinetics of charge exchange between [thymine]$^{+\cdot}$ (*m/z* 126) and anisole, forming [anisole]$^{+\cdot}$ at *m/z* 108.

4.3.3 UV-Vis Action Spectroscopy

To further characterize the [thymine]$^{+\cdot}$ ions, we obtained photodissociation action spectra that were collected in the 210−700-nm range (Figure 3). Photodissociation proceeded in two major channels, which were the loss of HNCO and the loss of (HNCO + CO), forming the *m/z* 83 and *m/z* 55 fragment ions, respectively. Note that these fragments were also observed upon CID of [thymine]$^{+\cdot}$. The wavelength profiles of the relative intensities of the *m/z* 83 and *m/z* 55 fragment ions overlapped but showed different maxima. The *m/z* 83 ion exhibited a broad band with a maximum at 520 nm. The *m/z* 55 ion exhibited multiple bands: a weak broad band with a maximum at 580, bands at 460 and 350 nm, and a strong UV band at 260 nm. The bands in the visible and near-UV regions are absent in the UV spectrum of neutral and protonated thymine[83] and represent a signature of the cation-radical chromophores. To interpret the action spectrum of [thymine]$^{+\cdot}$, we performed extensive ab initio calculations of isomeric ion structures and excitation energies, as described in the next sections.

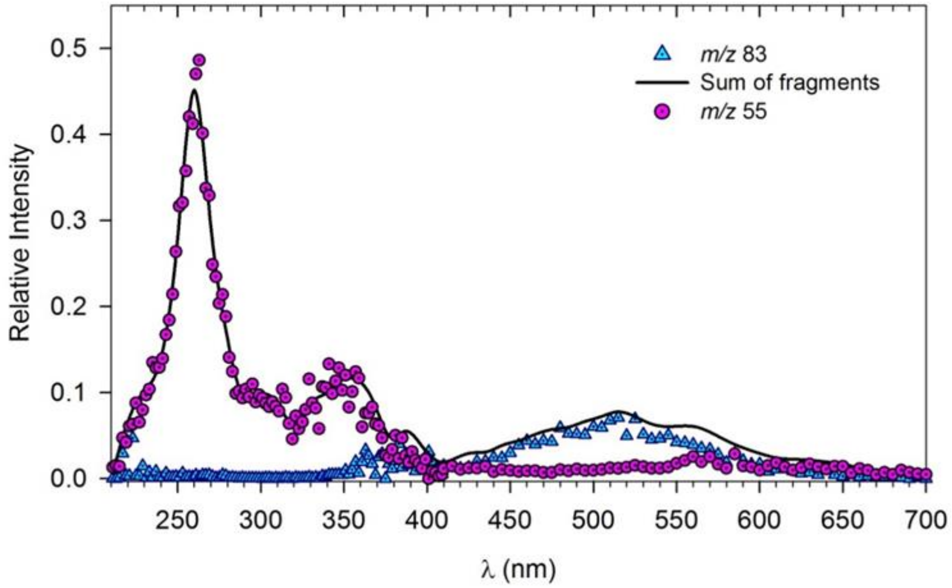

Figure 3. UV−vis photodissociation action spectrum of [thymine]$^{+\cdot}$ from [Cu(terpy)-thymine]$^{2+\cdot}$.

4.3.4 Thymine Cation Radical Structures

Thymine cation radicals can form several tautomers including those in which a hydrogen from the CH_3 group has migrated into a ring position.[29] We obtained optimized structures and DFT relative energies of 18 [thymine]$^{+\cdot}$ isomers (Table 1), and 11 low-energy structures were evaluated by CCSD(T) single-point energy calculations. Structures of the low-energy isomers are shown in Figure 4. The canonical 2,4-dioxo tautomer $1^{+\cdot}$ was the lowest-energy structure among the cation radicals having the CH_3 group ($1^{+\cdot} - 7^{+\cdot}$). This is analogous to neutral thymine, for which the canonical form is the most stable isomer in the gas phase.[84,85] In contrast, four isomers having the C-7-H_2 group, $8^{+\cdot}$−$11^{+\cdot}$, had a free energy that was lower than or comparable to that of $1^{+\cdot}$. The lowest-energy isomer, $8^{+\cdot}$, having the N-1-H, O-2-H, and O-4-H protonation pattern, was 24 kJ mol^{-1} more stable than $1^{+\cdot}$, according to the calculated ΔGg° at the experimental temperature of 310 K. Two other isomers that had free energies comparable to that of $1^{+\cdot}$ were $9^{+\cdot}$, with the N-1-H, N-3-H, and O-4-H protonation pattern, and $10^{+\cdot}$, with the N-1-H, O-2-H, and N-3-H protonation pattern. Another isomer ($11^{+\cdot}$) was 12 kJ mol^{-1} less stable than 1+· at 310 K.

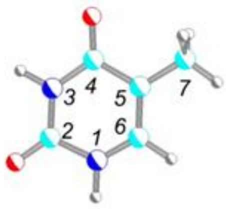

$1^{+\bullet}$

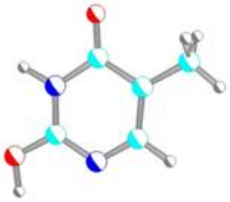

$2^{+\bullet}$

$3^{+\bullet}$

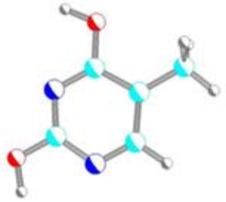

$4^{+\bullet}$

$5^{+\bullet}$

$6^{+\bullet}$

$7^{+\bullet}$

$8^{+\bullet}$

$9^{+\bullet}$

$10^{+\bullet}$

$11^{+\bullet}$

Figure 4. M06-2X/6-31+G(d,p)-optimized structures of [thymine]$^{+\cdot}$ cation radicals. Atom color coding: turquoise, C; gray, H; blue, N; red, O.

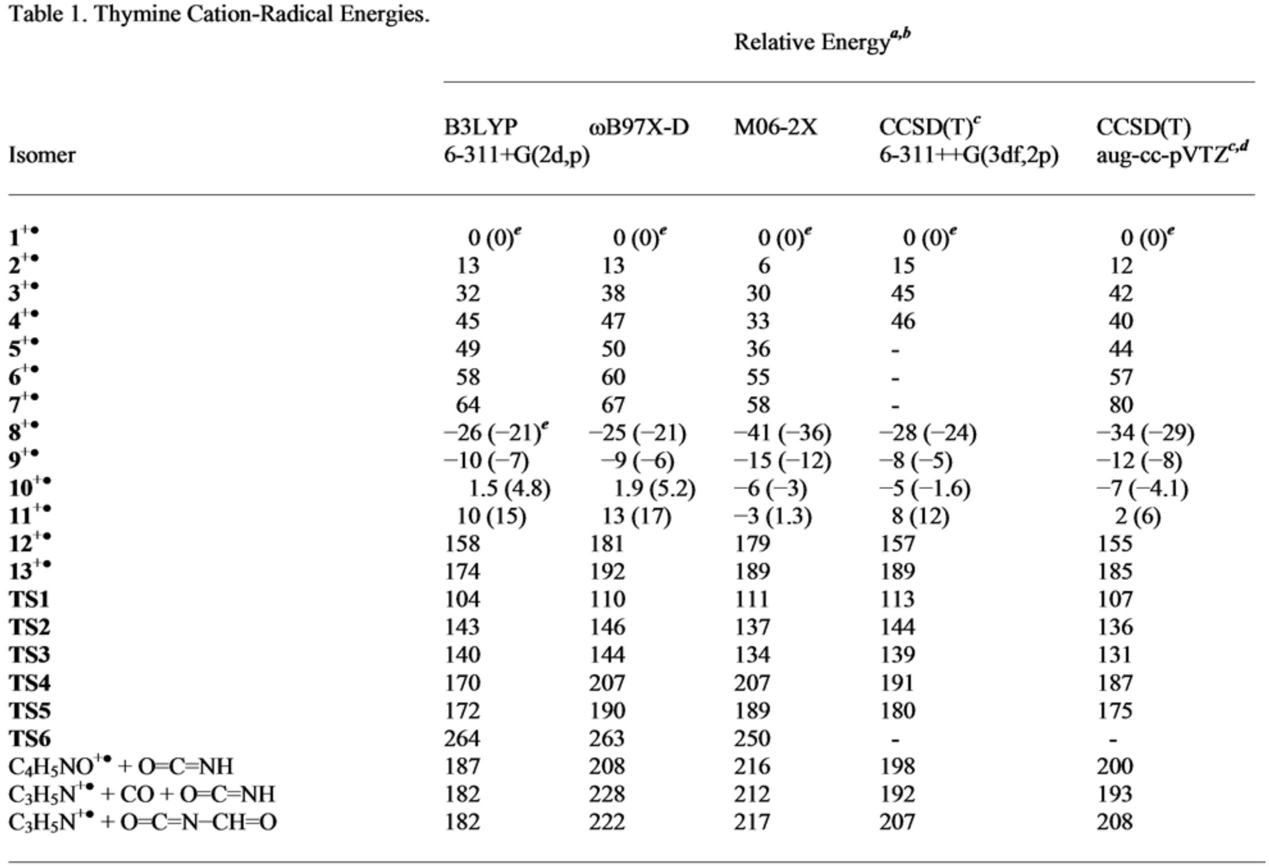

Table 1. Thymine Cation-Radical Energies.

	Relative Energy^{a,b}				
Isomer	B3LYP 6-311+G(2d,p)	ωB97X-D	M06-2X	CCSD(T)^{c} 6-311++G(3df,2p)	CCSD(T) aug-cc-pVTZ^{c,d}
$1^{+\bullet}$	0 (0)^{e}	0 (0)^{e}	0 (0)^{e}	0 (0)^{e}	0 (0)^{e}
$2^{+\bullet}$	13	13	6	15	12
$3^{+\bullet}$	32	38	30	45	42
$4^{+\bullet}$	45	47	33	46	40
$5^{+\bullet}$	49	50	36	-	44
$6^{+\bullet}$	58	60	55	-	57
$7^{+\bullet}$	64	67	58	-	80
$8^{+\bullet}$	−26 (−21)^{e}	−25 (−21)	−41 (−36)	−28 (−24)	−34 (−29)
$9^{+\bullet}$	−10 (−7)	−9 (−6)	−15 (−12)	−8 (−5)	−12 (−8)
$10^{+\bullet}$	1.5 (4.8)	1.9 (5.2)	−6 (−3)	−5 (−1.6)	−7 (−4.1)
$11^{+\bullet}$	10 (15)	13 (17)	−3 (1.3)	8 (12)	2 (6)
$12^{+\bullet}$	158	181	179	157	155
$13^{+\bullet}$	174	192	189	189	185
TS1	104	110	111	113	107
TS2	143	146	137	144	136
TS3	140	144	134	139	131
TS4	170	207	207	191	187
TS5	172	190	189	180	175
TS6	264	263	250	-	-
$C_4H_5NO^{+\bullet}$ + O=C=NH	187	208	216	198	200
$C_3H_5N^{+\bullet}$ + CO + O=C=NH	182	228	212	192	193
$C_3H_5N^{+\bullet}$ + O=C=N−CH=O	182	222	217	207	208

[a] Including B3LYP/6-311+G(2d,p) zero-point energy corrections and referring to 0 K unless stated otherwise. [b] Single-point energies on MP2(full)/6-31G(d,p)-optimized geometries. [c] From basis set expansion of aug-cc-pVDZ → aug-cc-pVTZ. [d] Values in parentheses are relative free energies at 310 K.

In contrast to the cation radicals, neutral thymine tautomers 8, 10, and 11, with the C-7-H$_2$ group, were >260 kJ mol^{-1} less stable than 1 (Table 2). Neutral isomer 9 was found to be a transition state (TS) that collapsed to 1 upon O−H rotation. The high energies of neutral species 8, 10, and 11 combined with the low energies of the respective cation radicals resulted in extremely low (<5.9 eV) adiabatic recombination energies for the cation radicals (Table 2). This result is consistent with the charge-exchange experiments, in which 77% of [thymine]$^{+\cdot}$ cation radicals were found to have very low ionization energies. Considering that the calculated adiabatic recombination energies of $8^{+\cdot}$, $9^{+\cdot}$, and $11^{+\cdot}$ are well below those of volatile organic and inorganic atoms and molecules with the exception of alkali metals, experimental determination of the RE_{adiab} values by charge-exchange bracketing of $[thymine]^{+\cdot}$ ions would be difficult.

Table 2. Relative and Adiabatic Ionization Energies of Neutral Thymine Isomers.

	relative energy^{a,b}				
species	B3LYP^{c}	M06-2X^{c}	ωB97X-D^{c}	CCSD(T)^{d}	CCSD(T)^{e}
1	0 (842)^{f}	0 (857)	0 (844)	0 (854)	0 (860)
2	45 (810)	38 (826)	47 (810)	42 (827)	39 (833)
4	55 (832)	40 (850)	57 (833)	50 (851)	44 (856)
8	267 (550)	265 (551)	286 (533)	276 (550)	269 (557)
10	280 (564)	287 (564)	302 (544)	287 (563)	282 (571)
11	288 (565)	287 (568)	308 (549)	299 (563)	291 (570)

[a]Including B3LYP zero-point vibrational energies and referring to 0 K. [b]Calculations with the 6-311+G(2dp) basis set. [c]From single-point calculations with the 6-311++G(3df,2p) basis set. [d]From effective CCSD(T)/aug-cc-pVTZ single-point calculations. [e]Adiabatic ionization energies in kJ mol^{-1} in parentheses.

4.3.5 Electronic Excitations

We used the optimized structures of the low-energy isomers $1^{+\cdot}$ and $8^{+\cdot}$−$11^{+\cdot}$ to calculate the excitation energies and oscillator strengths and obtain absorption spectra for comparison with the experimental photodissociation action spectrum of $[thymine]^{+\cdot}$. The spectra of all of the low-energy isomers showed a major band at 245−270 nm, although this band was notably weaker in the spectrum of $1^{+\cdot}$ (Figure 5a). This band appears at 260 nm in the action spectrum of [thymine]$^{+\cdot}$ and cannot be used to represent a specific isomer. The spectra of $8^{+\cdot}$ and $10^{+\cdot}$ are the only ones showing a distinct band at 330–360 nm to match the 330–360-nm band in the action spectrum of [thymine]$^{+\cdot}$ (Figure 5b,d). This indicates that $8^{+\cdot}$ or $10^{+\cdot}$ or both are present in the [thymine]$^{+\cdot}$ ion population. The long-wavelength bands in the visible region of the spectrum are also diagnostic. The broad band at 550–600 nm represented by the *m/z* 55 photodissociation channel in the action spectrum can be matched by the 550- and 615-nm bands in the absorption spectra of $1^{+\cdot}$ and $9^{+\cdot}$ (panels a and c, respectively, of Figure 5). Likewise, the 500-nm band represented by the *m/z* 83 photodissociation channel in the action spectrum finds analogous bands in the spectra of $8^{+\cdot}$ and $11^{+\cdot}$ (panels b and e, respectively, of Figure 5). The minor band at 460 nm represented by the *m/z* 55 photodissociation channel in the action spectrum has an analogue in the absorption spectrum of $10^{+\cdot}$ (Figure 5d). From this comparison, it is clear that the action spectrum of [thymine]$^{+\cdot}$ cannot be represented by a spectrum of a single ion isomer, indicating that the gas-phase ions were a mixture of isomers. This conclusion is consistent with the results of the ion–molecule reactions, as described above. We did not attempt to quantify the fractions of the individual noncanonical [thymine]$^{+\cdot}$ isomers whose spectra compose the action spectrum. This is because photodissociation, especially at short wavelengths (210–250 nm, ≥ 5 eV photon energy), could lead to consecutive dissociations of the primary photofragments to yield low-mass secondary ions that would fall below the low-mass cutoff of the ion trap and thus be undetectable in the mass spectra. This could skew the band intensities and affect quantitation.

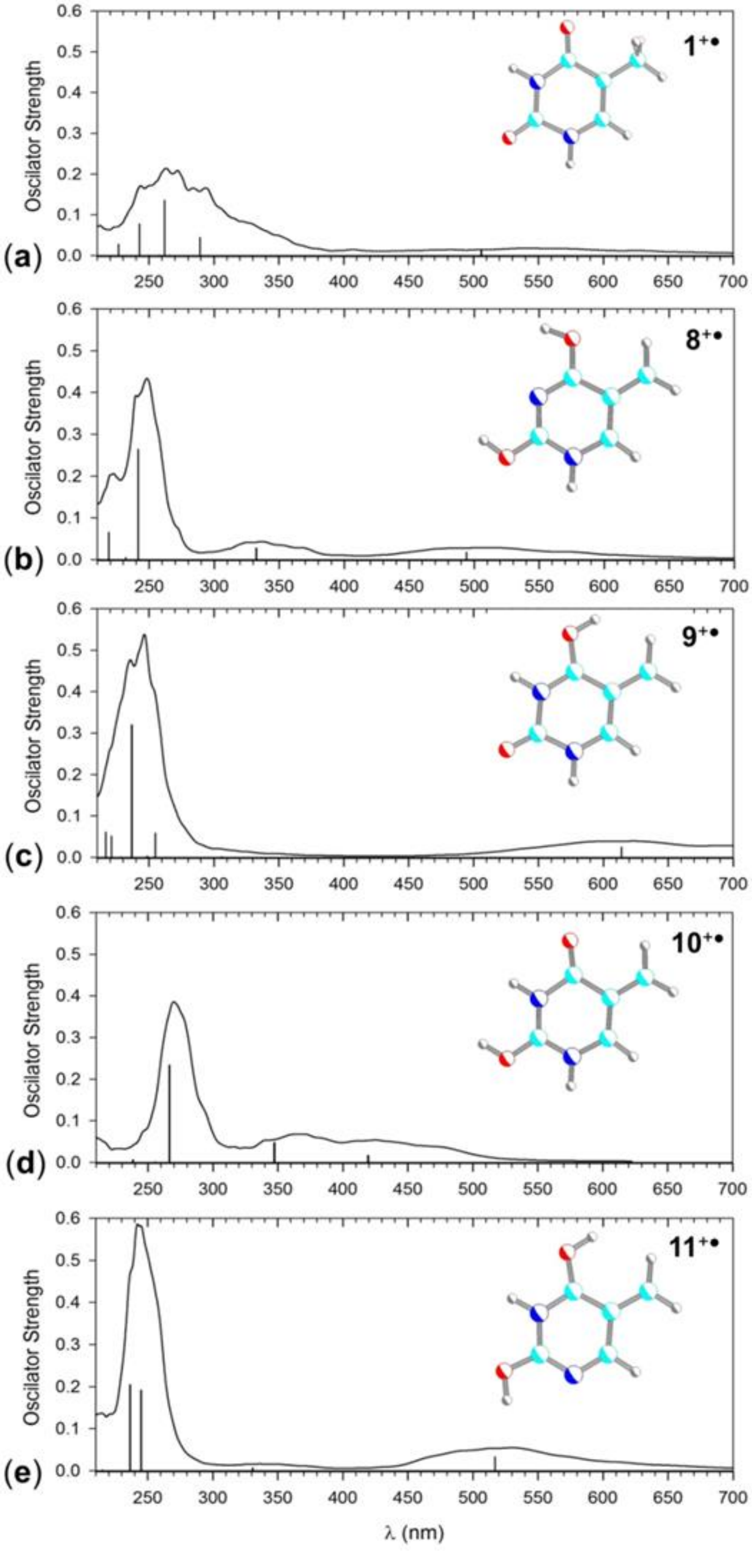

Figure 5. Vibronically broadened (300 K) TD-DFT M06-2X/6-31+G(d,p) absorption spectra of (a) $1^{+\cdot}$, (b) $8^{+\cdot}$, (c) $9^{+\cdot}$, (d) $10^{+\cdot}$, and (e) $11^{+\cdot}$. The bars represent the calculated vertical transitions.

4.3.6 Potential Energy Surface for [Thymine]$^{+\cdot}$

The experimental evidence for the formation of [thymine]$^{+\cdot}$ isomers other than the canonical form $1^{+\cdot}$ raised the question of the stage at which the isomerization occurs. Neutral thymine is present in solution in its canonical 2,4-dixo form. Isomerization could potentially occur in solution upon binding in the [Cu(terpy)-(thymine)]$^{2+\cdot}$ complex or upon collisional activation in the gas phase. We address the latter possibility first. The potential energy surface for the important steps in the isomerization and dissociation of gas-phase $1^{+\cdot}$ was obtained by CCSD(T) single-point energy calculations including zero-point vibrational energy corrections (Figure 6). For energies calculated at other levels of theory, see Table 1. Whereas isomerizations of $1^{+\cdot}$ to $8^{+\cdot} - 10^{+\cdot}$ were found to be exothermic, the initial step, which is H-atom migration from the methyl group to O-4 forming $9^{+\cdot}$, required that an energy barrier be overcome in TS1. The energy barriers for consecutive H-atom migrations, interconnecting $9^{+\cdot}$ with $8^{+\cdot}$ and $8^{+\cdot}$ with $10^{+\cdot}$ (TS2 and TS3, respectively), were found to be 26–30 kJ mol^{-1} higher than that for TS1.

In contrast, energy barriers to a ring opening en route to dissociation had substantially higher TS energies for cleavage of the N-1–C-2 and N-3–C-4 bonds. The transition state for the N-1–C-2 bond cleavage (TS4) was 188 kJ mol–1 relative to that of $1^{+\cdot}$, leading to a complex of O=C=NH and $C_4H_5NO^{+\cdot}$ ($12^{+\cdot}$) at 156 kJ mol^{-1} (Figure 6, Table 1). The transition state for the N-3–C-4 bond cleavage (TS5) was 175 kJ mol^{-1} relative to that of $1^{+\cdot}$, possibly forming a high-energy intermediate ($13^{+\cdot}$) after rotation about the N-1–C-6 bond. The thresholds for the formation of the observed dissociation products ($C_4H_5NO^{+\cdot}$ + O=C=NH), ($C_3H_4N^{+\cdot}$ + CO +

O=C=NH), and ($C_3H_4N^{+\cdot}$ + O=CH−N=C=O), were 200, 193, and 208 kJ mol^{-1}, respectively, relative to the thresholds for $1^{+\cdot}$. Ring opening by N-1−C-2 bond cleavage in $9^{+\cdot}$ was unfavorable, requiring 260 kJ mol^{-1} in the pertinent transition state (TS6, Table 1).

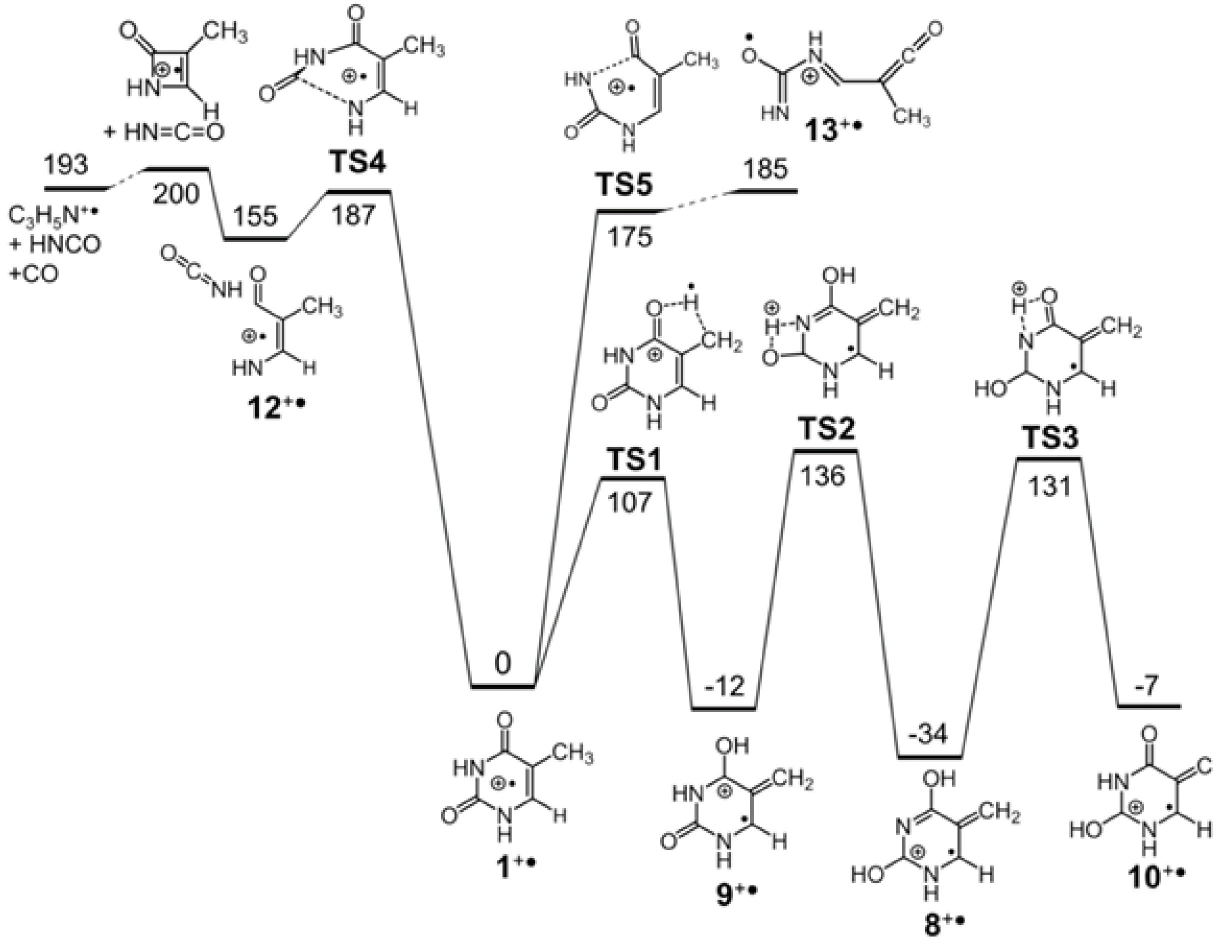

Figure 6. Potential energy surface (kJ mol^{-1}) for isomerizations and dissociations of $1^{+\cdot}$. Energies relative to $1^{+\cdot}$ are from effective CCSD(T)/aug-ccpVTZ calculations. For energies from the other calculations, see Table 1.

The kinetics for a reversible isomerization of $1^{+\cdot}$ to $9^{+\cdot}$ and further to $8^{+\cdot}$ and $10^{+\cdot}$ was evaluated from unimolecular rate constants obtained by RRKM calculations. At internal energies between E(TS1) and E(TS2), $1^{+\cdot}$ rapidly isomerized to $9^{+\cdot}$, reaching an equilibrium within 50 ms at internal energies greater than 128 kJ mol^{-1} (Figure 7a). Note that 50 ms is a benchmark ion residence time in the ion trap. Interestingly, although $9^{+\cdot}$ had a lower ΔH_0 value than $1^{+\cdot}$, the equilibrium fraction of $9^{+\cdot}$ was close to 50% and further decreased with increasing internal energy. This is caused by a higher density of vibrational states in $1^{+\cdot}$, increasing its entropy. The $1^{+\cdot} \rightarrow 9^{+\cdot}$ isomerization showed a substantial combined isotope effect that slowed the isomerization of 6,7,7,7-d_4-$1^{+\cdot}$ more than 5-fold at internal energies below 150 kJ mol^{-1}. At internal energies above 170 kJ mol^{-1}, the subsequent isomerizations of $9^{+\cdot}$, $8^{+\cdot}$, and $10^{+\cdot}$ also became fast, allowing the system to reach an equilibrium including $1^{+\cdot}$, $8^{+\cdot}$, $9^{+\cdot}$, and $10^{+\cdot}$. The equilibrium mole fractions were found to be energy-dependent (Figure 7b), whereby that of $1^{+\cdot}$ was increasing whereas that of $8^{+\cdot}$ was decreasing at high internal energies. The N-1−C-2 and N-3−C-4 modes of ring opening became kinetically relevant at internal energies of >190 kJ mol^{-1}, where the rate constants reached 14 s^{-1} for 50% reaction at 50 ms. The high threshold energy for the ring opening explains why $1^{+\cdot}$ can undergo extensive isomerization by reversible hydrogen migrations to generate a mixture of non-dissociating [thymine]$^{+\cdot}$ ions. The RRKM kinetics also suggest that the dissociation of thermal [thymine]$^{+\cdot}$ having a mean internal energy of 24 kJ mol^{-1} at 310 K can be promoted by an absorption of >176 kJ mol^{-1} energy, corresponding to a single 680-nm photon.

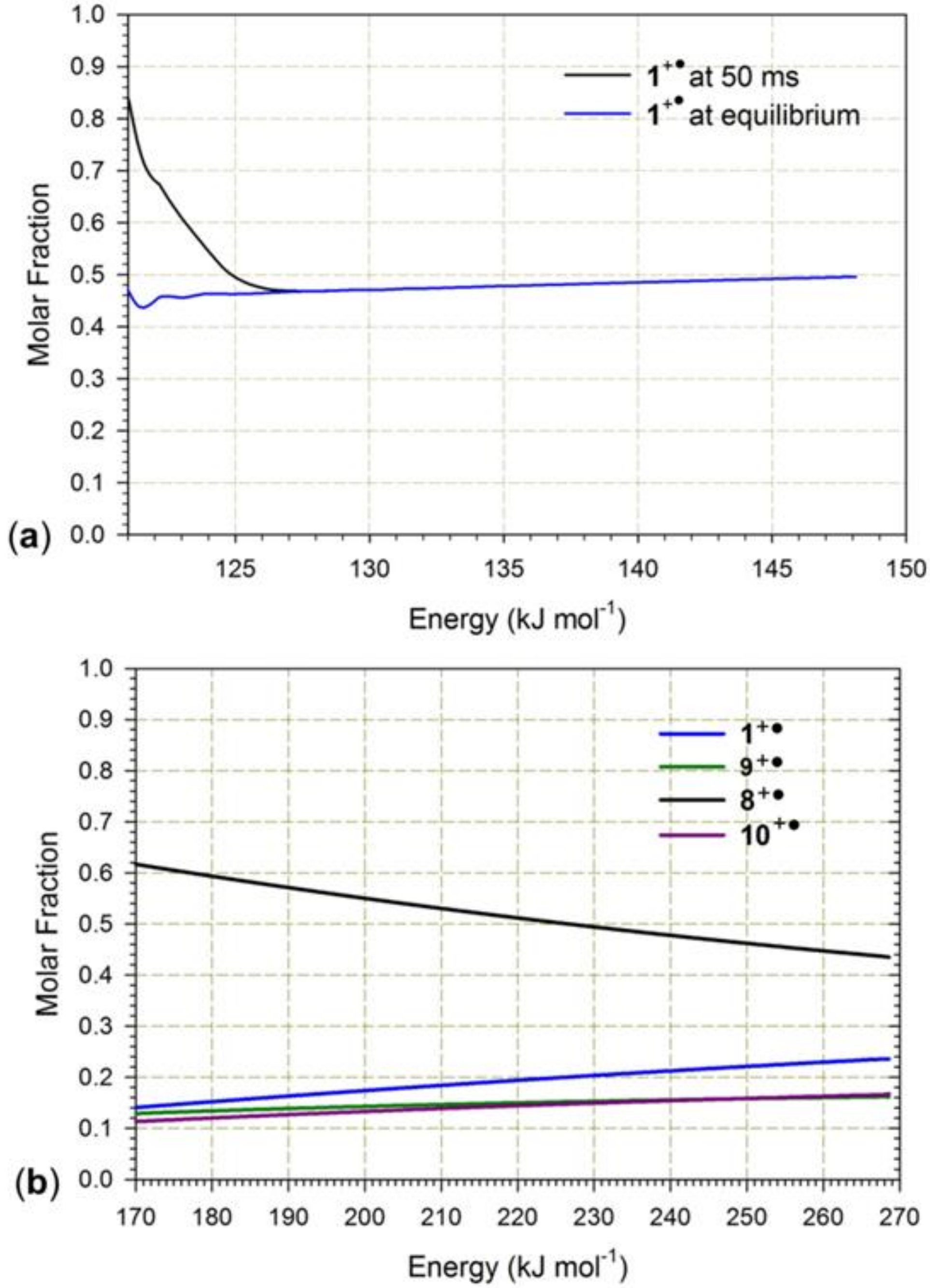

Figure 7. Mole fractions of $1^{+\cdot}$, $8^{+\cdot}$, $9^{+\cdot}$, and $10^{+\cdot}$ from RRKM calculations of isomerization rate constants. (a) Kinetics of reversible $1^{+\cdot} \leftrightarrow 9^{+\cdot}$ isomerization at low internal energies and (b) equilibrium mole fractions at high internal energies.

4.3.7 Formation of [Thymine]$^{+\cdot}$ from the [Cu(terpy)-(thymine)]$^{2+\cdot}$ Complex

The formation of unusual [thymine]$^{+\cdot}$ isomers upon CID of the [Cu(terpy)(thymine)]$^{2+\cdot}$ complex also raised the question of whether thymine coordination to Cu^{2+} in solution could lead to isomerization. We investigated by DFT calculations the relative energies of several [Cu(terpy)(thymine)]$^{2+\cdot}$ complexes in which the thymine ligands were different tautomers of the neutral molecule (Figure 8, Table 3). According to these calculations, the complex with an O-4-linked 1, [Cu(terpy)(O-4-1)]$^{2+\cdot}$, was the lowest-energy structure in both the gas phase and aqueous and methanol solutions, followed by the complexes with an O-2-linked 1 and an O-4-linked 2. In contrast, Cu(terpy) complexes with 8, 9, and 10 were >120 kJ mol^{-1} less stable than [Cu(terpy)(O-4-1)]$^{2+\cdot}$ and were unlikely to be present under equilibrium conditions in solution or formed by electrospray in the gas phase. We conclude that the formation of gas-phase $8^{+\cdot} - 11^{+\cdot}$ most likely occurs as a result of collisional excitation and dissociation of the [Cu(terpy)(thymine]$^{2+\cdot}$ complex that produces a fraction of [thymine]$^{+\cdot}$ ions with internal energies of >128 kJ mol^{-1} for kinetically relevant isomerization.

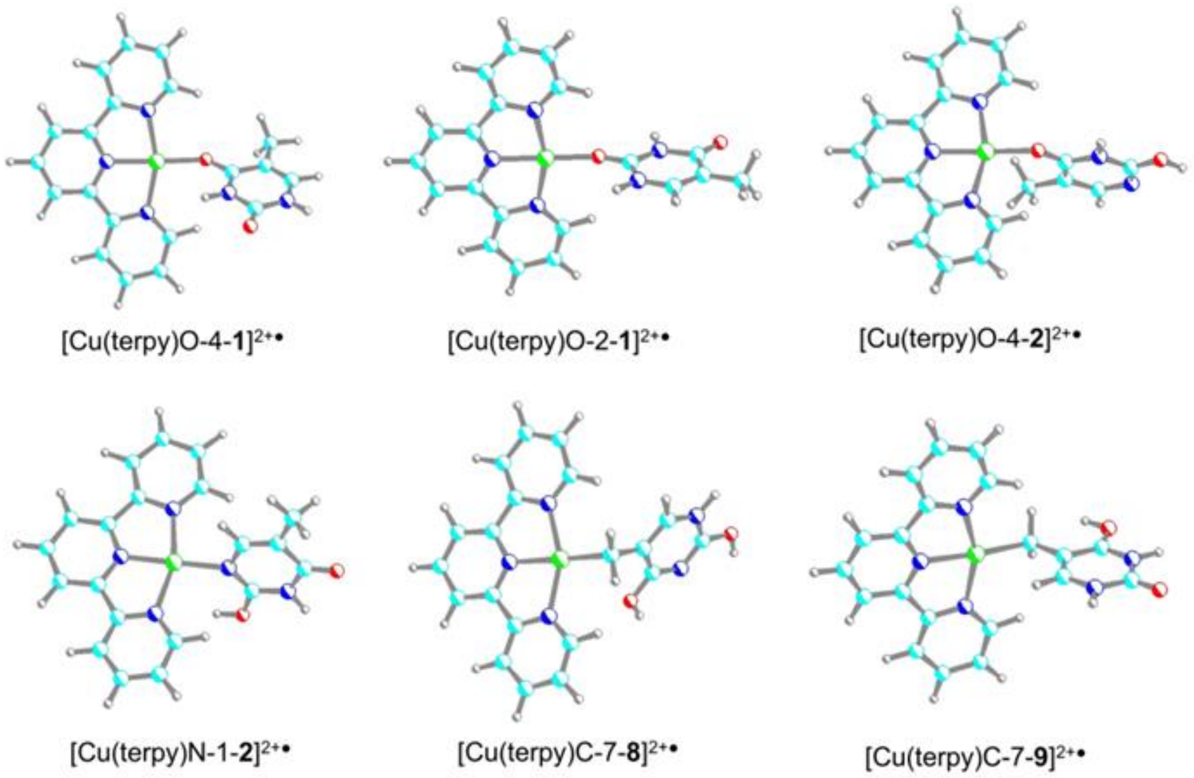

[Cu(terpy)O-4-**1**]$^{2+\bullet}$ [Cu(terpy)O-2-**1**]$^{2+\bullet}$ [Cu(terpy)O-4-**2**]$^{2+\bullet}$

[Cu(terpy)N-1-**2**]$^{2+\bullet}$ [Cu(terpy)C-7-**8**]$^{2+\bullet}$ [Cu(terpy)C-7-**9**]$^{2+\bullet}$

Figure 8. M06-2X/6-311+G(2d,p)-optimized structures of [Cu(terpy)(thymine)]$^{2+\cdot}$ complexes.

Table 3. Relative Energies of [Cu(terpy)(thymine)]$^{2+\bullet}$ Complexes.

	relative energy^{a,b}		
complex	B3LYP^{c}	M06-2X^{c}	ωB97X-D^{c}
[Cu(terpy)→O-4-**1**]$^{2+\bullet}$	0	0 (0)^{d}	0 (0)
[Cu(terpy)→O-2-**1**]$^{2+\bullet}$	17	16 (7)	20 (12)
[Cu(terpy)→O-4-**2**]$^{2+\bullet}$	36	7 (31)	19 (43)
[Cu(terpy)→N-1-**2**]$^{2+\bullet}$	86	76 (49)	78 (49)
[Cu(terpy)→N-3-**9**]$^{2+\bullet}$	120	145 (182)	125 (159)
[Cu(terpy)→C-7-**9**]$^{2+\bullet}$	130	128 (159)	125 (155)
[Cu(terpy)→C-7-**8**]$^{2+\bullet}$	154	159 (158)	145 (142)

[a] Including B3LYP/6-311+G(2d,p) zero-point energy corrections and referring to 0 K. [b] Calculations with the 6-311+G(2d,p) basis set. [c] Values in parentheses include solvation energies in the polarizable continuum of water.

4.3.8 Thymidine Cation Radicals

We attempted to generate 2'-deoxythymidine cation radicals by collision-induced intramolecular electron transfer in the $[Cu(terpy)(thymidine)]^{2+\cdot}$ complex. The precursor ion was successfully made by electrospray ionization (*m/z* 269 and 271 for the ^{63}Cu and ^{65}Cu isotopes, respectively). However, CID of $[Cu(terpy)(thymidine)]^{2+\cdot}$ resulted in a dissociation of the N-glycosidic bond forming the complementary deoxyribosyl ($C_5H_9O_3^+$, *m/z* 117) and $[Cu(terpy)(thymine)]^{+\cdot}$ (*m/z* 421) singly charged fragment ions. The major CID product was the $[Cu(terpy)(thymine)]^{2+\cdot}$ ion (*m/z* 211), which, upon mass isolation and CID-MS^3 gave the $[thymine]^{+\cdot}$ ion, which, according to its UVPD and CID spectra was identical to the ion formed directly from the doubly charged thymine complex. The unequivocal course of dissociation of the $[Cu(terpy)(thymidine)]^{2+\cdot}$ complex indicates that the cleavage of the 2'-deoxythymidine glycosidic bond is energetically more favorable than the electron-transfer reaction forming $[thymidine]^{+\cdot}$ and $[Cu(terpy)]^+$ ions.

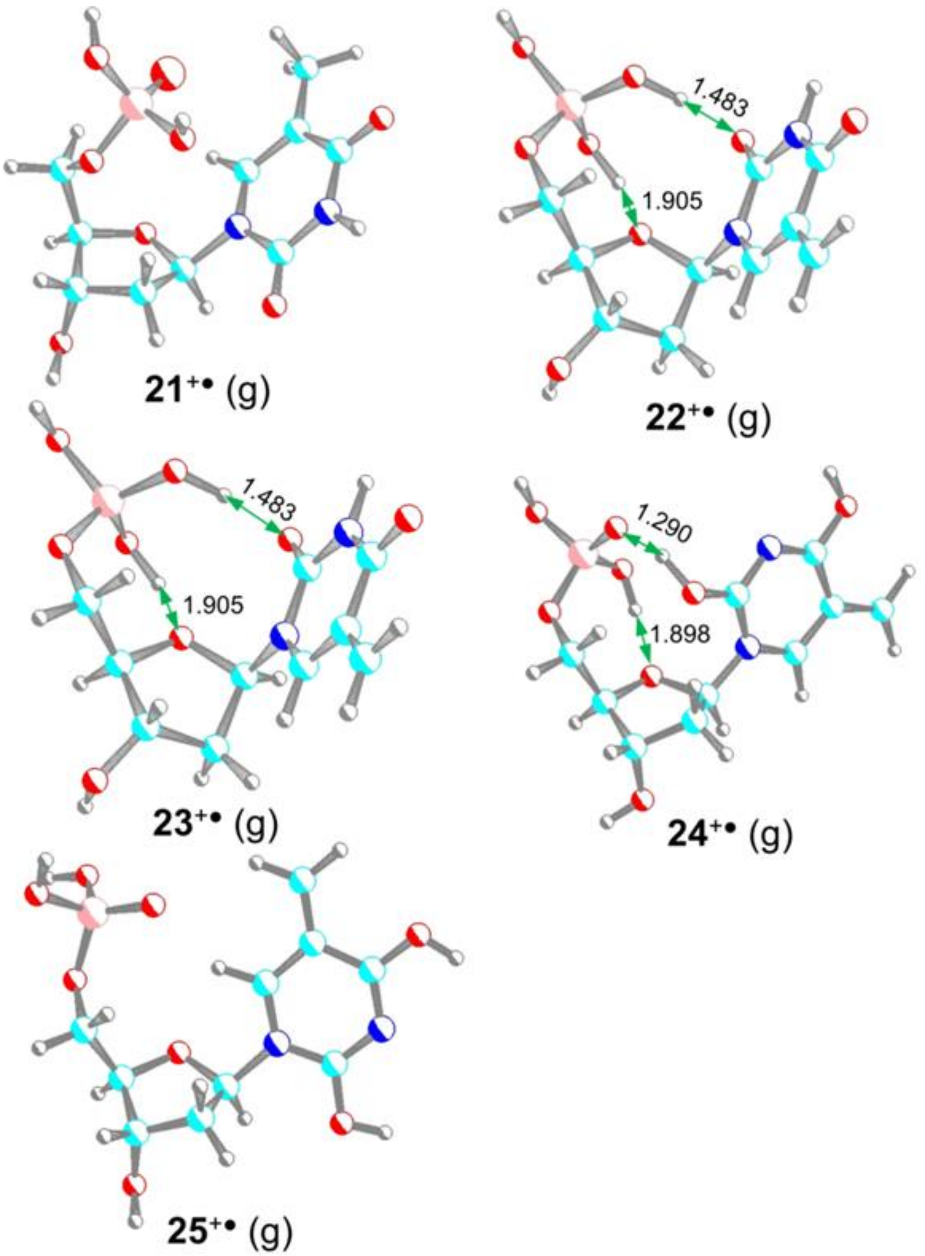

Figure 9. M06-2X/6-311+G(2d,p)-optimized structures of [2’-deoxythymidine phosphate]$^{+\cdot}$ isomers.

Table 4. Relative Energies of [2'-deoxythymidine phosphate]$^{2+\cdot}$ Isomers.

relative energy[a,b]	
gas phase	solvated

ion[c]	B3LYP	M06-2X	ωB97X-D	B3LYP	M06-2X	ωB97X-D
$21^{+\bullet}$	0 (0)[d]	0 (0)[d]	0 (0)[d]	0 (0)[d]	0(0)[d]	0(0)[d]
$22^{+\bullet}$	16 (28)	3 (14)	8 (20)	3 (14)	−6 (5)	−2 (9)
$23^{+\bullet}$	7 (19)	−4 (8)	9 (21)	23 (33)	13 (22)	25 (35)
$24^{+\bullet}$	12 (22)	−8 (2)	7 (16)	27 (34)	−1 (6)	19 (26)
$25^{+\bullet}$	17 (25)	10 (18)	19 (27)	28 (29)	23 (31)	31 (39)

[a]Including B3LYP/6-31+G(d,p) zero-point energy corrections and referring to 0 K unless stated otherwise. [b]Lowest-energy conformers. [c]Relative free energies at 298 K.

4.3.9 Thymidine Isomerization in Ionized Nucleotides

The existence of low-energy [thymine]$^{+\cdot}$ isomers could have a serious effect on charge transfer in ionized oligonucleotides. Because the recombination energies of $8^{+\cdot}-11^{+\cdot}$ are extremely low, in fact, much lower than the RE_{adiab} values of the other nucleobases, thymine ionization and isomerization would trap the hole at the thymine residue, providing a C-7-H_2 radical group for thymine-specific reactions.[19–24] To address this point, we investigated by DFT and ab initio computations the structures and relative energies of 2’-deoxythymidine phosphate cation radicals, both in the gas phase and in the polarizable dielectric of the surrounding water continuum. The ion relative energies, represented by the lowest-energy conformers $21^{+\cdot}$–$25^{+\cdot}$ (Figure 9), were found to depend on the computational method and also to be affected by entropies and solvent effects (Table 4). The canonical tautomer $21^{+\cdot}$ marginally had the lowest free energy ($\Delta G_{g,298}$ °) among the 2’-deoxythymidine phosphate isomers in the gas phase, chiefly because of its high vibrational entropy at 298 K. However, the $\Delta G_{g,298}$ ° values for $21^{+\cdot}$ and the C-7-H_2 tautomers $23^{+\cdot}$ and $24^{+\cdot}$ were as close as 2 kJ mol^{-1} (Table 4). Solvation by water favored the C-7-H_2 tautomer $22^{+\cdot}$, whose $\Delta G_{g,298}$ ° value was very close to those of $21^{+\cdot}$ and 24^{+}

$^{\cdot}$. The calculations indicated that the relative stabilities of thymidine tautomers are extremely sensitive to the local environment and solvent. To resolve this issue, a dedicated computational study of cation-radical A–T pairs in oligonucleotides is needed; however, this exceeds the scope of this work. A conspicuous feature of thymidine cation-radical structures displaying strong intramolecular hydrogen bonds is the spontaneous migration of a thymine hydroxyl proton to the phosphate group, forming distonic ions $22^{+\cdot}$–$24^{+\cdot}$. These ions are expected to behave as thymine radicals and to undergo typical reactions triggered by oxygen addition to the C-7-H_2 group. The internal prototropic isomerization in $22^{+\cdot}$–$24^{+\cdot}$ is an alternative to external proton transfer from ionized thymine to the surrounding water molecules, as suggested previously.[24]

4.4 Conclusions

The experimental and computational results presented in this article point to the existence of noncanonical [thymine]$^{+\cdot}$ isomers having the C-7-H_2 group. The new isomers are formed as major products by intramolecular electron transfer in gas-phase metal–thymine complexes and represent the lowest-energy structures that are more stable than the canonical 2,4-dioxo-N-1,N-3-H form. Theoretical calculations also predict the existence of low-energy noncanonical nucleobase isomers of 2'-deoxythymidine phosphate cation radicals. It remains to be explored if such unusual species play a role in DNA ionization.

4.5 Acknowledgments

Research at University of Washington was supported by the National Science Foundation Division of Chemistry (Grants CHE-1359810, CHE-1661815, and CHE-1624430) and the Klaus and Mary Ann Saegebarth Endowment. H.R. thanks the NSF-REU program (Grant CHE-1659548 to Northern Illinois University) for support.

4.6 References

1. Burrows, C. J.; Muller, J. G. Oxidative Nucleobase Modifications Leading to Strand Scission. *Chem. Rev*. 1998, 98, 1109−1151.
2. Steenken, S. Purine Bases, Nucleosides, and Nucleotides: Aqueous Solution Redox Chemistry and Transformation Reactions of Their Radical Cations and e- and OH Adducts. *Chem. Rev*. 1989, 89, 503−520.
3. Schuster, G. B. One-Electron Oxidation of DNA: Mechanism and Consequences. Nucleic Acids *Symp. Ser*. 2009, 53, 85−86.
4. Kanvah, S.; Joseph, J.; Schuster, G. B.; Barnett, R. N.; Cleveland, C.L.; Landman, U. Oxidation of DNA: Damage to Nucleobases. *Acc. Chem. Res*. 2010, 43, 280−287.
5. Murphy, C. J.; Arkin, M. R.; Jenkins, Y.; Ghatlia, N. D.; Bossmann, S. H.; Turro, N. J.; Barton, J. K. Long-Range Photoinduced Electron-Transfer through a DNA Helix. *Science*. 1993, 262, 1025−1029.
6. Giese, B. Hole Injection and Hole Transfer Through DNA: The Hopping Mechanism. *Top. Curr. Chem*. 2004, 236, 27−44.
7. Saito, I.; Takayama, M.; Sugiyama, H.; Nakatani, K.; Tsuchida, A.; Yamamoto, M. Photoinduced DNA Cleavage Via Electron-transfer. Demonstration That Guanine Residues Located 5′ To Guanine Are the Most Electrondonating Sites. *J. Am. Chem. Soc*. 1995, 117, 6406−6407.

8. Dougherty, D.; Wittel, K.; Meeks, J.; McGlynn, S. P. Photoelectron Spectroscopy of Carbonyls. Ureas, Uracils, and Thymine. *J. Am. Chem. Soc*. 1976, 98, 3815−3820.
9. Fulfer, K. D.; Hardy, D.; Aguilar, A. A.; Poliakoff, E. D. High-Resolution Photoelectron Spectra of the Pyrimidine-Type Nucleobases. *J. Chem. Phys*. 2015, 142, 224310.
10. Majdi, Y.; Hochlaf, M.; Pan, Y.; Lau, K.-C.; Poisson, L.; Garcia, G.A.; Nahon, L.; Al-Mogren, M. M.; Schwell, M. Theoretical and Experimental Photoelectron Spectroscopy Characterization of the Ground State of Thymine Cation. *J. Phys. Chem. A.* 2015, 119, 5951−5958.
11. Choi, K.-W.; Lee, J.-H.; Kim, S. K. Ionization Spectroscopy of a DNA Base: Vacuum-Ultraviolet Mass-Analyzed Threshold Ionization Spectroscopy of Jet-Cooled Thymine. *J. Am. Chem. Soc*. 2005, 127, 15674−15675.
12. Ghosh, D.; Isayev, O.; Slipchenko, L. V.; Krylov, A. I. Effect of Solvation on the Vertical Ionization Energy of Thymine: From Microhydration to Bulk. *J. Phys. Chem. A.* 2011, 115, 6028−6038.
13. Improta, R.; Scalmani, G.; Barone, V. Radical Cations of DNA Bases: Some Insights on Structure and Fragmentation Patterns by Density Functional Methods. Int. *J. Mass Spectrom*. 2000, 201, 321−336.
14. Close, D. M.; Crespo-Hernandez, C. E.; Gorb, L.; Leszczynski, J. Ionization Energy Thresholds (IETs) of Thymine, and Thymine Keto-Enol Tautomers. *J. Phys. Chem. A.* 2006, 110, 7485−7490.
15. Cauet, E.; Lievin, J. Radical Cations of the Nucleic Bases and Radiation Damage to DNA: Ab initio Study. *Adv. Quantum Chem*. 2007, 52, 121−147.

16. Close, D. M.; Crespo-Hernandez, C. E.; Gorb, L.; Leszczynski, J. Theoretical Elucidation of Conflicting Experimental Data on Vertical Ionization Potentials of Microhydrated Thymine. *J. Phys. Chem. A.* 2008, 112, 4405−4409.
17. Seidel, C. A. M.; Schulz, A.; Sauer, M. H. M. Nucleobase-Specific Quenching of Fluorescent Dyes. 1. Nucleobase One-Electron Redox Potentials and Their Correlation with Static and Dynamic Quenching Efficiencies. *J. Phys. Chem*. 1996, 100, 5541−5553.
18. Crespo-Hernandez, C. E.; Close, D. M.; Gorb, L.; Leszczynski, J. Determination of Redox Potentials for Watson-Crick Base Pairs, DNA Nucleosides, and Relevant Nucleoside Analogues. *J. Phys. Chem. B.* 2007, 111, 5386−5395.
19. Joy, A.; Ghosh, A. K.; Schuster, G. B. One-Electron Oxidation of DNA Oligomers That Lack Guanine: Reaction and Strand Cleavage at Remote Thymines by Long-Distance Radical Cation Hopping. *J. Am. Chem. Soc*. 2006, 128, 5346−5347.
20. Ghosh, A.; Joy, A.; Schuster, G. B.; Douki, T.; Cadet, J. Selective One-Electron Oxidation of Duplex DNA Oligomers: Reaction at Thymines. Org. *Biomol. Chem*. 2008, 6, 916−928.
21. Joseph, J.; Schuster, G. B. Oxidatively Damaged Nucleobases in Duplex DNA Oligomers: Reaction at Thymine-Thymine Mispairs. *J. Am. Chem. Soc*. 2009, 131, 13904−13905.
22. Kanvah, S.; Schuster, G. B. One-Electron Oxidation of DNA: Thymine versus Guanine Reactivity. *Org. Biomol. Chem*. 2010, 8, 1340−1343.
23. Kravec, S. M.; Kinz-Thompson, C. D.; Conwell, E. M. Localization of a Hole on an Adenine-Thymine Radical Cation in BForm DNA in Water. *J. Phys. Chem. B.* 2011, 115, 6166−6171.

24. Barnett, R. N.; Joseph, J.; Landman, U.; Schuster, G. B. Oxidative Thymine Mutation in DNA: Water-Wire-Mediated Proton-Coupled Electron Transfer. *J. Am. Chem. Soc.* 2013, 135, 3904−3914.
25. Wagner, J. R.; van Lier, J.-E.; Johnston, L. J. Quinone Sensitized Electron Transfer Photooxidation of Nucleic Acids: Chemistry of Thymine and Thymidine Radical Cations in Aqueous Solution. *Photochem. Photobiol*. 1990, 52, 333−343.
26. Wagner, J. R.; van Lier, J. E.; Decarroz, C.; Berger, M.; Cadet, J. Photodynamic Methods for Oxyradical-Induced DNA Damage. *Methods Enzymol*. 1990, 186, 502−511.
27. Douki, T.; Ravanat, J.-L.; Angelov, D.; Wagner, J. R.; Cadet, J. Effects of Duplex Stability on Charge-Transfer Efficiency within DNA. *Top. Curr. Chem*. 2004, 236, 1−25.
28. Fujita, S.; Steenken, S. Pattern of OH Radical Addition to Uracil and Methyl- and Carboxyl-Substituted Uracils. Electron Transfer of OH Adducts with N,N,N′ ,N′ -tetramethyl-p-phenylenediamine and Tetranitromethane. *J. Am. Chem. Soc*. 1981, 103, 2540−2545.
29. Kim, N.-J. DFT Study of Water-Assisted Intramolecular Proton Transfer in the Tautomers of Thymine Radical Cation. Bull. *Korean Chem. Soc*. 2006, 27, 1009−1014.
30. Kim, N. J.; Kim, H. M.; Kim, S. K. Ionization-Induced Proton Transfer in Thymine-Ammonia van der Waals Clusters. *Int. J. Mass Spectrom*. 2007, 261, 32−37.
31. Heo, J.; Kim, N. J. DFT Study on the Nucleophilic Addition Reaction of Water and Ammonia to the Thymine Radical Cation. *J. Phys. Chem. A*. 2007, 111, 8857−8863.
32. Malone, M. E.; Symons, M. C. R.; Parker, A. W. An EPR Study of Photoionized Thymine and Its Derivatives at 77 K. *J. Chem. Soc., Perkin Trans. 2.* 1993, 2, 2067−75.

33. Yan, M.; Becker, D.; Summerfield, S.; Renke, P.; Sevilla, M. D. Relative Abundance and Reactivity of Primary Ion Radicals in γ-Irradiated DNA at Low Temperatures. 2. Single- vs Double-Stranded DNA. *J. Phys. Chem*. 1992, 96, 1983−1989.

34. Sevilla, M. D. An Electron Spin Resonance Study of the Photoionization of Thymine. The Thymine Cation and Anion Radicals. *J. Phys. Chem*. 1971, 75, 626−631.

35. Nishimoto, S.; Ide, H.; Wada, T.; Kagiya, T. Radiation-Induced Hydroxylation of Thymine Promoted by Electron-Affinic Compounds. *Int. J. Radiat. Biol. Relat. Stud. Phys., Chem. Med*. 1983, 44, 585−600.

36. Sevilla, M. D. Electron Spin Resonance Study of N1-Substituted Thymine π-Cation Radicals. *J. Phys. Chem*. 1976, 80, 1898−1901.

37. Rashid, R.; Mark, F.; Schuchmann, H. P.; Von Sonntag, C. Sulfate Anion Radical-Induced Oxidation of 1,3,6-Trimethyluracil and 1,3,5-Trimethyluracil (1,3-Dimethylthymine) by Potassium Peroxodisulfate in Aqueous Solution: An Interesting Contrast. *Int. J. Radiat. Biol*. 1991, 59, 1081−1100.

38. Deeble, D. J.; Schuchmann, M. N.; Steenken, S.; Von Sonntag, C. Direct Evidence for the Formation of Thymine Radical Cations from the Reaction of Sulfate (SO4·-) with Thymine Derivatives: A Pulse Radiolysis Study with Optical and Conductance Detection. *J. Phys. Chem*. 1990, 94, 8186−8192.

39. Itahara, T.; Fujii, Y.; Tada, M. Oxidation of Thymines by Peroxosulfate Ions in Water. *J. Org. Chem*. 1988, 53, 3421−3424.

40. Adhikary, A.; Kumar, A.; Heizer, A. N.; Palmer, B. J.; Pottiboyina, V.; Liang, Y.; Wnuk, S. F.; Sevilla, M. D. Hydroxyl Ion Addition to One-Electron Oxidized Thymine:

Unimolecular Interconversion of C5 to C6 OH-Adducts. *J. Am. Chem. Soc*. 2013, 135, 3121−3135.

41. Tureček, F. Transient Intermediates of Chemical Reactions by Neutralization-Reionization Mass Spectrometry. *Top. Curr. Chem*. 2003, 225, 77−129.
42. Yao, C.; Cuadrado-Peinado, M.; Polášek, M.; Tureček, F. Specific Generation of 1-Methylcytosine Radicals in the Gas-Phase. *Angew. Chem*., Int. Ed. 2005, 44, 6708−6711.
43. Chen, X.; Syrstad, E. A.; Nguyen, M. T.; Gerbaux, P.; Turecek, F. Distonic Isomers and Tautomers of the Adenine Cation Radical in the Gas Phase and Aqueous Solution. *J. Phys. Chem. A*. 2004, 108, 9283−9293.
44. Wolken, J. K.; Syrstad, E. A.; Vivekananda, S.; Tureček, F. Uracil Radicals in the Gas Phase. Specific Generation and Energetics. *J. Am. Chem. Soc*. 2001, 123, 5804−5805.
45. Tureček, F.; Julian, R. R. Peptide Radicals and Cation-Radicals in the Gas Phase. *Chem. Rev*. 2013, 113, 6691−6733.
46. Korn, J. A.; Urban, J.; Dang, A.; Nguyen, H. T. H.; Turecek, F. UV-Vis Action Spectroscopy Reveals a Conformational Collapse in Hydrogen-Rich Dinucleotide Cation Radicals. *J. Phys. Chem. Lett*. 2017, 8, 4100−4107.
47. Chu, I. K.; Rodriquez, C. F.; Lau, T.-C.; Hopkinson, A. C.; Siu, K. W. M. Molecular Radical Cations of Oligopeptides. *J. Phys. Chem. B*. 2000, 104, 3393−3397.
48. Wee, S.;O’Hair, R. A. J.; McFadyen, W. D. Can Radical Cations of the Constituents of Nucleic Acids Be Formed in the Gas Phase Using Ternary Transition Metal Complexes? *Rapid Commun. Mass Spectrom*. 2005, 19, 1797−1805.

49. Feketeova, L.; Khairallah, G. N.; Chan, B.; Steinmetz, V.; Maitre, P.; Radom, L.; O'Hair, R. A. J. Gas-Phase Infrared Spectrum and Acidity of the Radical Cation of 9-Methylguanine. *Chem. Commun*. 2013, 49, 7343−7345.

50. Lesslie, M.; Lawler, J. T.; Dang, A.; Korn, J. A.; Bím, D.; Steinmetz, V.; Maitre, P.; Tureček, F.; Ryzhov, V. Cytosine Radical Cation: A Gas-Phase Study Combining IRMPD Spectroscopy, UV-PD Spectroscopy, Ion−Molecule Reactions, and Theoretical Calculations. *ChemPhysChem* 2017, 18, 1293−1301.

51. Feketeova, L.; Chan, B.; Khairallah, G. N.; Steinmetz, V.; Maitre, P.; Radom, L.; O'Hair, R. A. J. Gas-Phase Structure and Reactivity of the Keto Tautomer of the Deoxyguanosine Radical Cation. *Phys. Chem. Chem. Phys*. 2015, 17, 25837−25844.

52. Feketeova, L.; Chan, B.; Khairallah, G. N.; Steinmetz, V.; Maitre, P.; Radom, L.; O'Hair, R. A. J. Watson-Crick Base Pair Radical Cation as a Model for Oxidative Damage in DNA. *J. Phys. Chem. Lett*. 2017, 8, 3159−3165.

53. Antoine, R.; Dugourd, P. UV-Visible Activation of Biomolecular Ions. (Laser Photodissociation and Spectroscopy of Mass-Separated Biomolecular Ions). Lect. Notes Chem. 2013, 83, 93−116.

54. Lam, A. K.; Abrahams, B. F.; Grannas, M. J.; McFadyen, W. D.; O'Hair, R. A. J. Tuning the Gas Phase Redox Properties of Copper(II) Ternary Complexes of Terpyridines to Control the Formation of Nucleobase Radical Cations. *Dalton Trans*. 2006, 5051−5061.

55. Shaffer, C. J.; Pepin, R.; Tureček, F. Combining UV Photodissociation Action Spectroscopy with Electron Transfer Dissociation for Structure Analysis of Gas-Phase Peptide Cation-Radicals. *J. Mass Spectrom*. 2015, 50, 1438−1442.

56. Pyatkivskyy, Y.; Ryzhov, V. Coupling of Ion−Molecule Reactions with Liquid Chromatography on a Quadrupole Ion Trap Mass Spectrometer. *Rapid Commun. Mass Spectrom*. 2008, 22, 1288−1294.

57. Frisch, M. J.; Trucks, G. W.; Schlegel, H. B.; Scuseria, G. E.; Robb, M. A.; Cheeseman, J. R.; Scalmani, G.; Barone, V.; Mennucci, B.; Petersson, G. A.; Nakatsuji, H.; Caricato, M.; Li, X.; Hratchian, H. P.; Izmaylov, A. F.; Bloino, J.; Zheng, G.; Sonnenberg, J. L.; Hada, M.; Ehara, M.; Toyota, K.; Fukuda, R.; Hasegawa, J.; Ishida, M.; Nakajima, T.; Honda, Y.; Kitao, O.; Nakai, H.; Vreven, T.; Montgomery, J. A., Jr.; Peralta, J. E.; Ogliaro, F.; Bearpark, M.; Heyd, J. J.; Brothers, E.; Kudin, K. N.; Staroverov, V. N.; Keith, T.; Kobayashi, R.; Normand, J.; Raghavachari, K.; Rendell, A.; Burant, J. C.; Iyengar, S. S.; Tomasi, J.; Cossi, M.; Rega, N.; Millam, J. M.; Klene, M.; Knox, J. E.; Cross, J. B.; Bakken, V.; Adamo, C.; Jaramillo, J.; Gomperts, R.; Stratmann, R. E.; Yazyev, O.; Austin, A. J.; Cammi, R.; Pomelli, C.; Ochterski, J. W.; Martin, R. L.; Morokuma, K.; Zakrzewski, V. G.; Voth, G. A.; Salvador, P.; Dannenberg, J. J.; Dapprich, S.; Daniels, A. D.; Farkas, Ö.; Foresman, J. B.; Ortiz, J. V.; Cioslowski, J.; Fox, D. J. Gaussian 09, revision A.02; Gaussian Inc.: Wallingford, CT, 2009.

58. Becke, A. D. New Mixing of Hartree-Fock and Local Density-Functional Theories. *J. Chem. Phys*. 1993, 98, 1372−1377.

59. Zhao, Y.; Truhlar, D. G. The M06 Suite of Density Functionals for Main Group Thermochemistry, Thermochemical Kinetics, Noncovalent Interactions, Excited States, and Transition Elements: Two New Functionals and Systematic Testing of Four M06-Class Functionals and 12 Other Functionals. *Theor. Chem. Acc*. 2008, 120, 215−241.

60. Chai, J. D.; Head-Gordon, M. Long-Range Corrected Hybrid Density Functionals with Damped Atom-Atom Dispersion Corrections. *Phys. Chem. Chem. Phys*. 2008, 10, 6615−6620.

61. Tomasi, J.; Mennucci, B.; Cammi, R. Quantum Mechanical Continuum Solvation Models. *Chem. Rev*. 2005, 105, 2999−3093.

62. Møller, C.; Plesset, M. S. A Note on an Approximation Treatment for Many Electron Systems. *Phys. Rev*. 1934, 46, 618−622.

63. Dunning, T. H., Jr Gaussian Basis Sets for Use in Correlated Molecular Calculations. I. The Atoms Boron Through Neon and Hydrogen. *J. Chem. Phys*. 1989, 90, 1007−1023.

64. Schlegel, H. B. Potential Energy Curves Using Unrestricted Moller-Plesset Perturbation Theory with Spin Annihilation. *J. Chem. Phys*. 1986, 84, 4530.

65. Mayer, I. Spin-Projected UHF Method. IV. Comparison of Potential Curves Given by Different One-Electron Methods. *Adv. Quantum Chem*. 1980, 12, 189−262.

66. Chan, B.; Radom, L. Assessment of Theoretical Procedures for Hydrogen Atom Abstraction by Chlorine, and Related Reactions. *Theor. Chem. Acc*. 2011, 130, 251−260.

67. Cížek, J. On the Use of the Cluster Expansion and the Technique of Diagrams in Calculations of Correlation Effects in Atoms and Molecules. *Adv. Chem. Phys*. 1969, 14, 35−89.

68. Purvis, G. D., III; Bartlett, R. J. A. Full Coupled-Cluster Singles and Doubles Model − the Inclusion of Disconnected Triples. *J. Chem. Phys*. 1982, 76, 1910−1918.

69. Sekino, H.; Bartlett, R. J. A Linear Response, Coupled-Cluster Theory for Excitation Energy. *Int. J. Quantum Chem*. 1984, 26, 255−265.

70. Comeau, D. C.; Bartlett, R. J. The Equation-of-Motion Coupled-Cluster Method. Applications to Open- and Closed-Shell Reference States. *Chem. Phys. Lett*. 1993, 207, 414−423.
71. Furche, F.; Ahlrichs, A. Adiabatic Time-Dependent Density Functional Methods for Excited State Properties. *J. Chem. Phys*. 2002, 117, 7433−7447.
72. Turecek, F. Benchmarking Electronic Excitation Energies and Transitions in Peptide Radicals. *J. Phys. Chem. A*. 2015, 119, 10101−10111.
73. Nguyen, H. T. H.; Andrikopoulos, P. C.; Bím, D.; Rulíšek, L.; Dang, A.; Tureček, F. Radical Reactions Affecting Polar Groups in Threonine Peptide Ions. *J. Phys. Chem. B*. 2017, 121, 6557−6569.
74. Barbatti, M.; Ruckenbauer, M.; Plasser, F.; Pittner, J.; Granucci, G.; Persico, M.; Lischka, H. Newton-X: A Surface-Hopping Program for Nonadiabatic Molecular Dynamics. Wiley Interdisciplinary Reviews: *Comput. Mol. Sci*. 2014, 4, 26−33.
75. Gilbert, R. G.; Smith, S. C. Theory of Unimolecular and Recombination Reactions; Blackwell Scientific Publications: Oxford, U.K., 1990; pp 52−132.
76. Zhu, L.; Hase, W. L. Program No. QCPE 644; Quantum Chemistry Program Exchange, Indiana University: Bloomington, IN, 1994.
77. Frank, A. J.; Sadílek, M.; Ferrier, J. G.; Tureček, F. Sulfur Oxoacids and Radicals in the Gas Phase. A Variable-Time Neutralization-Photoexcitation-Reionization Mass Spectrometric and Ab Initio/RRKM Study. *J. Am. Chem. Soc*. 1997, 119, 12343−12353.
78. Ulrich, J.; Teoule, R.; Massot, R.; Cornu, A. Mass-Spectrometric Study of the Fragmentation of Uracil and Thymine Derivatives. *Org. Mass Spectrom*. 1969, 2, 1183−99.

79. Imhoff, M.; Deng, Z.; Huels, M. A. Identification of Ion Fragments Produced from Thymine and Deuterated Thymine by Low Energy Ion Impact in Films and Electron Impact in the Gas Phase. *Int. J. Mass Spectrom*. 2005, 245, 68−77.

80. Almeida, D.; Antunes, R.; Martins, G.; Eden, S.; Ferreira da Silva, F.; Nunes, Y.; Garcia, G.; Limao-Vieira, P. Electron Transfer-Induced Fragmentation of Thymine and Uracil in Atom-Molecule Collisions. *Phys. Chem. Chem. Phys*. 2011, 13, 15657−15665.

81. Thymine Mass Spectrum. In NIST Chemistry WebBook; NIST Standard Reference Database 69; National Institute of Standards and Technology (NIST): Gaithersburg, MD, 2005; available at http://webbook.nist.gov/chemistry (accessed October 20, 2017).

82. Meotner, M. Charge Transfer Equilibria and Complexes. In The Encyclopedia of Mass Spectrometry; Gross, M. L., Caprioli, R., Eds; Elsevier: Amsterdam, 2003; Vol. 1, Theory and Ion Chemistry, pp 345−350.

83. Barbatti, M.; Aquino, A. J. A.; Lischka, H. The UV Absorption of Nucleobases: Semi-Classical Ab Initio Spectra Simulations. *Phys. Chem. Chem. Phys*. 2010, 12, 4959−4967.

84. Rejnek, J.; Hanus, M.; Kabelac, M.; Ryjacek, F.; Hobza, P. Correlated Ab Initio Study of Nucleic Acid Bases and Their Tautomers in the Gas Phase, in a Microhydrated Environment and in Aqueous Colution. Part 4. Uracil and Thymine. *Phys. Chem. Chem. Phys*. 2005, 7, 2006−2017.

85. Jiao, D.; Wang, H.; Zhang, Y.; Tang, Y. A DFT Study of Thymine and Its Tautomers. Can. *J. Chem*. 2009, 87, 406−415.

Chapter 5: Near-UV Water Splitting by Cu, Ni, and Co Complexes in the Gas Phase

Reproduced in part with permission from Dang, A.; Shaffer, C.; Bim, D.; Lawler, J.; Lesslie, M.; Ryzhov, V.; Tureček. F. The Journal of Physical Chemistry Letters A. 2018, 122, 2069-2078.

Abstract

(2,2’-Bipyridine)M=O$^+$ ions (M = Cu, Ni, Co) were generated by collision-induced dissociation and near-UV photodissociation of readily available [(2,2’-bipyridine)M^{II}(NO3)]+ ions in the gas phase, and their structure was confirmed by ion−molecule reactions combined with isotope labeling. Upon storage in a quadrupole ion trap, the (2,2’- bipyridine)M=O$^+$ ions spontaneously added water, and the formed [(2,2’-bipyridine)M=O + H_2O]$^+$ complexes eliminated OH upon further near-UV photodissociation. This reaction sequence can be accomplished at a single laser wavelength in the range of 260−340 nm to achieve stoichiometric homolytic cleavage of gaseous water. Structures, spin states, and electronic excitations of the metal complexes were characterized by ion−molecule reactions using ^{2}H and ^{18}O labeling, photodissociation action spectroscopy, and density functional theory calculations.

5.1 Introduction

Water is an extremely stable molecule, as illustrated by its molar enthalpy of formation from O_2 and H_2 (−242 kJ mol^{-1}) and its large O−H bond dissociation energy (499 kJ mol^{-1}).[1] Perhaps for this reason, homolytic splitting of O−H bonds in water has not been pursued as a potential source of H_2 and O_2 for chemical energy storage. Water splitting by oxidation to O_2 and H_3O^+ is achieved by plants in a multistep four-electron process accomplished by the multienzyme photosystem II.[2] Artificial water oxidation has been the target of numerous studies that relied on heterogeneous and homogeneous transition metal (M) catalysts such as complexes of Mn and Ru.[3–5] The mechanistic interpretation of the redox cycles presumes the existence of ligated M=O complexes that oxidize water, forming hydroperoxy intermediates.[6,7] However, these highly reactive M=O intermediates are difficult to characterize in the condensed phase.[7]

The rarefied gas phase is an inert medium that has been used for the generation of numerous highly reactive species in different electronic states that have been characterized by mass spectrometry.[8] Ligated metal-oxide cations, (phen)Cu=O$^+$ (phen = 1,10-phenanthroline) were first generated in the gas phase by Schroder, Schwarz, and co-workers[9] using collision-induced dissociation (CID) of ternary $[(phen)Cu^{II}(NO3)]^{+\cdot}$ ions formed by electrospray ionization.[10] The (phen)Cu=O$^+$ and related ions have been used to study hydrogen abstraction from C−H bonds of various gaseous molecules.[11 − 13] The formation of (phen)Cu=O$^+$ was accomplished under the relatively high-pressure conditions of an electrospray ion source and without mass-selecting the precursor ternary nitrate complex. This led to a partial isomerization of the (phen)-Cu=O$^+$ ions to isomeric (phen−OH)Cu$^+$ ions that were distinguished by Schwarz et al. using ion mobility,[12] and by Roithova et al. using infrared multiphoton dissociation spectroscopy measurements.[11] Isomerization of (phen)Cu=O$^+$ to (phen−OH)Cu$^+$ has been shown by density functional calculation to be highly exothermic.[11] These studies established that the formation of (phen)Cu=O$^+$ and its isomerization in the gas phase depended on the experimental conditions of the applied cone voltage.[11,12] Interest in Cu complexes has been further stimulated by a recent report[14] by Mayer, Goldberg, and co-workers who described a soluble copper complex containing 2,2’-bipyridine (bpy) as a ligand that was an efficient homogeneous catalyst for electrolytic water oxidation.

We now report that simple bpy complexes of Cu, Ni, and Co in the gas phase can be used to achieve nonelectrolytic water splitting. We generated the (bpy)Cu=O$^+$, (bpy)Ni=O$^+$, and (bpy)Co=O$^+$ complexes from mass-selected ion precursors and characterized them by ion−molecule reactions, ^{2}H and ^{18}O isotope labeling, UV−vis photodissociation action spectroscopy, and time-dependent DFT calculations. In particular, we wish to show that in situ made water adducts of the Cu, Ni, and Co complexes undergo near-UV photodissociation achieving stoichiometric water splitting in the gas phase under mild conditions.

5.2 Experimental Section

5.2.1 Materials

Sodium nitrite, 2,2'-bipyridine, copper(II) perchlorate hexahydrate, copper(II) nitrate (97% purity or better), and all solvents were purchased from Sigma-Aldrich (Milwaukee, WI) Water-^{18}O (normalized at 97−98 atom %) was purchased from Icon Isotopes (Summit, NJ). All purchased materials were used as received without further purification. 6-Hydroxy-2,2'-bipyridine was prepared by Pd(Ph$_3$P)$_4$-catalyzed coupling of pyridine-2-magnesium bromide with 2-bromo-6-methoxypyridine (Sigma-Aldrich) followed by hydrolysis.[15] The product was characterized by high-resolution mass spectrometry (measured *m/z* 173.0705, $C_{10}H_9N_2O^+$ requires 173.0709, error < 2.5 ppm) and a CID mass spectrum: *m/z* 173.0705, (M+H)$^+$, *m/z* 155 (loss of H_2O), *m/z* 146 (loss of HCN), *m/z* 145 (loss of CO), *m/z* 131 (loss of NCO).

5.2.2 Mass Spectrometry

Mass spectrometry measurements were performed on a modified LTQ-XL-ETD linear ion trap (LIT) tandem mass spectrometer (ThermoElectron Fisher, San Jose, CA, USA).

$[(bpy)M^{II}(NO_3)]^+$ ions were generated by electrospray ionization of methanol−water solutions containing 2,2'-bipyridine and metal (Cu, Ni, or Co)^{II} nitrates. The ions were selected by mass for the major isotopes (^{63}Cu, ^{58}Ni, ^{59}Co) and stored in the ion trap at 3 mTorr of the He bath gas. CID was performed by resonant ion excitation at normalized collision energies of 10−25 system units. Photodissociation was performed using the previously described equipment.[16,17] The irradiating light beam was produced by an Nd:YAG EKSPLA NL301G laser (Altos Photonics, Bozeman, MT, USA) operating at 20 Hz frequency with a 3−6 ns pulse width. Photons exiting the pump laser are fed into a PG142C unit (Altos Photonics, Bozeman, MT, USA, which integrates a third harmonic generator and optical parametric oscillator coupled with an optional second harmonic generator (SH) to provide wavelength tuning between 210 and 409 nm at a pulse peak power ranging between 0.79 and 2.06 mJ. These powers are measured at each wavelength using an EnergyMax-USB J-10MB energy sensor (Coherent Inc., Santa Clara, CA, USA) to calibrate the spectra. The laser beam is aligned by mirrors and focused by a telescopic lens to pass the small aperture drilled in the auxiliary chemical ionization source used to produce electron donor reagent ions. The laser beam diameter in the LIT is estimated at 3−4 mm to ensure overlap with the trapped ions. Typically, 100 scans were accumulated at each wavelength, and the photofragment ion intensities were normalized to the sum of all fragment ions.

Another set of measurements with regular and ^{18}O-labeled ions were performed on a Thermo Orbitrap Velos instrument. Ions were generated by electrospray ionization, stored in the LIT at bath gas pressure and analyzed by resonant ejection from the LIT or transferred to the Orbitrap analyzer for Fourier transform mass measurements at 100,000 resolving power (fwhm). The *m/z* measured in the ^{18}O labeling experiments were as follows: $[(bpy)^{65}Cu^{II}(NO_2\,^{18}O)]^+$:

measured 284.9915, theoretical 284.9886; $[(bpy)^{65}Cu(^{18}O)]^+$: measured 238.9973, theoretical 238.9957.

Ion−molecule reactions with $H_2{}^{18}O$ were performed on a modified Bruker Esquire 3000 ion trap tandem mass spectrometer (Bruker Daltonics, Billerica, MA, USA).[18] The working pressure in the ion trap was estimated at 1 mTorr He and several mTorr of water vapor introduced by a leak valve.

5.2.3 Calculations

Standard ab initio and density functional theory calculations were performed with the Gaussian 09 suite of programs.[19] All structures were obtained by gradient optimization using the B3LYP[20] CAM-B3LYP,[21] ωB97X-D,[22] and M06[23] hybrid functionals with the 6-311+G(2d,p) basis set and confirmed as local energy minima by harmonic frequency calculations, which gave all real frequencies. The optimized structures are available from the corresponding author upon request. All calculations of open-shell species were performed within the spin-unrestricted formalism. Vertical excitation energies were obtained by time-dependent DFT calculations[24] using the M06 functional and the 6-311++G(3df,2p) basis set in a spin unrestricted formalism. The choice of the M06 functional was based on benchmarking against the experimental absorption and UVPD action spectra of $[(bpy)M(NO_3)]^{+\cdot}$ complexes (M = Cu, Ni, Co), where M06 TD-DFT calculations showed the best match, as discussed later in the paper. Typically 30−40 excited states were generated by TD-DFT calculations. Vibronic absorption spectra were calculated for 30 excited states from 500 configurations generated at 300 K by the Newton-X program.[25]

5.3 Results and Discussion

5.3.1 Formation of (bpy)M=O+ Ions

The reactive complexes, $(bpy)M=O^+$, where M = Cu, Ni, and Co, were generated from ternary transition metal nitrate complexes obtained by electrospray ionization of aqueous-methanol solutions.[26] To illustrate this with the Cu ions, $[(bpy)Cu(NO_3)]^{+\cdot}$ ions were formed by electrospray, selected by mass (*m/z* 281 for the ^{63}Cu isotope), and stored in the ion trap. The ions were subjected to CID, resulting in elimination of NO_2 (Figure 1a) thus forming $(bpy)Cu=O^+$ ions9 that were selected by mass (*m/z* 235) and stored in the ion trap. Analogously, laser photodissociation[16] of gas-phase $[(bpy)Cu(NO_3)]^{+\cdot}$ resulted in elimination of NO_2 and formation of $(bpy)Cu=O^+$ (Figure 1b). The $(bpy)Co=O^+$ and $(bpy)Ni=O^+$ ions were generated analogously from the respective nitrate complexes. An alternative method of generating $(bpy)Cu=O^+$ ions by CID of a mass-selected perchlorate complex, $[(bpy)Cu(ClO_4)]^{+\cdot}$, *m/z* 318 for the ^{35}Cl and ^{63}Cu isotopes, was less efficient, chiefly leading to loss of ClO_4 and forming the $Cu(bpy)^+$ fragment ions. This result differs from those reported by Roithova et al., who used perchlorate complexes for the formation of $LCuO^+$ ions with various ligands (L) under high pressure conditions of an electrospray interface.[13] All Cu-containing ions we generated in the linear ion trap were characterized by appropriate accurate mass measurements.

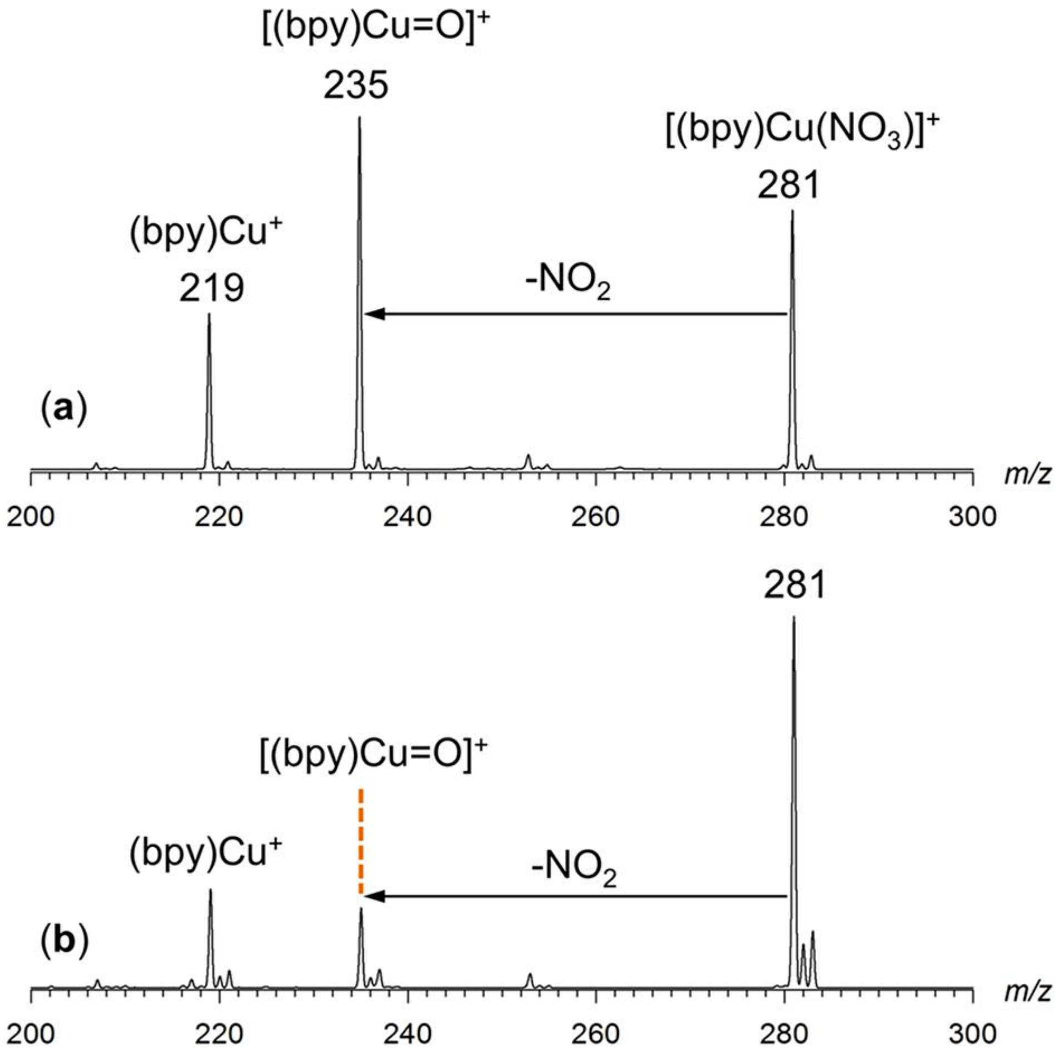

Figure 1. (a) Collision-induced dissociation and (b) 299 nm single-pulse photodissociation spectra of $[(bpy)^{63}CuNO_3]^{+\cdot}$ complexes.

The $(bpy)M{=}O^+$ ions underwent a facile reaction with residual water vapor upon storage in the ion trap, forming $[(bpy)M{=}O + H_2O]^+$ adducts as the only products. The water addition showed a pseudo-first order rate of depletion of the reactant ions. The absolute rate constants were not determined because the water vapor pressure could not be measured accurately; kinetic measurements that were performed on different types of ion trap instruments showed different reaction rates. The relative rates were simultaneously measured for the Cu−Co and Cu−Ni pairs of complexes whose isotopes are well mass-resolved. Figure 2 shows the semi-log plots of the (bpy)M=O^+ ion molar fractions. The curves for (bpy)Cu=O^+ ion depletion via reaction with background water when plotted against those for Ni and Co complexes are perfectly overlapping, indicating identical conditions for all three metal complexes. From these measurements, the (bpy)Co=O^+ ion showed the largest relative rate constant for water addition (k' = 8.8 s^{-1}, r^2 = 0.9996), followed by (bpy)Ni−O+ (k' = 5.6 s^{-1}, r^2 = 0.9996), whereas (bpy)Cu=O^+ was the least reactive (k' = 3.2 s^{-1}, r^2 = 0.9996). The different rates are also reflected by the kinetic curves that show increasing fractions of (bpy)M=O^+ ions, 0.06, 0.10, and 0.19, for Cu, Ni, and Co, respectively, which were already depleted at t = 0 during the preceding 20 ms precursor ion isolation time window.

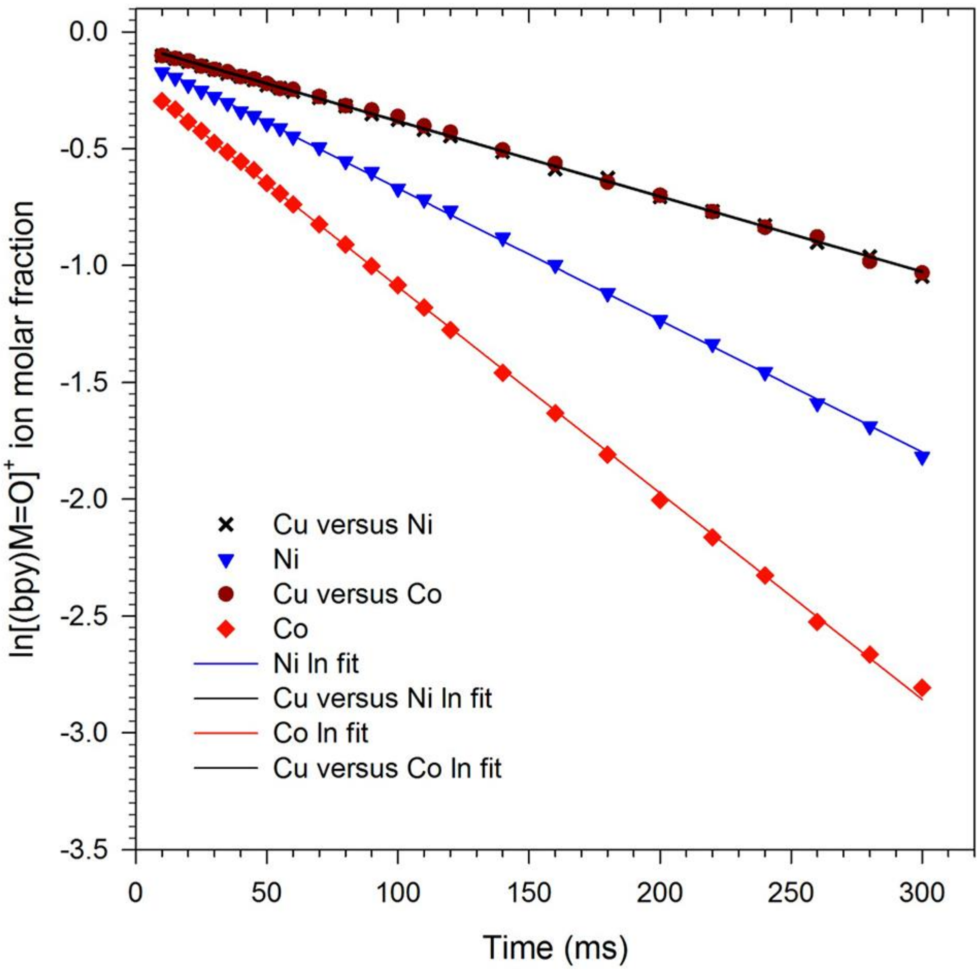

Figure 2. Logarithmic plots for reactions of (bpy)Cu=O$^+$, (bpy)Ni=O$^+$, and (bpy)Co=O$^+$ with water.

5.3.2 Structure Characterization of [(bpy)M=O + H_2O]$^+$ Ions

Previous reports indicated that (phen)Cu=O$^+$ ions can undergo internal oxygen transfer to the phenanthroline ligand forming a 2-hydroxyphenanthroline isomer, (2-OH-phen)-Cu$^+$.[11] In light of those results, we probed the structural integrity of the bpy ligand in the (bpy)M=O$^+$ ions formed in the ion trap. To this end we utilized the facile addition of water to elucidate the structure of the closely related [(bpy)M=O + H_2O]$^+$ adducts using two different probes. In the first probe aimed at the bpy ligand, we generated (D_8-bpy)M=O$^+$ ions by CID of [(D_8-bpy)M(NO_3)]$^{+\cdot}$ complexes. The (D_8-bpy)M=O$^+$ ions were isolated by mass and allowed to react with residual water forming the respective $[(D_8\text{-bpy})M{=}O + H_2O]^+$ adducts. The adducts were stored in the ion trap for up to 2 s. Assuming that the D_8-bpy ligand underwent oxygen insertion forming a D_7-bpy-OD in an isomeric complex, as reported for phenanthroline,[9,11] the newly formed OD group would be expected to undergo gradual D/H exchange with the added light water and surrounding water vapor. However, less than 0.1% D/H exchange was observed for all $[(D_8\text{-bpy})M{=}O + H_2O]^+$ complexes after having been stored in the ion trap for 2 s, indicating that the D atoms remained in the nonexchangeable positions in the bpy ligand.

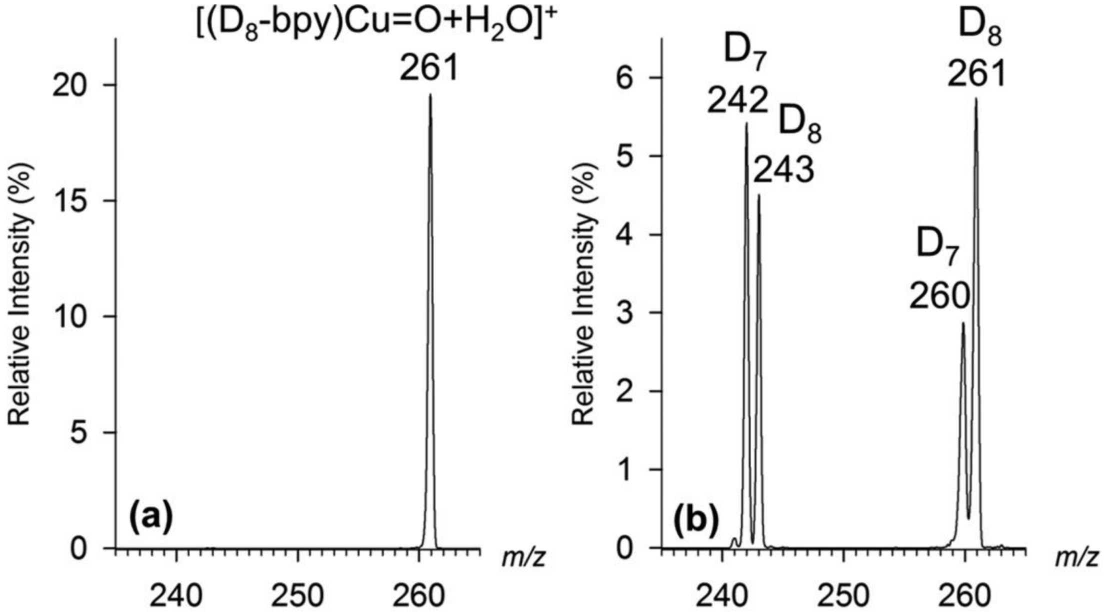

Figure 3. Mass spectra of $[(D_8\text{-bpy})Cu{=}O + H2O]^+$ ions (*m/z* 261) formed by CID (100 ms) of $[(D_8\text{-bpy})^{63}Cu(NO_3)]^{+\cdot}$ followed by water addition. (a) H/D exchange by ion−molecule reactions for 2000 ms with no additional excitation. (b) H/D exchange for 300 ms with CID excitation (100 ms).

Further probing by CID of $[(D_8\text{-bpy})M{=}O + H_2O]^+$ complexes gave different results for Co and Ni on one hand and Cu on the other. CID of $[(D_8\text{-bpy})Co{=}O + H_2O]^+$ and $[(D_8\text{-bpy})Ni{=}O + H_2O]^+$ ions produced the respective $(D_8\text{-bpy})Co{=}O^+$ and $(D_8\text{-bpy})Ni{=}O^+$ ions that, upon storage in the ion trap, added water without D/H exchange. These results indicated that the bpy ligand remained intact in the Co and Ni complexes even after collisional activation. By contrast, collisional activation of $[(D_8\text{-bpy})Cu{=}O + H_2O]^+$ resulted in loss of H_2O that was accompanied by D/H exchange in a 55% fraction of the ions, giving the respective D_8 and D_7 $[(D_x\text{-bpy})Cu{=}O + H_2O]^+$ ions after spontaneous water readdition (Figure 3a,b). This result is consistent with previous studies of $(phen)Cu{=}O^+$ ions, where isomerization by oxygen transfer to the ligand was promoted by collisional activation.[11,12]

An additional probe was based on comparing the properties of $(bpy)Cu{=}O^+$ and $[(bpy)Cu{=}O + H_2O]^+$ ions with those of authentic $(6\text{-OH-bpy})Cu^+$ and $[(6\text{-OH-bpy})Cu + H_2O]^+$ isomers. The latter ions were generated by CID of the $[(6\text{-OH-bpy})Cu^{II}(CH_3COO)]^+$ complex (*m/z* 294 for the ^{63}Cu isotope) prepared by electrospray of an aqueous-methanol solution of 6-hydroxy-2,2'-bipyridine, $CuSO_4$ and acetic acid.[26] CID of the $[(6\text{-OH-bpy})Cu(CH_3COO)]^+$ ion produced the $(6\text{-OH-bpy})Cu^+$ ions at *m/z* 235 that spontaneously added water upon storage in the ion trap, forming $[(6\text{-OH-bpy})Cu + H_2O]^+$ at *m/z* 253. The water addition was reversible, as documented by CID of the water adduct that reformed $(6\text{-OH-bpy})Cu^+$. The $[(6\text{-OH-bpy})Cu + H_2O]^+$ ions were further probed by UVPD at 311 nm (Figure 4). Whereas UVPD of $[(bpy)Cu{=}O + H_2O]^+$ resulted in a dominant loss of OH (Figure 4a), UVPD of $[(6\text{-OH-bpy})Cu + H_2O]^+$ ions resulted in an exclusive loss of the water ligand (Figure 4b). In summary, these combined D/H exchange and UVPD experiments provided strong evidence for the structure integrity of the $[(bpy)Cu{=}O + H_2O]^+$ ions and their $(bpy)Cu{=}O^+$ precursors, and further highlighted the unique reactivity of the ligated $M{=}O^+$ complexes.

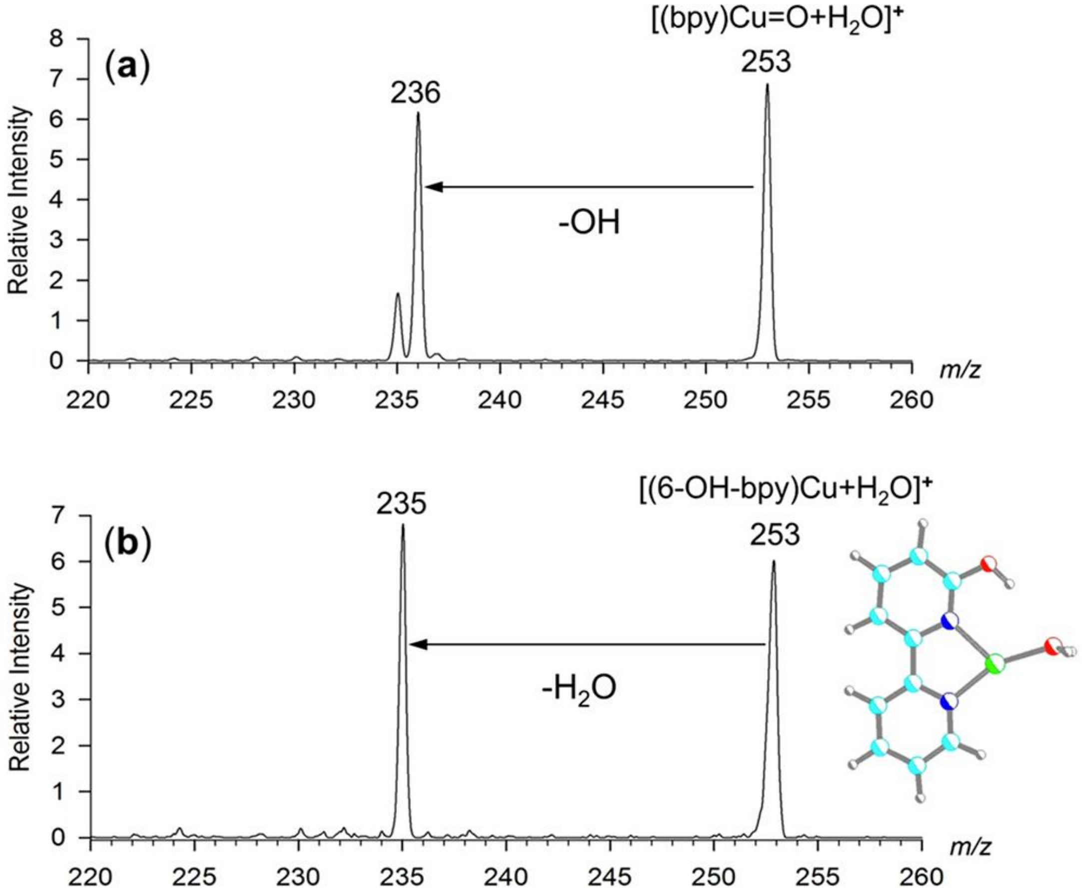

Figure 4. Photodissociation spectra (311 nm, single 12 mJ laser pulse) of (a) $[(bpy)^{63}Cu{=}O + H_2O]^+$ and (b) $[(6\text{-}OH\text{-}bpy)^{63}Cu + H_2O]^+$.

5.3.3 Oxygenated Ligands in $[(bpy)M{=}O + H_2O]^+$ Ions

Ligation of the two oxygen and hydrogen atoms in the $[(bpy)M{=}O + H_2O]^+$ complexes raised further questions about the nature of the oxygenated ligands. The possible combinations, a H_2O_2 molecule, two hydroxyl groups ligated to the metal ion, or a water adduct to a metal-oxo complex, were distinguished by using specific ^{18}O labeling of the oxygen atoms introduced sequentially into the metal complexes. In these experiments, we probed ligand exchange combined with complementary ^{18}O isotope labeling. An ion − molecule reaction of the $(bpy)^{65}Cu{=}O^+$ (*m/z* 237) ion with $H_2{}^{18}O$ that was introduced into the ion trap[18,27] produced the $[(bpy)Cu{=}O + H_2{}^{18}O]^+$ adduct that was isolated by mass (*m/z* 257). The ^{65}Cu isotope was selected to avoid overlap of $^{63}Cu^{18}O$ and $^{65}Cu^{16}O$ isobars due to spurious light water in the ion trap. Resonant excitation and CID of $[(bpy)^{65}Cu{=}O + H_2{}^{18}O]^+$ produced exclusively (>99%) $(bpy)^{65}Cu{=}O^+$ (*m/z* 237, Figure 5a) by elimination of $H_2{}^{18}O$. Hence, under these conditions, the oxygen atoms in the water adduct were nonequivalent and did not undergo equilibration by proton transfer. The reversible nature of the water elimination-addition is apparent from the CID spectrum of $[(bpy)^{65}Cu{=}O + H_2{}^{18}O]^+$ (Figure 5a) that shows the formation of $[(bpy)^{65}Cu{=}O + H_2O]^+$ at *m/z* 255 by reaction with background light water during the CID excitation time.

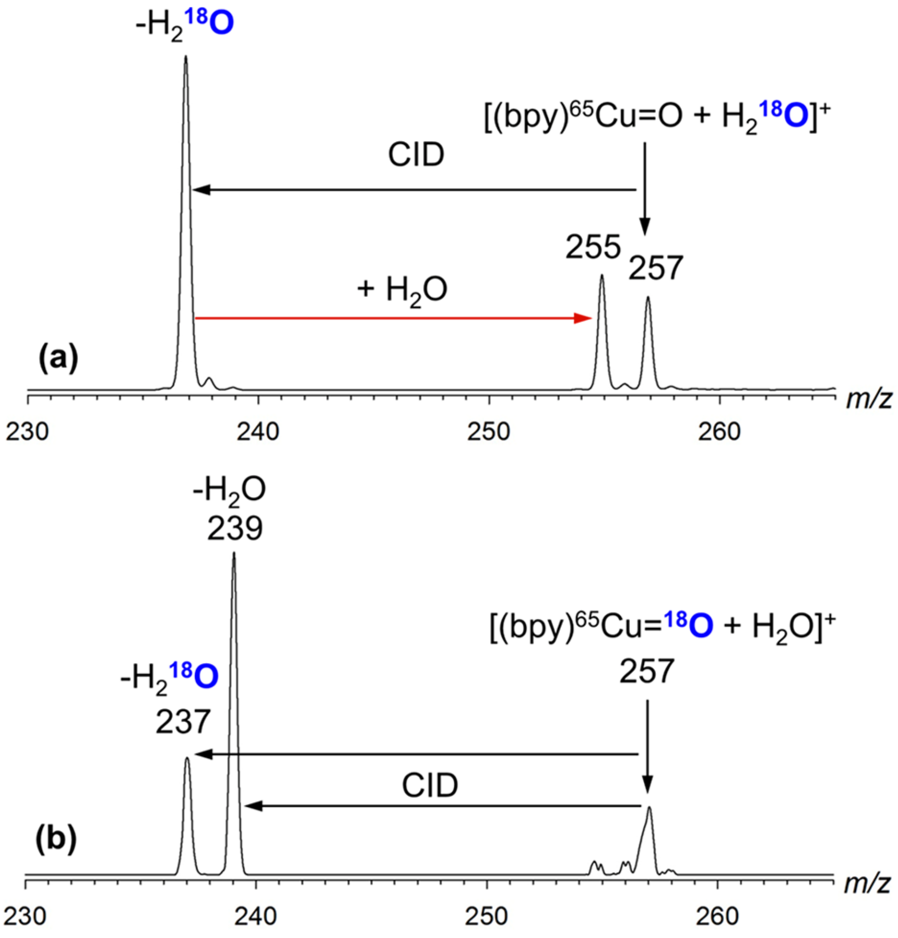

Figure 5. Collision-induced dissociation mass spectra of (a) $[(bpy)^{65}Cu{=}^{18}O + H_2O]^+$ and (b) $[(bpy)^{65}Cu{=}O + H_2{}^{18}O]^+$ ions.

Contrasting results were obtained for the complementary reaction with light water of the ^{18}O labeled Cu complex, $(bpy)^{65}Cu{=}^{18}O^+$ at *m/z* 239, that was generated by CID of $[(bpy)^{65}Cu^{II}(NO_2\ ^{18}O)]^+$ in another ion trap mass spectrometer operating under lower water pressure conditions (Orbitrap Velos) and characterized by accurate mass measurements. Addition of light water followed by resonant excitation CID of mass-selected $[(bpy)^{65}Cu{=}^{18}O + H_2O]^+$ gave two products by loss of H_2O and $H_2\ ^{18}O$ in a 71:29 ratio (±0.08) as an average of measurements at three collision energies (Figure 5b). This indicated oxygen equilibration by hydrogen migration in a 0.58 molar fraction of the water adduct complex, whereas a 0.42 molar fraction corresponded to unscrambled $[(bpy)^{65}Cu{=}^{18}O + H_2O]^+$. We interpret these results as being due to a different composition of water adducts to $(bpy)Cu{=}O^+$ ions generated under different conditions. Water adducts generated at a higher background water pressure contained nonequivalent oxygenated ligands, whereas water addition at a low pressure formed a mixture of complexes containing both types of ligands.

Addition of $H_2\ ^{18}O$ to the $(bpy)Ni{=}O^+$ and $(bpy)Co{=}O^+$ ions formed adducts that were selected by mass (*m/z* 250 and 251, respectively) and investigated by CID. The $[(bpy)Ni{=}O^+ + H_2\ ^{18}O]^+$ ion competitively eliminated $H_2\ ^{18}O$ and light water in a 4:3 ratio, indicating prevalent equilibration of the ligated oxygen atoms. The data analysis was complicated by the rapid reverse addition of light and heavy water to the $(bpy)Ni{=}O^+$ product ions that formed adducts (*m/z* 248, 250, and 252) in which the oxygen atoms were scrambled. The $[(bpy)Co{=}O^+ + H_2\ ^{18}O]^+$ ion also competitively eliminated $H_2\ ^{18}O$ and light water, but because of the very fast reverse water addition, the label scrambling was extensive.

5.3.4 UV Water Splitting and Action Spectra

Photodissociation at 311 nm of the $[(bpy)Cu{=}O + H_2O]^+$ complex revealed that near-UV electronic excitation resulted in the splitting of the ligated water molecule and release of an OH radical. Considering the overall sequence for the gas-phase reactions involving $(bpy)Cu{=}O^+$ (eq 1), near-UV photodissociation effectively achieved dissociation of the water molecule

$$[(bpy)Cu{=}O]^+ + H_2O \rightarrow [(bpy)Cu{=}O + H_2O]^+ \rightarrow [(bpy)Cu\text{-}OH]^{+\cdot} + OH^{\cdot} \quad (1)$$

that was mediated by the Cu complex. This contrasts direct photodissociation of gaseous water that requires wavelengths in the vacuum UV region (<180 nm).[28] This unexpected result prompted us to investigate UVPD of the $[(bpy)M{=}O + H_2O]^+$ and related ion complexes over a broader range of wavelengths. To begin with, we obtained a UV−vis photodissociation action spectrum[17] of mass-selected $[(bpy)\text{-}CuNO_3]^{+\cdot}$. The spectrum was similar to the absorption spectrum of $(bpy)Cu\text{-}(NO_3)_2$ measured in aqueous-methanol solution, indicating that the gas-phase structure and electronic properties of this ion were similar to those of the species in solution. The photodissociative elimination of NO_2 (fragment ion *m/z* 235) showed broad maxima at 285 and 240 nm and competed with a minor loss of $NO_3^{\cdot}$ (fragment ion at *m/z* 219.

Near-UV photodissociation of the Ni^{II} and Co^{II} bpy complexes gave similar results. The action spectrum of $[(bpy)NiNO_3]^{+\cdot}$ (^{58}Ni, *m/z* 276) showed well-developed absorption maxima at 290 and 310 nm, extending by a weaker arm to 350 nm. Further broad bands appeared at 230−250 nm. The $[(bpy)CoNO_3]^{+\cdot}$ (^{59}Co, *m/z* 277) complex showed a band centered at 306 nm and a weaker broad band stretching from 280 to 210 nm. In both cases, the main photodissociation channel corresponded to loss of NO_2, forming the respective $(bpy)Ni{=}O^+$ and $(bpy)Co{=}O^+$ ions.

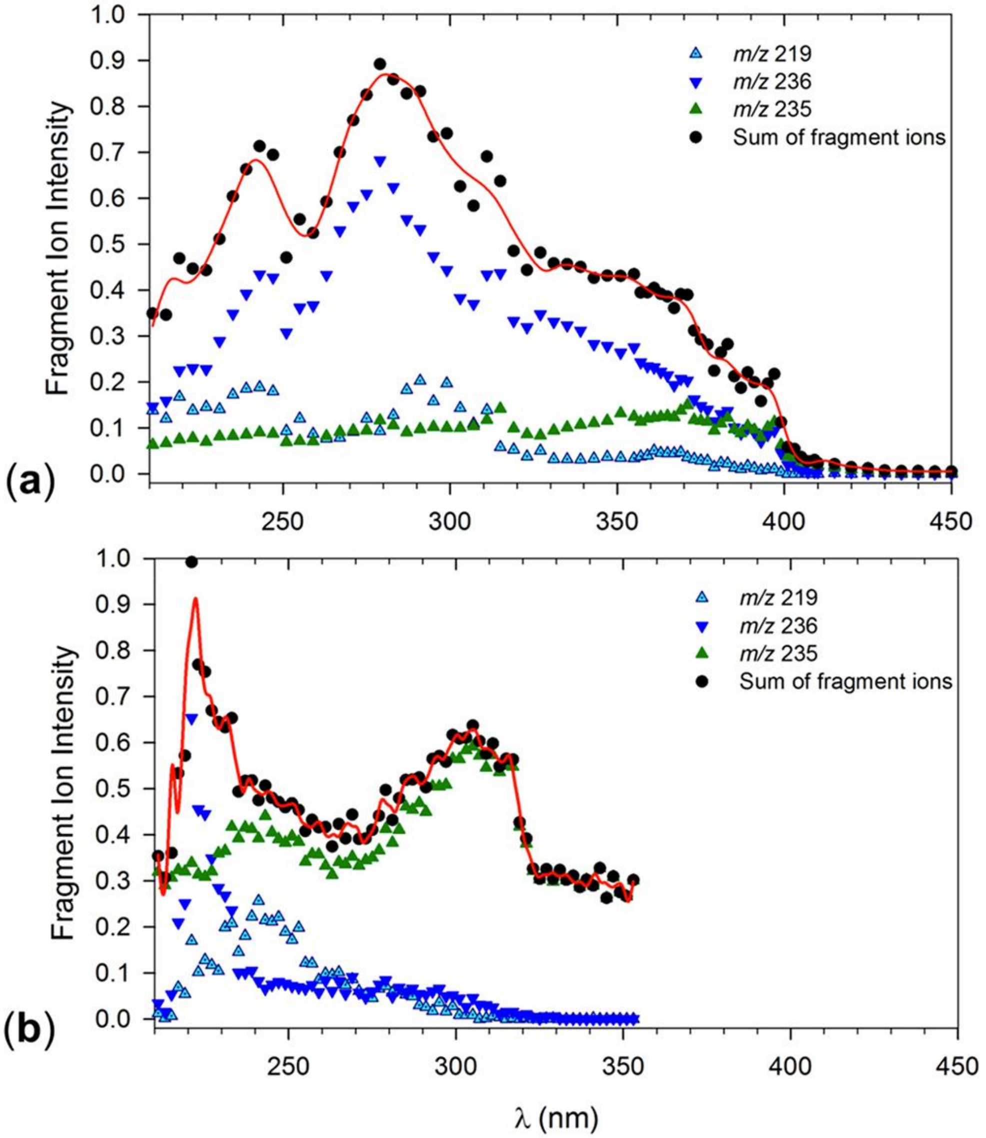

Figure 6. Photodissociation action spectra of (a) [(bpy)Cu=O + H_2O]$^+$, (b) [(6-OH-bpy)Cu + H_2O]$^{+\cdot}$. Blue triangles: loss of OH channel; green triangles: loss of water channel; black circles: sum of photofragment ion intensities.

Photodissociation of the water adducts was investigated by UV−vis action spectroscopy (Figure 6a,b). The [(bpy)Cu=O + H_2O]$^+$ complex showed three dissociation channels; a major loss of OH (*m/z* 236), and less abundant loss of H_2O (*m/z* 235), and 2OH (*m/z* 219) (Figure 6a). The loss of OH showed absorption maxima at 330 (broad), 315, 280, and 244 nm. The loss of water displayed a broad band with a maximum at 370 nm and less pronounced ones at 315 and

245 nm. The *m/z* 219 dissociation channel showed maxima at 365, 296, and 244 nm. No photodissociation was observed near 617 nm where the $[(bpy)Cu(OH)_2]^+$ complex was reported to absorb in aqueous solution.[29] The UVPD action spectrum of the isomeric $[(6\text{-}OH\text{-}bpy)Cu + H_2O]^+$ complex (Figure 6b) showed a major band with a maximum at 305 nm that was almost entirely due to the *m/z* 235 (loss of water) channel. Loss of OH became significant at short wavelengths of <230 nm. The data in Figure 6a and 6b show that the UVPD action spectra of the isomeric complexes were distinctly different. In particular, the *m/z* 235 loss of water showed a very minor shoulder in the spectrum of the $[(bpy)Cu{=}O + H_2O]^+$ complex (Figure 6a). We note that this complex undergoes loss of water upon collisional activation, which proceeds from vibrationally excited ground electronic state of the ion. The minor fraction of water loss upon photodissociation can be assigned to ions that underwent internal conversion from the excited electronic state to the vibrationally excited ground state. It should be noted that, whereas collisional activation of $[LCu{=}O + H_2O]^+$ complexes with dicoordinating auxiliary ligands results in loss of water, CID of an acetonitrile complex,[13] $[(CH_3CN)Cu{=}O + H_2O]^+$, has been reported to result in elimination of OH in a process analogous to the above-described photodissociation.

The $[(bpy)Ni{=}O + H_2O]^+$ ion showed major absorption bands at 230, 310, and 340 nm with an arm extending to 420 nm (Figure 7a). A weak absorption band was observed at 590 nm. In contrast to the Cu complex, the Ni complex showed dominant loss of water (*m/z* 230) that peaked at 310 and 240 nm. The 230, 310, and 340 nm bands were also observed for the $[(bpy)Co{=}O + H_2O]^+$ ion that further showed a well-developed band with a maximum at 430 nm (Figure 7b). However, the Co complex showed a different course for the elimination of OH (*m/z*

232) that peaked at 230 and 310 nm, whereas loss of water was slightly more abundant at 340 and 430 nm.

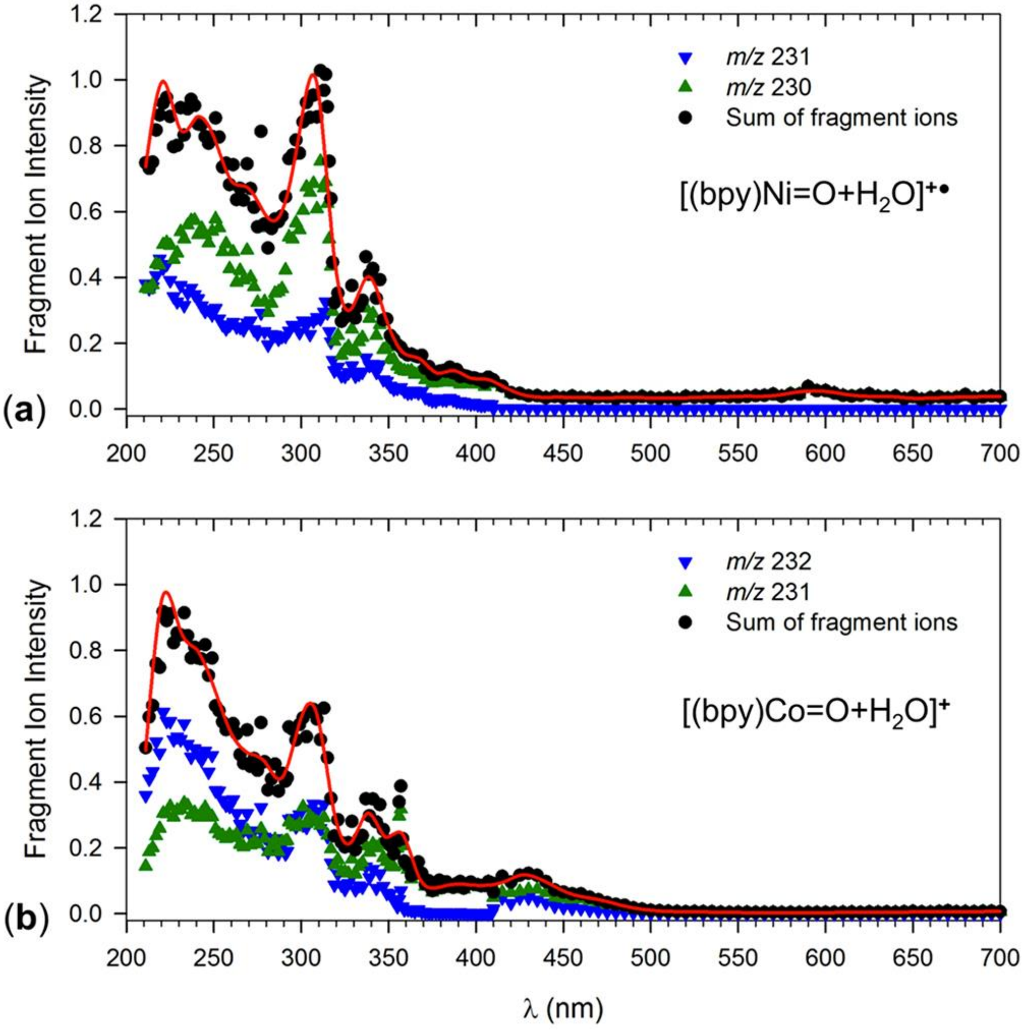

Figure 7. Photodissociation action spectra of (a) [(bpy)Ni=O + H_2O]$^{+\cdot}$, (b) [(bpy)Co=O + H_2O]$^+$ complexes. Blue triangles: loss of OH channel; green triangles: loss of water channel; black circles: total photofragment ions.

5.3.5 Ion Electronic Structures

In order to interpret the dissociations and light absorption characteristics of the complexes we carried out extensive DFT and TD-DFT calculations. The calculated M−O bond lengths in (bpy)M=O$^+$ were substantially shorter than in the covalent water adducts, justifying the formulas with M=O double bonds. We note that the analogous (phen)Cu=O$^+$ ion structures and energetics have been analyzed previously by Schroder, Roithova et al.[11] Starting with the Cu complexes, the ground electronic state of the (bpy)Cu=O$^+$ ion is a triplet (1, $^3A_2$)9 whereas the singlet state (2, $^1A''$) is substantially less stable. The singlet−triplet energy difference was 94−106 kJ mol^{-1} according to calculations by four DFT methods (Table 1). The ωB97X-D/6-311+G(3df,2p) data are discussed in the text and displayed in the potential energy diagram ($\Delta H°_{g,0}$, Figure 8a). Attachment of a water molecule to 1 was continuously exothermic leading to a complex (3) at −32 kJ mol^{-1} relative to the reactants. The reaction free energy was calculated as $\Delta G°_{g,310}$ = 1.2 kJ mol^{-1} at 310 K, indicating that this stage of the addition is reversible. Complex 3 can be further stabilized by forming a Cu−OH_2 covalent bond in a triplet intermediate 4 at −64 kJ mol^{-1} relative to the reactants. Ion 4 can undergo a facile isomerization by proton migration between the OH_2 and O groups (E_{TS1} = 28 kJ mol^{-1} relative to 4), exothermically forming a symmetrical adduct with equivalent Cu-ligated OH groups (5, Figure 8a).

Addition of water to the singlet ion 2 was continuously exothermic. At the Cu−OH_2 distance of 2.2 Å the water molecule rotated about the Cu−O axis over a small potential energy ridge (8−10 kJ mol^{-1}), allowing one of the protons to approach the other Cu-bound oxygen atom. This was followed by an exothermic proton transfer forming adduct 6. The PES indicated that the singlet and triplet states can interconnect through a surface crossing[30] at distances of r(Cu−OH_2) ≤ 2.15, leading to the more stable singlet adduct 6.

Table 1. Energies of (bpy)Cu Ion Complexes.

	Relative Energy^{a,b}							
	B3LYP		CAM-B3LYP		ωB97X-D		M06	
Ion/Reaction	A^c	B^d	A	B	A	B	A	B
Triplet Energies								
$[(\mathrm{bpy})\mathrm{CuNO_3}]^{+\bullet} \rightarrow (^3\mathrm{A_2})\mathbf{1} + \mathrm{NO_2}$	244	247	268	271	278	281	282	283
$\mathbf{1} + \mathrm{H_2O} \rightarrow \mathbf{3}$	−28	−25	−33	−30	−35	−32	−36	−33
$\mathbf{1} + \mathrm{H_2O} \rightarrow \mathbf{4}$	−50	−47	−66	−63	−68	−64	−71	−68
$\mathbf{4} \rightarrow \mathbf{5}$	−19	−8	−8	2	−19	−9	−9	1
TS1(**4** → **5**)	24	24	24	24	29	28		
$\mathbf{4} \rightarrow (^2\mathrm{A''})\mathrm{Cu(bpy)OH}^{+\bullet} + \mathrm{OH}^\bullet$	77	74	88	85	91	88	102	99
$(\mathrm{bpy})\mathrm{Cu{-}OH}^{+\bullet} \rightarrow \mathbf{1} + \mathrm{H}^\bullet$	451	454	458	462	457	461	454	458
$(\mathrm{bpy})\mathrm{Cu{-}OH}^{+\bullet} \rightarrow \mathrm{Cu(bpy)}^+ + \mathrm{OH}^\bullet$	236	239	238	241	237	240	226	228
$(\mathrm{bpy})\mathrm{Cu{-}OH}^{+\bullet} \rightarrow \mathrm{Cu(bpy - H)}^{+\bullet} + \mathrm{H_2O}$	207	206	212	212	211	210	188	185
$(\mathrm{bpy})\mathrm{Cu{-}OH}^{+\bullet} \rightarrow (^2\mathrm{A''})\mathrm{CuOH}^{+\bullet} + \mathrm{bpy}$	468	471	508	512	507	510	496	499
$(\mathrm{bpy})\mathrm{Cu{-}OH}^{+\bullet} + \mathrm{OH}^\bullet \rightarrow \mathbf{1} + \mathrm{H_2O}$	−27	−27	−22	−22	−23	−23		
Singlet Energies								
$[(\mathrm{bpy})\mathrm{CuNO_3}]^{+\bullet} \rightarrow (^1\mathrm{A''})\mathbf{2} + \mathrm{NO_2}$	339	340	374	375	384	385	375	375
$\mathbf{2} + \mathrm{H_2O} \rightarrow \mathbf{6}$	−221	−218	−231	−230	−232	−230	−235	−233
$\mathbf{2} + \mathrm{H_2O} \rightarrow \mathbf{7}$	−110	−107	−136	−132	−139	−136	−131	−128
$\mathbf{2} + \mathrm{H_2O} \rightarrow \mathbf{8}$	−408	−408	−444	−444	−451	−451	−461	−461
$(\mathrm{bpy})\mathrm{Cu}^+ \rightarrow \mathrm{Cu}^+ + \mathrm{bpy}$							403	406
$(\mathrm{bpy})\mathrm{Cu}^+ \rightarrow \mathrm{Cu} + \mathrm{bpy}^{+\bullet}$							454	457
$\mathrm{bpy} \rightarrow \mathrm{bpy}^{+\bullet}$							805	805
$\mathrm{Cu} \rightarrow \mathrm{Cu}^+$							754	754

[a] In kJ mol^{-1}. [b] Including zero-point energy corrections. [c] Calculations with the 6-311+G(2d,p) basis set. [d] Calculations with the 6-311+G(3df,2p) basis set.

(**a**) Cu

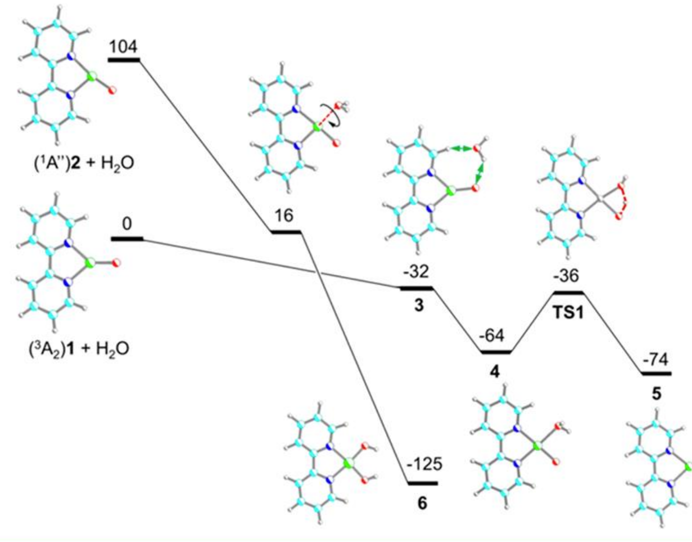

104
(^{1}A'')**2** + H$_2$O
0
(^{3}A$_2$)**1** + H$_2$O
16
-32
3
-64
4
-36
TS1
-74
5
-125
6

(**b**) Ni

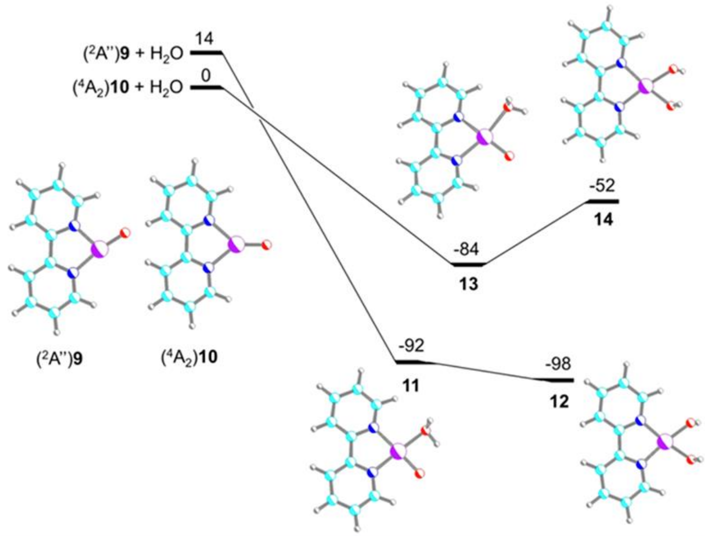

(^{2}A'')**9** + H$_2$O
14
(^{4}A$_2$)**10** + H$_2$O
0
-52
14
-84
13
-92
11
-98
12
(^{2}A'')**9**
(^{4}A$_2$)**10**

(**c**) Co

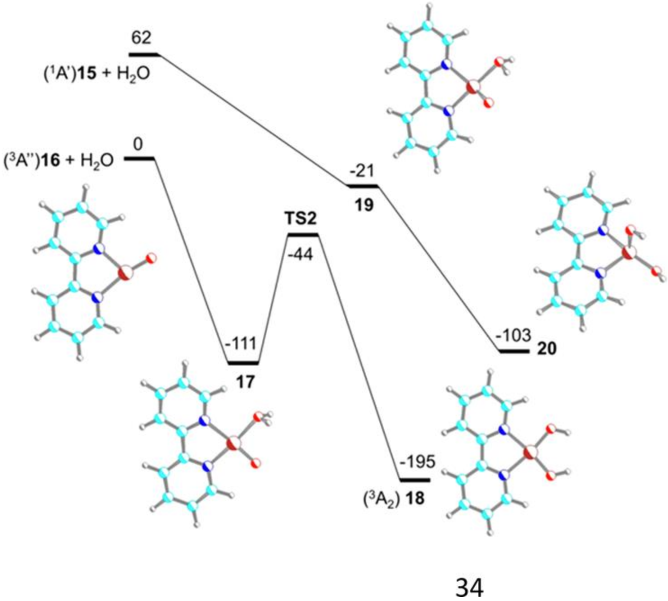

62
(^{1}A')**15** + H$_2$O
0
(^{3}A'')**16** + H$_2$O
-21
19
TS2
-44
-111
17
-103
20
-195
(^{3}A$_2$) **18**

Figure 8. Potential energy diagram (kJ mol^{-1}) for (a) Cu, (b) Ni, and (c) Co complexes relative to the [(bpy)M=O]$^+$ + H_2O reactants. From ωB97X-D/6-311+G(3df,2p) calculations including zero-point vibrational energy corrections.

The nature of the (bpy)Cu=O$^+$ water adduct formed by the ion−molecule reaction was elucidated by analyzing the UVPD action spectrum of the *m/z* 253 ion (Figure 6a) using TD-DFT calculations (Figure 9a−c). First, the TD-DFT-calculated excitation energies were benchmarked on the action spectra of (bpy)[$CuNO_3$]$^{+\cdot}$ and (bpy)Cu$^+$, which showed excellent agreement for the M06/6-311+G(2d,p) and 6-311+G(3df,2p) calculations that were then used for the other species. The bands in the action spectrum of [(bpy)Cu=O + H_2O]$^+$ appear in the TD-DFT absorption spectra of 6 and 4 (Figure 9a,b), but cannot be represented by a single species. In particular, the long wavelength band in the action spectrum extending to 400 nm is prominent in the absorption spectrum of the triplet complex 4, where it appears at 325 nm (ΔE = 3.81 eV) and is further broadened and red-shifted by vibronic transitions at 310 K (Figure 9b). The pertinent electron transition, MO61β → MO64β, involves Cu-centered $\sigma_{x,y}$ and $\sigma_{x,y}$* molecular orbitals (MO). The intense band at 292 nm (Figure 9b) is assigned to the bpy π(MO64α) → π*(MO66α) transition (ΔE = 4.25 eV). However, the spectrum of 4 does not display an abundant band at 240 nm, which is prominent in the action spectrum. This band appears at 237 nm (ΔE = 5.22 eV) in the calculated spectrum of 6 (Figure 9a) and arises from combined $\pi_z \rightarrow \pi_z^*$ transitions within the bpy ligand and $\sigma_{x,y} \rightarrow \sigma_{x,y}^*$ transitions involving the Cu-centered molecular orbitals. Combining the calculated spectra of of 4 and 6 in a 3:1 mixture then provides an excellent fit to the action spectrum after intensity scaling (Figure 9c). It is noteworthy that the calculated absorption spectrum of the covalent triplet adduct 5 shows bands at 295 and 270 nm that can account for some minor features in the action spectrum. Thus, the presence of 5 in the adduct cannot be excluded, but it is unlikely to represent a major component. Other plausible structures, such as a $[(\text{bpy})\text{Cu-}\mu\text{-H}_2\text{O}_2]^+$ adduct (7) and a $[(6\text{-OH-bpy})\text{Cu}-\text{ OH}_2]^+$ complex (8) were examined but gave absorption spectra that were incompatible with the action spectrum. It is noteworthy that none of the gas-phase $[(\text{bpy})\text{Cu(OH)}_2]^+$ isomers showed a strong absorption band at 617 nm that has been reported in solution.[14,29] Weak bands (oscillator strength <0.001) were calculated at 579 and 595 nm for 5 and at 651 nm for 6.

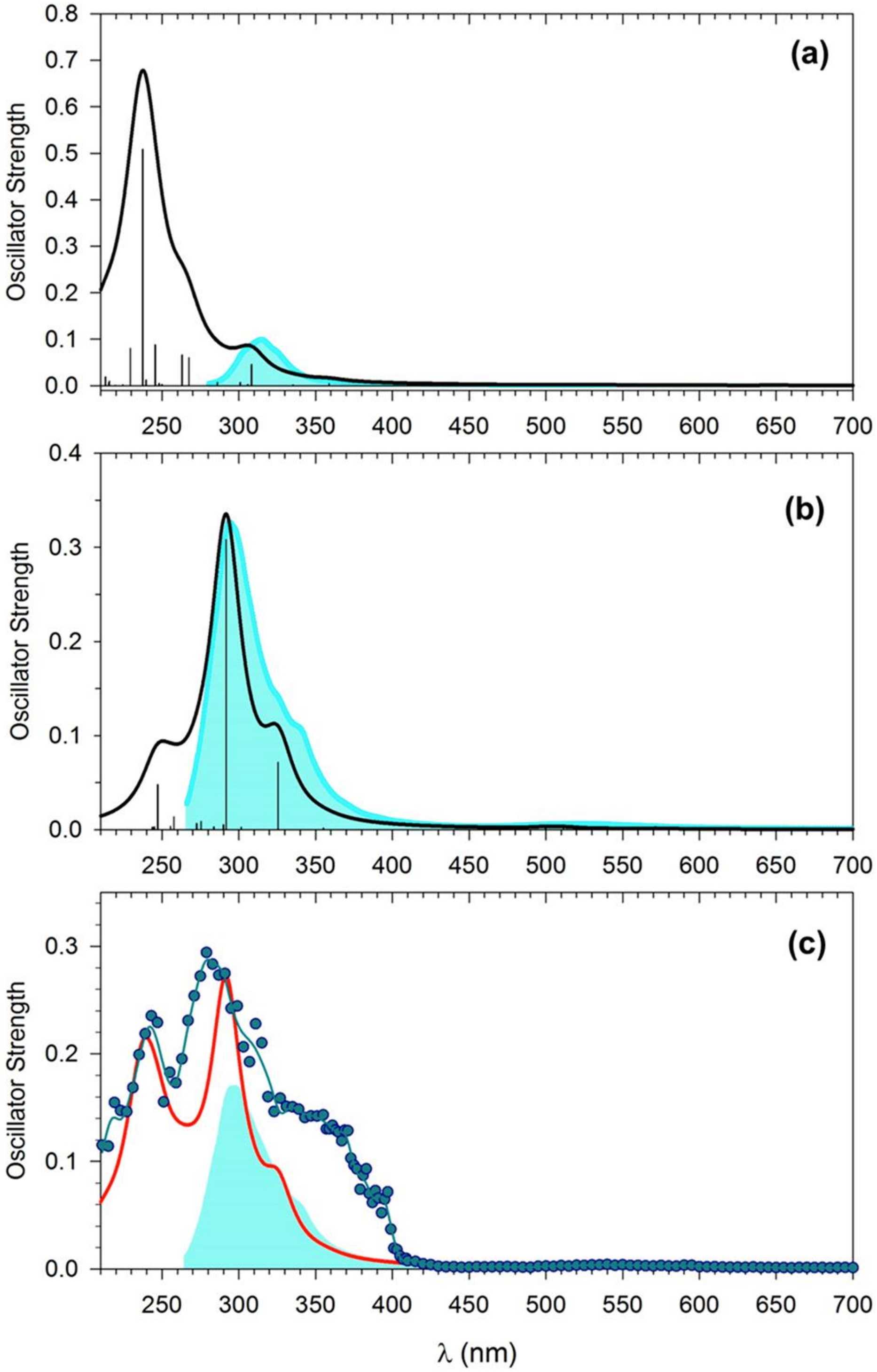

Figure 9. TD-DFT M06/6-311+G(3df,2p) calculated absorption spectra of (a) 6 and (b) 4. The green-shaded curves are from TDDFT calculations of top 30 excited states including vibronic transitions from 500 configurations sampled at 310 K. (c) Fit of the intensity-scaled action spectrum of [(bpy)Cu=O + H_2O]$^+$ (green circles and fitting curve) and the calculated absorption spectrum of a 3:1 mixture of 4 and 6 (red curve and green shaded area).

The ^{18}O labeling and action spectroscopy data pointed to the dynamical nature of the reaction of 1 with water, which was sensitive to the surrounding conditions of residual gas pressure and collisional cooling. When the reaction was performed under higher pressure conditions, the $[(bpy)Cu{=}O + H_2O]^+$ system followed the triplet-state trajectory forming complex 4 that was collisionally cooled and avoided crossing to the more stable singlet 6. Under the low-pressure conditions, ca. 60% of the reacting system crossed to the singlet state. Under intermediate pressure/collision cooling conditions used in the action spectroscopy measurements, ca. 75% of the complexes remained in the triplet state.

The Ni and Co complexes showed some specific features that distinguished them from the Cu system. The doublet ($^2A''$)9 and quartet ($^4A_2$)10 states of $(bpy)Ni{=}O^+$ are nearly isoenergetic and each can be the reactant in the exothermic addition of water (Figure 8b, Table 2). The water adducts of the doublet-state are the nearly isoenergetic asymmetric (11) and symmetric (12) ions that can interconvert. The quartet-state products favor the asymmetric adduct 13. The more loosely bound water in asymmetric adducts can presumably be displaced by an external water molecule to undergo exchange.

The 310 nm band in the action spectrum of the $[(bpy)Ni{=}\ O + H_2O]^+$ ion (Figure 7a) can be fitted by the TD-DFT calculated absorption spectra of 11 and 12. However, only 11 shows bands at 340 and 400 nm to fit the action spectrum whereas the 590 nm band can originate only from 12. Hence, the action spectrum of $[(bpy)Ni{=}O + H_2O]^+$ can be represented by a mixture of 11 and 12, which is also consistent with their comparable relative energies that should allow them to coexist at thermal equilibrium (Figure 8b).

The $(bpy)Co=O^+$ ions clearly favor the triplet ($^3A''$)16 state over the ($^1A'$)15 singlet (Figure 8c, Table 3). Water addition to 16 can proceed on the triplet-state potential energy surface forming exothermically the asymmetric adduct 17 that can isomerize to the final symmetric adduct ($^3A_2$)18. The singlet potential energy surface runs parallel to and above of that of the triplet state, so no surface crossing is indicated. The final singlet-state adduct 20 is at a significantly higher energy than 18. The action spectrum of the $[(bpy)Co=O + H_2O]^+$ ion (Figure 7b) shows a close fit with the TD-DFT-calculated absorption spectra of 17 and 18 regarding the 310 and 340 nm bands. The 430 nm band is represented (at 460 nm) in the calculated spectrum of 17 only. This indicates that the gas-phase ion population contains both 17 and 18. In view of its higher relative energy, the presence of complex 17 must be due to kinetic trapping. We calculated the unimolecular rate constants for the 17 → 18 isomerization using the RRKM theory[31] and the ωB97X-D energies from Table 3. These indicate that 17 having 75 kJ mol^{-1} internal energy, corresponding to 495 K rovibrational temperature, would have a 50 ms half-life which is compatible with the ion trapping time. A half-life for a fully thermalized 17 at 310 K was obtained from transition state theory as $t_{1/2}$ = 95 ms. Hence, the presence of the higher-energy asymmetric ion 17 in the population of stable $[(bpy)Co=O + H_2O]^+$ ions is not excluded by the isomerization kinetics.

5.3.6 Stoichiometric versus Catalytic Water Splitting

Photodissociation of the $[(bpy)M(NO_3)]^+$ ions followed by water addition and further photodissociation of the $[(bpy)M=O + H_2O]^+$ adducts achieves dissociation of the water molecule. The pertinent action spectra indicate that strong absorption bands of $[(bpy)M(NO_3)]^+$ and $[(bpy)M=O + H_2O]^+$ overlap at 300 nm, allowing the use of single-color photodissociation.

To close the reaction cycle and achieve a catalytic photodissociation process in the gas phase,[32] the $[(bpy)M{-}OH]^+$ products have to be photolyzed to liberate the $[(bpy)M{=}O]^+$ active species. To explore this step, we obtained the action spectrum of the $[(bpy)Cu{-}OH]^{+\cdot}$ ion (Figure 10a) that was generated by CID of a serine ternary complex, $[(bpy)Cu(Ser - H)]^{+\cdot}$,[33] and characterized by its matching absorption spectrum from TD-DFT calculations (Figure 10b). The action spectrum shows a strong absorption band at 300 nm that overlaps with the absorption bands used to generate the $[(bpy)Cu{-}OH]^{+\cdot}$ ion. However, photodissociation of $[(bpy)Cu{-}OH]^{+\cdot}$ did not result in a loss of a hydrogen atom to reform the $[(bpy)Cu{=}\ O]^+$ ions to repeat the water addition and splitting, closing the catalytic cycle.[34] The main dissociation channels are loss of OH and H_2O forming the *m/z* 219 and 218 fragment ions. The dissociations of $[(bpy)\text{-}Cu{-}OH]^{+\cdot}$ are essentially consistent with the pertinent energy thresholds (Table 1). The loss of water, forming $[(bpy - H)Cu]^{+\cdot}$, has the lowest threshold energy (210 kJ mol^{-1} relative to $[(bpy)Cu{-}OH]^{+\cdot}$) and is the dominant channel in collision-induced dissociation. The reaction is reversible, as the $[(bpy - H)Cu]^{+\cdot}$ ion adds water, and the addition−elimination reactions can be cycled with trapped mass-selected ions. Loss of OH from $[(bpy)Cu{-}OH]^{+\cdot}$ requires 241 kJ mol^{-1} of threshold energy and is one of the major photodissociation channels. By contrast, loss of H from the OH group is a high-energy process of a 461 kJ mol^{-1} threshold energy that is not triggered by even higher-energy photons ($\lambda < 259$ nm). Interestingly, the O−H bond in $[(bpy)Cu{-}OH]^{+\cdot}$ is weaker than in water, as the hydrogen transfer from $[(bpy)Cu{-}OH]^{+\cdot}$ to OH is calculated to be 23 kJ mol^{-1} exothermic (Table 1). The results for the Ni and CO complexes were analogous to those for Cu in that the loss of H was energetically disfavored against the loss of OH (Tables 2 and 3).

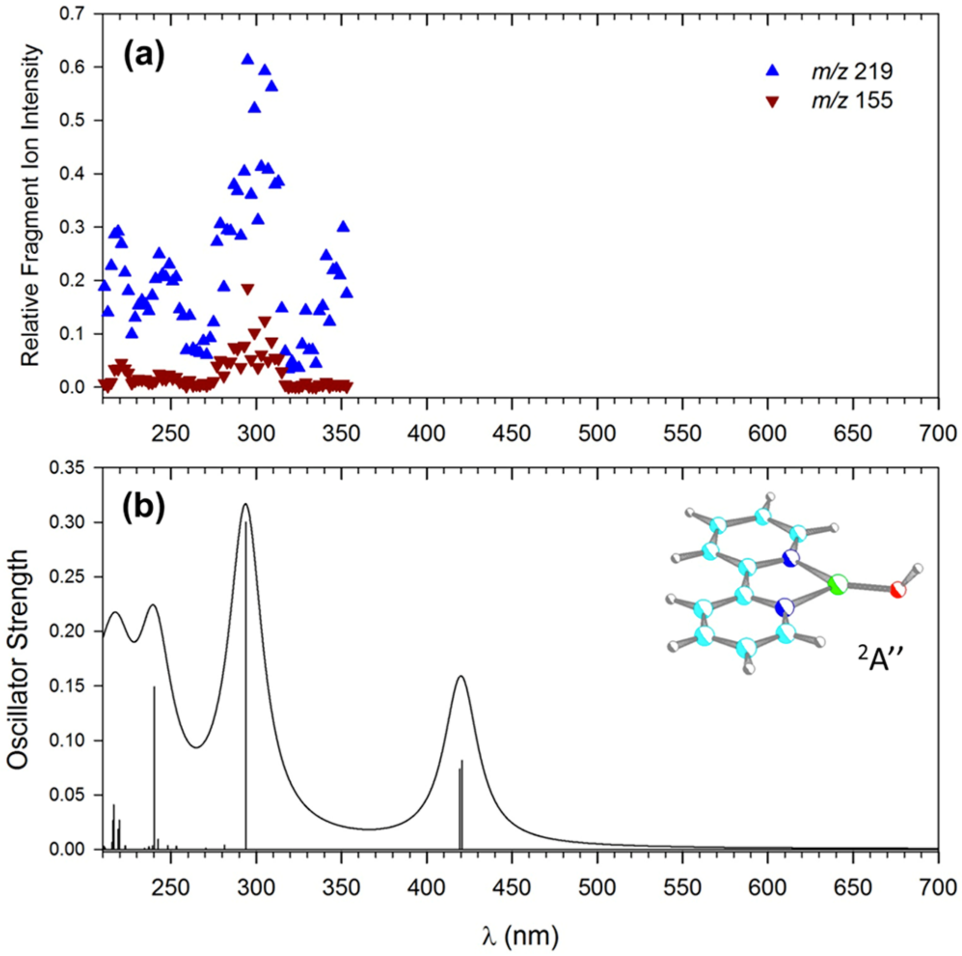

Figure 10. (a) Photodissociation action spectra of (bpy)Cu−OH$^+$ (*m/z* 236) (b) TD-DFT M06/6-311+G(3df,p) calculated absorption spectrum of (^{2}A”)(bpy)Cu−OH$^{+\cdot}$ showing major transitions at 215, 240, and 294 nm. The lines were convoluted with Lorenztian functions at 12 nm full width at half-maximum.

5.4 Conclusions

Near-UV photodissociation at 300 nm can be used to drive the formation of gas-phase metal-oxo ions of the (bpy)M=O$^+$ type (M = Cu, Ni, Co) that spontaneously add water in ion−molecule reactions. The resulting [(bpy)M=O + H_2O]$^+$ complexes are photolyzed by near-UV light to eliminate OH radicals, effectively cleaving the added water molecules. The gas-phase water splitting reaction is stoichiometric, as the [(bpy)M−OH]$^+$ products do not photodissociate to reform the (bpy)M=O$^+$ reactants. The [(bpy)M=O + H_2O]$^+$ ion structures, electronic states, and dissociations were characterized by photodissociation action spectroscopy and density functional theory calculations to elucidate the processes involved in water splitting. Further efforts are needed to reform the $[(bpy)M=O]^+$ reactant ions and close the catalytic cycle.

5.5 Acknowledgments

We thank the Chemistry Division of the National Science Foundation (Grants CHE-1661815 and CHE-1543805) for research funding, and the Klaus and Mary Ann Saegebarth Endowment for general support. Thanks are due to Jarred Olson and Professor Cody Schlenker for their help with the electrochemical synthesis of 18O labeled nitrate.

5.6 References

1. http://webbook.nist.gov/chemistry/ (accessed November 22, 2017).
2. McEvoy, J. P.; Brudvig, G. W. Water-Splitting Chemistry of Photosystem II. *Chem. Rev.* 2006, 106, 4455−4483.
3. Joya, K. S.; Valles-Pardo, J. L.; Joya, Y. F.; Eisenmayer, T.; Thomas, B.; Buda, F.; de Groot, H. J. M. Molecular Catalytic Assemblies for Electrodriven Water Splitting. *ChemPlusChem* 2013, 78, 35−47.
4. Sala, X.; Romero, I.; Rodríguez, M.; Escriche, L.; Llobet, A. Molecular Catalysts That Oxidize Water to Dioxygen. *Angew. Chem.*, Int. Ed. 2009, 48, 2842−2852.
5. Hurst, J. K. Chemistry in Pursuit of Water Oxidation Catalysts for Solar Fuel Production. *Science.* 2010, 328, 315−316.
6. Liu, X.; Wang, F. Transition Metal Complexes That Catalyze Oxygen Formation from Water:1979−2010. *Coord. Chem. Rev*. 2012, 256, 1115−1136.

7. Karkas, M. D.; Verho, O.; Johnston, E. V.; Akermark, B. Artificial Photosynthesis: Molecular Systems for Catalytic Water Oxidation. *Chem. Rev*. 2014, 114, 11863−12001.
8. Tureček, F. Transient Intermediates of Chemical Reactions by Neutralization-Reionization Mass Spectrometry. *Top. Curr. Chem*. 2003, 225, 77−129.
9. Schroder, D.; Holthausen, M. C.; Schwarz, H. Radical-Like Activation of Alkanes by the Ligated Copper Oxide Cation (Phenanthroline)CuO+. *J. Phys. Chem. B.* 2004, 108, 14407−14416.
10. Turecek, F. Copper-Biomolecule Complexes in the Gas Phase. The Ternary Way. *Mass Spectrom. Rev*. 2007, 26, 563−582.
11. Jasikova, L.; Hanikyrova, E.; Schroder, D.; Roithova, J. Aromatic C-H Bond Activation Revealed by Infrared Multiphoton Dissociation Spectroscopy. *J. Mass Spectrom*. 2012, 47, 460−465.
12. Rijs, N. J.; Weiske, T.; Schlangen, M.; Schwarz, H. On Divorcing Isomers, Dissecting Reactivity, and Resolving Mechanisms of Propane C-H and Aryl C-X (X = halogen) Bond Activations Mediated by a Ligated Copper(III) Oxo Complex. *Chem. Phys. Lett*. 2014, 608, 408−424.
13. Yassaghi, G.; Andris, E.; Roithova, J. Reactivity of Copper(III)-Oxo Complexes in the Gas Phase. *ChemPhysChem* 2017, 18, 2217−2224.
14. Barnett, S. M.; Goldberg, K. I.; Mayer, J. M. A. Soluble Copper- Pyridine Water-Oxidation Electrocatalyst. *Nat. Chem*. 2012, 4, 498−502.
15. Kaczmarek, L.; Balicki, R.; Lipkowski, J.; Borowicz, P.; Grabowska, A. Structure and Photophysics of Deazabipyridyls. Excited Internally Hydrogen-Bonded Systems with One Proton Transfer Reaction Site. *J. Chem. Soc., Perkin Trans. 2.* 1994, 2, 1603−1610.

16. Shaffer, C. J.; Marek, A.; Pepin, R.; Slováková, K.; Tureček, F. Combining UV Photodissociation with Electron Transfer for Peptide Structure Analysis. *J. Mass Spectrom*. 2015, 50, 470−475.
17. Shaffer, C. J.; Pepin, R.; Tureček, F. Combining UV Photodissociation Action Spectroscopy with Electron Transfer Dissociation for Structure Analysis of Gas-Phase Peptide Cation-Radicals. *J. Mass Spectrom*. 2015, 50, 1438−1442.
18. Pyatkivskyy, Y.; Ryzhov, V. Coupling of Ion−Molecule Reactions with Liquid Chromatography on a Quadrupole Ion Trap Mass Spectrometer. *Rapid Commun. Mass Spectrom*. 2008, 22, 1288−1294.
19. Frisch, M. J.; Trucks, G. W.; Schlegel, H. B.; Scuseria, G. E.; Robb, M. A.; Cheeseman, J. R.; Scalmani, G.; Barone, V.; Mennucci, B.; Petersson, G. A., et al. Gaussian 09, revision A.02; Gaussian, Inc.: Wallingford CT, 2009.
20. Becke, A. D. A. New Mixing of Hartree-Fock and Local Density-Functional Theories. *J. Chem. Phys*. 1993, 98, 1372−1377.
21. Yanai, T.; Tew, D. P.; Handy, N. C. A New Hybrid Exchange-Correlation Functional Using the Coulomb-Attenuating Method (CAM-B3LYP). *Chem. Phys. Lett*. 2004, 393, 51−57.
22. Chai, J. D.; Head-Gordon, M. Long-Range Corrected Hybrid Density Functionals with Damped Atom-Atom Dispersion Corrections. *Phys. Chem. Chem. Phys*. 2008, 10, 6615−6620.
23. Zhao, Y.; Truhlar, D. G. The M06 Suite of Density Functionals for Main Group Thermochemistry, Thermochemical Kinetics, Noncovalent Interactions, Excited States,

and Transition Elements: Two New Functionals and Systematic Testing of Four M06-Class Functionals and 12 Other Functionals. *Theor. Chem. Acc*. 2008, 120, 215−241.

24. Furche, F.; Ahlrichs, A. Adiabatic Time-Dependent Density Functional Methods for Excited State Properties. *J. Chem. Phys*. 2002, 117, 7433−7447.
25. Barbatti, M.; Ruckenbauer, M.; Plasser, F.; Pittner, J.; Granucci, G.; Persico, M.; Lischka, H. Newton-X: A Surface-Hopping Program for Nonadiabatic Molecular Dynamics. Wiley Interdisciplinary Reviews: *Comput. Mol. Sci*. 2014, 4, 26−33.
26. Gatlin, C. L.; Tureček, F.; Vaisar, T. Determination of Soluble Cu(I) and Cu(II) Species in Jet Fuel by Electrospray Ionization Mass Spectrometry. *Anal. Chem*. 1994, 66, 3950−3958.
27. Osburn, S.; Ryzhov, V. Ion−Molecule Reactions: Analytical and Structural Tool. *Anal. Chem*. 2013, 85, 769−778.
28. Haddad, G. N.; Samson, J. A. R. Total Absorption and Photoionization Cross Sections of Water Vapor between 100 and 1000 A. *J. Chem. Phys*. 1986, 84, 6623−6626.
29. Garribba, E.; Micera, G.; Sanna, D.; Strinna-Erre, L. The Cu(II)-2,2'-bipyridine System Revisited. *Inorg. Chim. Acta*. 2000, 299, 253−261.
30. Schroder, D.; Shaik, S.; Schwarz, H. Two-State Reactivity As a New Concept in Organometallic Chemistry. *Acc. Chem. Res*. 2000, 33, 139−145.
31. Gilbert, R. G.; Smith, S. C. Theory of Unimolecular and Recombination Reactions; Blackwell: Oxford, U.K., 1990; pp 52−132.
32. Tsybizova, A.; Roithova, J. Copper-Catalyzed Reactions: Research in the Gas Phase. *Mass Spectrom. Rev*. 2016, 35, 85−110.

33. Gatlin, C. L.; Tureček, F.; Vaisar, T. Gas-Phase Complexes of Amino Acids with Copper(II) and Diimine Ligands. Part II. Amino Acids with O, N and S Functional Groups in the Side-Chain. *J. Mass Spectrom*. 1995, 30, 1617−1627.

34. Roithova, J.; Schroder, D. Selective Activation of Alkanes by Gas-Phase Metal Ions. *Chem. Rev*. 2010, 110, 1170−1211.